Università degli Studi di Ferrara

DOCTORAL COURSE IN PHYSICS

CYCLE XXXV

COORDINATOR Prof. Luppi, Eleonora

Optimization of Spin Coherence Time at a Prototype Storage Ring for Electric Dipole Moment Investigations

Scientific/Disciplinary Sector (SDS) FIS/04

Candidate

Dott. Shankar, Rahul

(signature)

Supervisor

Prof. Lenisa, Paolo

(signature)

Year 2020/2023

Università degli Studi di Ferrara

Dottorato di Ricerca in Fisica – Ciclo XXXIV

Coordinatrice:
Prof. Luppi, Eleonora

Optimization of Spin Coherence Time at a Prototype Storage Ring for Electric Dipole Moment Investigations

Settore Scientifico Disciplinare FIS/04

Anni:
2019 – 2023

Dottorando

Shankar, Rahul

Tutore

Prof. Lenisa, Paolo

Tutore Esterno
Prof. Lehrach, Andreas

Abstract

The standard model of particle physics has thus far fallen short of being able to explain the observed amount of matter-antimatter asymmetry in the Universe. Electric Dipole Moments (EDMs) of fundamental particles are very sensitive probes of physics beyond the Standard Model. The JEDI collaboration is dedicated to the measurement of the electric dipole moments of charged particles by using a polarized beam in storage rings. The goal can be accomplished by performing the measurement in a pure electrostatic storage ring, which can freeze the horizontal spin precession of protons. As an intermediate step, a smaller "prototype" storage ring, capable of using a combination of electric and magnetic fields, is proposed to serve as a proof-of-principle and to better understand the required systematics. A fundamental parameter to be optimised to reach the highest possible sensitivity in the EDM measurement is the Spin Coherence Time (SCT) of the stored polarized beam, that is the time interval within which the particles of the stored beam maintain a net polarisation greater than 1/e of its initial value. To identify the working conditions that maximise SCT, accurate spin dynamics simulations have been performed on the lattice of the prototype ring. This study presents an investigation of the variation of the beam and spin parameters that influence SCT as well as an optimisation strategy for the sextupole settings to obtain the highest spin coherence time at any given working condition of the ring. The study provides a data set of many configurations with spin coherence times high enough to meet the sensitivity requirements of the EDM measurement. It also analyses the possible design factors that may negatively impact SCTs and discusses possible reconfigurations or design upgrades to improve these values in the future.

Acknowledgements

This thesis in the pages that follow, will take on the daunting task of describing the world we live in exactly as it is. While there are so many pages that fly on in their attempt to do this task justice, there are only these two pages that reflect on all those individuals who made this attempt possible. As unfair as this reality may be, I will nevertheless spend these moments making the best of my two pages of retrospect and gratitude.

While CP violation may be the thing that comes to mind when I think "why am I here?", Prof. Paolo Lenisa is the first person who comes to mind when I think "How did I get here?". Over these years, he has not only supported me and my work, but has also provided me with a platform so rich in academic value and learning opportunities that I could never think of anything more a PhD student like me would have ever needed. I can say without hesitation that I owe the success of this work and the achievement of this doctorate to him.

That being said, I must also mention that if it were not for the wisdom of Prof. Andreas Lehrach, I would still have a writer's block at chapter 2! Not only did he take me in as a "free student" in his class on accelerator physics, but his timely insights and guidance is the foundation of every eventual finding. Simply put, if not for him, I'd now have a lot of numbers and still not know what I'm looking at.

Along with him, I was also lucky enough to have the guidance, expertise and resources of Dr. Jörg Pretz, Dr. Andro Kacharava, Dr. Volker Hejny, Dr. Richard Talman, and the experts within the JEDI and CPEDM collaborations. It is these amazing people who have taken me in at Jülich and made my stay at the Forschungszentrum both memorable and victorious. Just like in a certain universe, if not for the JEDI, there wouldn't be hope, just an ever-growing and all-consuming dark side…

And it is under this nurturing umbrella of hope, academia and research, that I have also made lifelong friends of wonderful colleagues like Max, Saad, Vera, Rahul (the other one…), Achim and Andrea. Even during weeks spent on sleepless nights working deadlines, it has been them that let me say "life was never short of absolutely worth living!".

I must also take a moment to reflect on the most influential teachers in my life: Dr. David Hamilton, Dr. David Ireland, Dr. Daria Sokhan and Prof. A N Garg, as well as the most important mentors: Dr. D Gopalani, Dr. S S Barala, Dr. A K Yadav, Dr. B Seitz, Dr. B S Tomar, and Dr. Sarmishtha Bhattacharya who nurtured my curiosity and shaped my attitude towards science and research.

But I must confess, it takes a strenuous perseverance and continuous dedication to make a work like this possible, and even when faced with prerequisites so high, the people in my life have always made putting all those hours never get to my soul. These are my friends: Namrata, Jaya, Vahini, Sudha, Roy, Sneha, Nandini, Satish, Michele, Aurora, Tannishtha, Shantanu, Trish, Adarsh, Mattia, Tais, Renato, Silvia, Seema, Smita, Samyak, Aayush and Mohit; and also my family: Mom, Dad, Vaishnavi, Rohit, Karthik and Aditya. Its already a pretty long list, and yet the paragraph feels incomplete: an inconvenient but beautiful reminder of exactly how blessed I am.

Am I forgetting someone?

I write this here, because a name on a list, or even "not just a colleague, but a friend" simply doesn't cut it… I'm talking about my "Light Saber": Nicola Canale, who with his masterful moves took away all possible forms of boredom, crises, cluelessness, doubt, and hopelessness. PhD's can be stressful, just like moving to a new country or learning a new language, but I can always stay calm since this guy makes me just enough of a scholar and also an "Italian" that I can live like I own the place. The only downside is that I also made him lose his own Italian-ness to become a "Punjabi" in the process!

I would have mentioned him earlier, but unfortunately, I am still waiting for him to finish reading my thesis… But hey Nicola! At least you got two whole paragraphs!

My last and most sincere thanks go to you, the reader of my thesis. You gave a purpose to me and a meaning to my work. I hope that reading this work gives you as much joy as it gave me writing it for you.

Thank you…

Table of Contents

Abstract iii
Acknowledgements v
1. Introduction 1
1.1 Scientific Motivation 4
1.1.1 Symmetries and transformations 5
1.1.2 $\mathcal{CP}$ violation in the Standard Model 7
1.2 Electric Dipole Moment 7
1.2.1 $\mathcal{CP}$ violation and EDM 8
1.2.2 Sources of $\mathcal{CP}$ violation that could contribute to a permanent EDM .9
1.3 Experimental searches for nucleon EDM 10
1.3.1 Direct measurement of neutron EDM 10
1.3.2 Measurement of nucleon EDM in diamagnetic atoms 12
1.4 Summary 12
2. Storage Ring Concepts 15
2.1 The Synchrotron 15
2.1.1 The RF cavity 16
2.1.2 The Quadrupole Magnet 18
2.1.3 The Sextupole Magnet 21
2.2 Frenet-Serret Coordinate System 22
2.3 Transverse Beam Dynamics in storage rings 23
2.3.1 Betatron Motion 23
2.3.2 Off-Momentum Particles and Dispersion 30
2.3.3 Chromaticity 31
2.3.4 Chromaticity correction by sextupoles 32
2.4 Longitudinal Beam Dynamics in Storage rings 33

2.4.1 Path Lengthening and momentum compaction 33
2.4.2 Synchrotron frequency 36
2.5 6D Phase Space and Transfer Matrices 40
2.5.1 Symplectic Condition 41
2.6 Spin Dynamics in Storage rings 42
2.6.1 Spin Precession 42
2.6.2 Spin transfer matrix 45
2.6.3 Polarisation vector for fermions 48
2.6.4 Spin resonances 49
2.6.5 Spin coherence time and spin tune spread 50
3. EDM Measurement using Spin Precession in Storage Rings 53
3.1.1 Strategy at pure magnetic storage rings 53
3.1.2 Strategy at combined-field storage rings 56
3.1.3 Strategy at pure electrostatic storage rings 56
3.2 Stages of the EDM experiment 57
3.2.1 Precursor stage: COSY 58
3.2.2 Proof-of-concept stage: The Prototype EDM Storage ring 59
3.2.3 Final experiment stage: pure-electric storage ring 62
4. The Precursor Experiments at COSY 65
4.1 Spin Coherence Time Study 65
4.1.1 Experimental setup 65
4.1.2 Experimental Results 66
4.2 Deuteron EDM Measurement 67
4.2.1 Experimental Setup 67
4.2.2 Methodology 68
4.2.3 Experimental results 69
5. Simulations of the Prototype Storage Ring 71
5.1 BMAD 71
5.2 The Prototype Lattice “V3” 72
5.2.1 Dipole magnet settings 73

5.2.2 Quadrupole and sextupole magnet settings 74
5.3 Measurement of Twiss Parameters 74
5.4 Parameter Space 75
5.4.1 First-order optical parameters 75
5.4.2 Second-order optical parameters 77
5.4.3 Structure and organization of parameters 79
5.4.4 Choice of first working point 80
5.4.5 C-matrix 81
5.5 Investigations of Spin Decoherence 81
5.5.1 Decoherence in frozen spin 82
5.5.2 Beam Distribution 83
5.5.3 Parallelization Scheme 83
5.5.4 Time development of polarisation vector magnitude 84
5.5.5 Variation of spin tune error with second-order optics 89
5.5.6 Measuring spin coherence time 90
5.5.7 Variation of spin coherence time with second-order optics 92
5.6 Grid tests 93
5.6.1 Grid test 1 93
5.6.2 Grid test 2 94
5.7 Maximum Spin Coherence Time and Analysis of Grid test Results 98
5.8 Optimization of working point 100
5.8.1 Longitudinal stability 101
5.8.2 Betatron and spin resonances 101
5.8.3 Beam Lifetime 102
5.9 Lattice-wide Optimization Survey 104
6. Results and Discussion 105
6.1 Achievements of this study 105
6.2 Optimization method 107
6.3 Optimized working points 108
6.3.1 Measurements of lower limits 109

6.3.2 Measurement of chromaticity tolerance 109
6.4 Discussion on lattice performance 110
7. Outlook: Areas yet to be Explored 113
7.1 A Racetrack Lattice 113
7.2 An improved Four-fold Symmetry Lattice 114
8. Summary and Conclusion 117
9. References 119
10. List of Figures 127
11. List of Tables 135
12. List of Equations 137

To Amama…

1. Introduction

The aim of physics is to arrive at a description of the universe through models, often expressed in the language of mathematics, that are capable of making accurate predictions about the fate of the systems within its realms. Apart from this, physics also aims to answer one of humanity's most burning questions: "Why do we exist?".

Over millennia of resilience in searching for answers, physics has made remarkable progress in understanding the origins and the evolution of the universe. Since the discovery that apart from energy, the universe is made up of matter and antimatter, the problem whose solutions continue to elude physicists to this day is the matter antimatter asymmetry observed in the universe [1]. While matter and antimatter can be seen as two sides of the same "universal coin", when seen from the perspective of processes like pair production and annihilation, the very fact that we exist, implies a fundamental phenomenon that skews the universe in favour of matter.

Based on what physics has uncovered so far about the workings of the universe, the dominance of matter over antimatter can only occur if certain conditions are met. The most important of these conditions, which were put forward by Sakharov [2], is the violation of certain fundamental symmetries.

One of the most successful and most contested theories in physics today, is the standard model. It is in fact the theory that has come the closest to being a theory of "everything except gravity"! However, if every postulate of this theory were true, then $\mathcal{CP}$ violation, which is one of those necessary violations of fundamental symmetries, would be occurring too rarely to explain the dominance of matter. Fortunately, there are other theories which predict higher $\mathcal{CP}$ violations which may even account for this asymmetry. These are known as BSM theories or theories "Beyond the Standard Model", which forms the inspiration of a large portion of fundamental physics research today.

One of the avenues to search for $\mathcal{CP}$ violation is to look for a permanent electric dipole moment (EDM) of a fundamental particle, which is a direct manifestation of the phenomenon. In other words, the EDM of fundamental particles is a very sensitive probe of $\mathcal{CP}$ violation. The measurement of EDM could therefore enable the extension of the standard model and bring physics closer to understanding the matter antimatter asymmetry observed in the universe.

This being said the measurement of EDMs in fundamental particles can be tricky since it requires a very high systematic and statistical sensitivity [3]. The search for a permanent EDM in neutral particles has been underway for decades, without ever observing a non-zero value with enough certainty [1]. So, the idea which may seem intuitively trickier, of measuring the EDM of charged particles, has received much attention in recent years. While neutral particles can be trapped at rest, charged particles must be confined in motion, which is achieved using storage rings. This method was performed successfully for the measurement of the EDM of muons as a part of the famous g-2 experiment [4]. While the gyromagnetic anomaly of protons being positive as compared to the near-zero value of muons makes it more challenging to measure its EDM, future experiments for the direct measurement of the proton EDM have been proposed in dedicated storage rings [5] [6]. To overcome the challenge of the non-zero gyromagnetic anomaly of the proton, the storage rings must either operate with only electric fields or a combination of both electric and magnetic fields.

The Jülich Electric Dipole moment Investigations or "JEDI" collaboration aims to build such a dedicated storage ring. This dedicated storage ring will perform the measurement by putting the particles in a "frozen spin" state, meaning that the particles which are injected into the ring with spins that are aligned with their momentum will, if not for the effect of an EDM, continue to stay aligned with the momentum at all times. This isolates the EDM effect from other storage ring phenomena, thus allowing for a direct measurement.

By running precursor experiments on an existing storage ring [7] which only uses magnetic fields, the JEDI has accumulated crucial data on the systematics of a proton EDM experiment at a dedicated all-electric ring and conducted a feasibility study [8]. At this existing storage ring known as COSY, located at the Jülich Forschungszentrum in Jülich, Germany, JEDI has also performed a direct measurement of the deuteron EDM, whose preliminary results were recently presented [9].

However, despite the remarkable experimental achievements at COSY, there still exists a vast divide in the systematics, the working principles and the operating circumstances between COSY and the dedicated all-electric ring. To bridge this gap, the JEDI collaboration proposes to build and conduct experiments at a prototype storage ring. This ring will be the first storage ring to achieve frozen spin for protons and will use a combined electric and magnetic field for confinement.

The ring is currently being investigated for its performance and sustainability via simulations of beam and spin dynamics on a software adaptation of the original design proposed by JEDI.

This thesis presents one such simulation study of an idealised model of the prototype storage ring. Through simulations of beam and spin dynamics of a frozen spin bunch of particles using the BMAD software toolkit, this thesis will explore the nature of frozen spin storage of particles with simultaneous electric and magnetic fields, observe and model the various effects that modify particle spin and the overall bunch polarization, and conclude with a method to optimise the parameters of the beam to maximize the sensitivity of a potential EDM measurement. The structure of this thesis is outlined here:

The following sections of this chapter briefly describe the scientific motivation behind the experiment to measure proton EDM: the matter-antimatter asymmetry, $\mathcal{CP}$ violation as a possible source, the $\mathcal{CP}$ violating nature of EDM, and past attempts at measuring it.

Chapter 2 goes into detail about the specific formalisms used to describe the beam and spin dynamics in particle storage rings. Relevant parameters as well as specific terminology which characterise the particle motion, such as betatron tunes, spin tunes, chromaticity, and also spin coherence time are defined and described here.

Chapter 3 applies the specific concepts discussed in the previous chapter, to the task of measurement of proton EDM. Technical details of possible strategies to measure EDM using devices of different specificity are discussed along with methods of managing systematic uncertainties. This chapter also outlines the staged approach employed by JEDI to achieve its goal of a precise measurement of proton EDM.

Chapter 4 gives relevant details about the precursor experiments conducted by JEDI at COSY.

Chapter 5 describes in detail the simulation study performed on the prototype storage ring model, the tools used, the parameters explored, as well as the strategy developed to optimise these parameters to maximise the precision and sensitivity of the storage ring to the proton EDM measurement.

Chapter 6 presents the results of tests of this optimisation strategy at various beam configurations of the idealized prototype ring model, as well as a discussion on the implications of these results.

Chapter 7 discusses possible directions for future research in this area.

Finally, chapter 8 summarises the outcomes of this study and concludes the thesis.

1.1 Scientific Motivation

For a while now, physics has been grappling with one of its most puzzling questions: "why is there more matter than antimatter in the universe?"

From what is known about the history of the universe, shortly after the big bang it went to a phase of rapid exponential expansion, in a process called inflation [10]. After inflation stopped, the temperatures in the universe were still high enough that particle antiparticle pairs could continue to be produced at thermal equilibrium, in a process called pair production [11]. Once the universe cooled down just enough so that pair production was no longer accessible, the matter produced quickly began to annihilate with the antimatter, into photons (see Figure 1). However, at the end of this annihilation phase the universe somehow had lots of matter left over which would not exist, if matter and antimatter exhibited similar behaviour. This is known as the matter-antimatter asymmetry, and a reliable quantity to measure it is the baryon asymmetry number:

$$\eta_{B\bar{B}} = \frac{N_B - N_{\bar{B}}}{N_\gamma} \qquad \{1\}$$

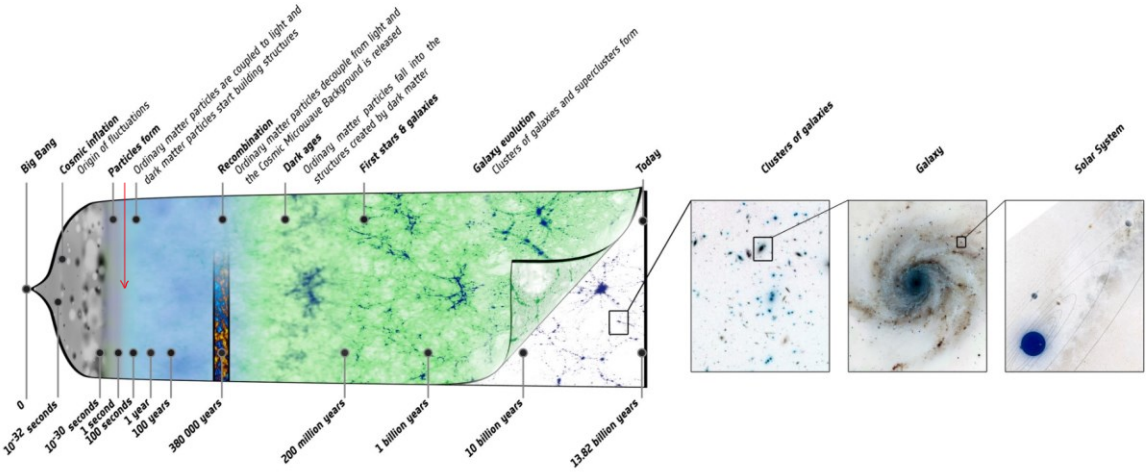

Figure 1: A depiction of the history of the universe from the Big Bang until today, where the timescale is represented as labels at the bottom, and our solar system's location (not to scale) is pointed out on the right. Pair production was no longer accessible since after the lepton epoch (marked with a red arrow), somewhere between 10 and 100 s after the big bang, after which the matter-antimatter asymmetry became a permanent feature of the universe.

Here, N_B is the baryon density, $N_{\bar{B}}$ is the antibaryon density, and N_γ is the cosmic background radiation photon density just before the baryon annihilation. The baryon asymmetry number was accurately measured by two experiments: one

which determined the abundance of light elements produced during big bang nucleosynthesis (BBN), and the other that observed temperature fluctuations in the cosmic microwave background within the Wilkinson microwave anisotropy probe (WMAP). The numbers measure by these experiments [12] (observations) show reasonable agreement with each other.

However, the estimations based on the standard model [12] seem to not agree with their measurements. Shown below are the numbers measured by each experiment.

$$\begin{gathered}\eta_{B\bar{B}}^{BBN} = 6.07^{+0.33}_{-0.33} \times 10^{-10} \\ \eta_{B\bar{B}}^{WMAP} = 6.16^{+0.153}_{-0.156} \times 10^{-10} \\ \eta_{B\bar{B}}^{SM} \approx 10^{-18}\end{gathered} \qquad \{2\}$$

Physicists are currently exploring two avenues that might explain this imbalance. One theory is that our galaxy and its neighbourhood exist in a part of the universe that is dominated by matter, implying that there may be other parts which might be dominated by antimatter. This is being explored by experiments such as the alpha magnetic spectrometer (AMS) [13], a cosmic ray detector on the International Space Station, in its search for antimatter and its related signatures.

The other theory is that baryogenesis and baryon annihilation are fundamentally asymmetric processes. For this to be true, certain conditions need to be met. These were summarised by Andrei Sakharov in 1967 [2]:

- **Violation of baryon number**: since the number of the universe was initially 0, a baryon number violation is necessary for there to be an excess of baryons.
- **Violation of $\mathcal{C}$ and $\mathcal{CP}$ symmetries**: a disparity in the probability of particle and antiparticle creation can only exist if the symmetries of charge conjugation ($\mathcal{C}$) and simultaneous charge-parity conjugation ($\mathcal{CP}$) are violated.
- **Violation of thermal equilibrium**: if the asymmetric baryogenesis is in thermal equilibrium then the rate of the forward process would be the same as that of the reversed one, preventing the build-up of the excess baryons.

Among these, the second requirement has received a lot of attention from physicists in recent years due to the vast disagreement between theory and observation. So, the concepts of discrete symmetries and their violations are discussed below.

1.1.1 Symmetries and transformations

Symmetry is the term used to refer to a system which is invariant under certain transformations. For instance, if a system is unchanged after rotating it, the system

is said to have rotational symmetry. Rotational symmetries are an example of a continuous symmetry. But in the context of the Sakharov conditions, the concept of interest is discrete symmetries, in which systems remain invariant under discrete transformations.

1.1.1.1 Parity transformations

A system having parity ($\mathcal{P}$) symmetry remains invariant after one of its spatial dimensions are inverted. In other words, the system remains in invariant after being mirror-reflected. If the "state" of the system is given by the function $\Psi(x,t)$ which depends on its spatial position at a given time, then a party transformation can be represented as:

$$\Psi(x,t) \underset{\mathcal{P}}{\rightarrow} \Psi(-x,t) \qquad \{3\}$$

Here, the "reflection" is implemented with the reversal of the spatial dimension x of the system. Parity violations were first observed by Wu [14] in the beta decay of $^{60}_{27}Co$.

1.1.1.2 Charge conjugation transformation

A charge conjugation transformation turns a system's particles into antiparticles: It is denoted by:

$$\Psi(x,t) \underset{\mathcal{C}}{\rightarrow} \overline{\Psi}(x,t) \qquad \{4\}$$

…where the bar represents the same system, but with antiparticles instead of particles. Violations of the $\mathcal{C}$ symmetry can be seen within the standard model itself, where neutrinos with spins aligned with their momentum undergo weak interactions whereas antineutrinos with spins aligned with their momentum do not.

1.1.1.3 Time Reversal transformation

A time reversal transformation reverses the flow of time, essentially reversing the direction of all moving objects in the system:

$$\Psi(x,t) \underset{\mathcal{T}}{\rightarrow} \Psi(x,-t) \qquad \{5\}$$

Violations of the time reversal symmetry were observed in 1998 by the CPLEAR collaboration, with an experiment based at CERN, on the neutral kaon system [15].

1.1.1.4 $\mathcal{CPT}$ Theorem

$\mathcal{CPT}$ symmetry being obeyed by a system is a requirement of the Lorentz-invariant local quantum field theory, within which each combination of all the three transformations results in a symmetric process [16]. This is known as the $\mathcal{CPT}$ theorem.

1.1.2 $\mathcal{CP}$ violation in the Standard Model

A $\mathcal{CP}$ transformation is a combined transformation of a system, where a $\mathcal{P}$ transformation is followed by a $\mathcal{C}$ transformation. $\mathcal{CP}$ violation was first observed in the neutral kaon sector, by the famous Fitch-Cronin experiment [17] in 1964, and the evidence has been widespread in experiments and reviews ever since. This eventually led to the incorporation of $\mathcal{CP}$ violation into the standard model via the Cabbibo-Kobayashi-Maskawa, or CKM matrix, which describes in its elements, the strength of the flavour-changing weak interactions, and the strength of the $\mathcal{CP}$ violation in its phase angle [18].

While this formalism has been successful in explaining the observed $\mathcal{CP}$ violation in the weak sector, comparable effects have not been found in the strong sector, despite the Lagrangian of Quantum Chromodynamics having $\mathcal{CP}$ violating terms. This is known as the strong $\mathcal{CP}$ problem [19]. Furthermore, the predictions of the CKM matrix still do not account for the matter-antimatter asymmetry observed in the universe [20]. Therefore, efforts are being made by the physics community to find additional sources of $\mathcal{CP}$ violation, many of which may manifest as a permanent electric dipole moment of a particle.

1.2 Electric Dipole Moment

The basic definition of an Electric Dipole Moment (EDM) is given by the shift in the "centre of charge" of a system, which for a continuous system located at the origin, can be expressed by:

$$\vec{d} = \int \rho(\vec{r})\vec{r} \cdot d\vec{r} \qquad \{ 6 \}$$

…which is analogous to the expression for the Magnetic Dipole Moment (MDM), given by:

$$\vec{\mu} = \int \left(\vec{r} \times \vec{j}(\vec{r})\right) \cdot d\vec{r} \qquad \{ 7 \}$$

Here, the integrals are over all space, and $\rho(\vec{r})$ and $\vec{j}(\vec{r})$ are the charge and current densities at a location $\vec{r}$ from the origin.

Since at the particle level, the only quantization axis available is the spin axis, these quantities can be represented as multiples of the spin:

$$\vec{\mu} = g\frac{q}{2m}\vec{\boldsymbol{s}}$$
$$\vec{d} = \eta\frac{q}{2mc}\vec{\boldsymbol{s}} \qquad \{8\}$$

Here, q and m are the charge and mass of the particle, c is the speed of light. g and η are dimensionless quantities, known as the gyromagnetic and gyroelectric ratios.

1.2.1 $\mathcal{CP}$ violation and EDM

The presence of a permanent EDM on fundamental particles would violate $\mathcal{P}$ and $\mathcal{T}$ symmetries. This can be demonstrated by defining the state of the system in an external magnetic and electric field as a Hamiltonian, which has both MDM and EDM terms:

$$H = -\vec{\mu}\cdot\vec{B} - \vec{d}\cdot\vec{E} \qquad \{9\}$$

Applying the $\mathcal{P}$ and $\mathcal{T}$ operators on this system would modify the system and thus the Hamiltonian. If the Hamiltonian changes in value, the system is said to violate the symmetry.

Applying the $\mathcal{P}$ transformation on the Hamiltonian would reverse the direction of a spatial dimension, also reversing the charge distribution across space, and thus the direction of the electric field. However, magnetic fields wouldn't be affected since they are generated by circular currents. Similarly, the particle spin and its associated properties also remain invariant.

Applying the $\mathcal{T}$ transformation reverses the direction of all moving objects, including spins and currents. The only thing that remains invariant is the electric field. The effect of these transformations is also depicted in Figure 2.

The Hamiltonian under the transformations would become:

$$\mathcal{P}(H) = -\vec{\mu}\cdot\vec{B} + \vec{d}\cdot\vec{E}$$
$$\mathcal{T}(H) = -\vec{\mu}\cdot\vec{B} + \vec{d}\cdot\vec{E} \qquad \{10\}$$

Both these systems would thus be energetically different as compared to the original system, which establishes the symmetry violations. By the $\mathcal{CPT}$ theorem, it can also be said that this system is $\mathcal{CP}$ violating.

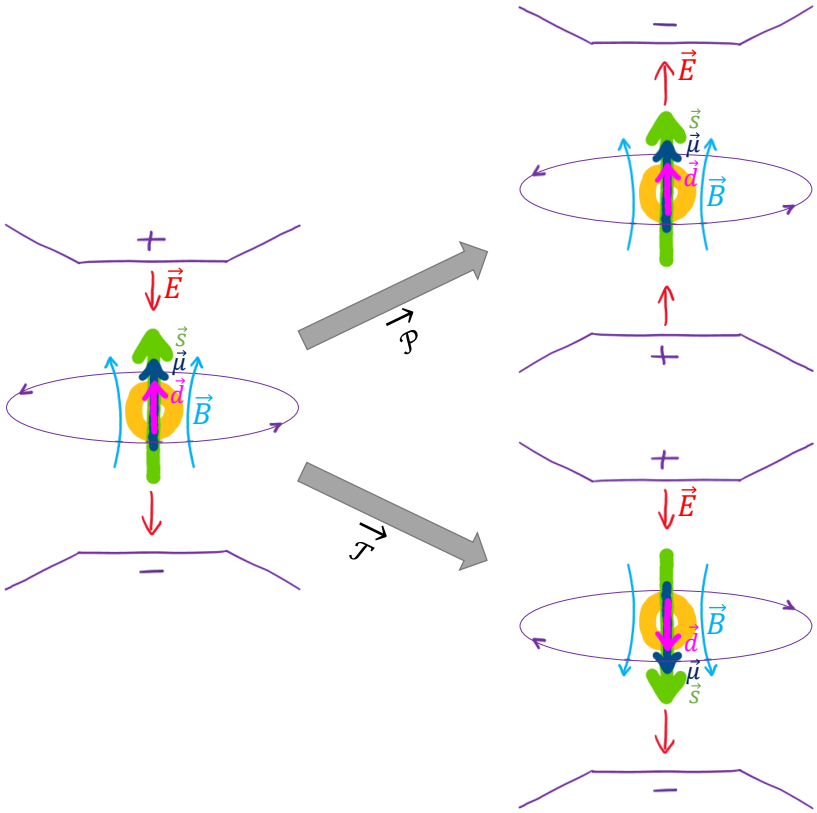

Figure 2: The effect of parity and time reversal transformations on a particle (yellow) with an electric dipole moment (magenta) being subject to an external electric field (red) via electrodes, and magnetic field (blue) via a current carrying coil. The parity transformation (inversion of the vertical coordinate) flips the electrodes while leaving the intrinsic moments and magnetic field invariant. The time reversal flips the intrinsic moments and the magnetic field but leaves the electric field invariant. Both transformed systems would behave differently than the original, thus demonstrating the violations of the transformations.

1.2.2 Sources of $\mathcal{CP}$ violation that could contribute to a permanent EDM

From within the weak sector of the standard model, $\mathcal{CP}$ violation accounts for an EDM of [21]

$$d_n^{CKM} \approx 10^{-32}\, e \cdot cm \qquad \{ 11 \}$$

…for neutrons, as calculated from the CKM matrix. The strong sector places a slightly higher upper limit on the same value:

$$d_n^{\bar{\theta}} < 1.1 \times 10^{-26}\, e \cdot cm \qquad \{ 12 \}$$

Since the predictions of the strong sector are currently challenged by the strong $\mathcal{CP}$ problem, the one from the weak sector is currently considered the upper limit of the standard model.

Apart from just the standard model, there are sources of $\mathcal{CP}$ violation that come from models beyond as well (BSM models). These sources are summarized in Figure 3 [22] [21].

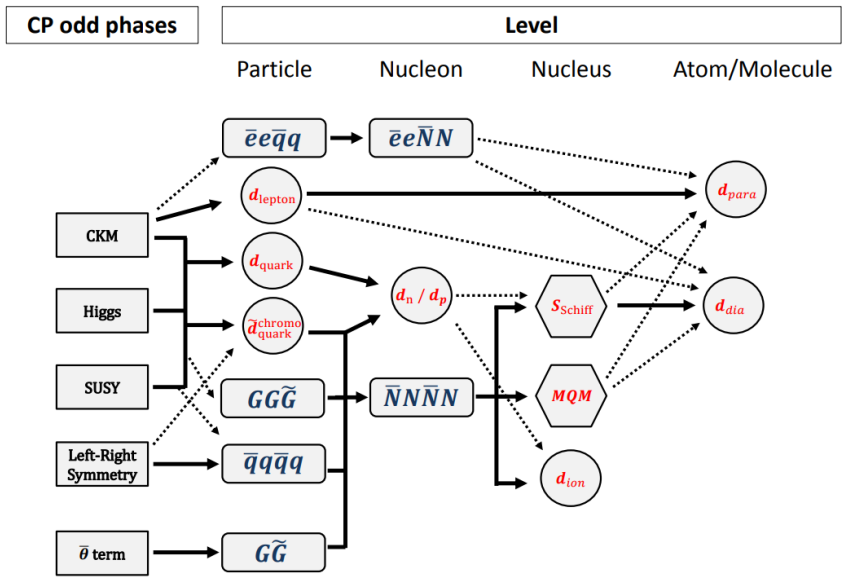

Figure 3: The connection of CP violating sources and the EDMs of various particles. The different momenta (EDM, magnetic quadrupole moment and Schiff moment) are shown in red; the effective couplings are shown in blue. Solid arrows represent a stronger contribution than dashed arrows. [22]

1.3 Experimental searches for nucleon EDM

In pursuit of validating the predictions of nucleon EDM by the standard model as well as looking for additional sources of $\mathcal{CP}$ violation, experiments were performed by physicists to measure the EDM of nucleons. Two of the most noteworthy are described here.

1.3.1 Direct measurement of neutron EDM

The first EDM measurement was performed on neutrons, specifically those produced by the Oak Ridge nuclear reactor. The experiment generated an EDM signal from these neutrons using the Ramsey method [23]. A schematic of the experiment is shown in Figure 4.

The Ramsey method involves five steps:

1. Neutrons are created in the reactor and undergo spin-dependent reverse scattering on a magnetic mirror, which renders them spin-polarized along the vertical axis. These neutrons are then guided through to the main apparatus.
2. While passing through the apparatus, an RF magnetic field is created by a coil. The frequency of the field is adjusted to the Larmor frequency of the neutrons in the main magnetic field. The solenoidal field slowly moves the polarization into the plane perpendicular to the main magnetic field. This is called a $\pi/2$-pulse.

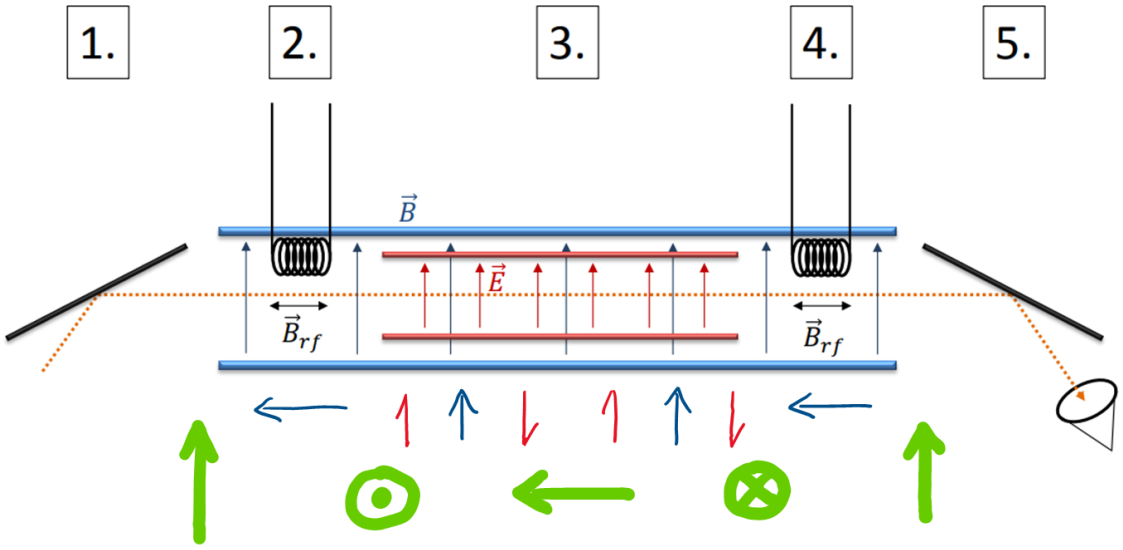

Figure 4: A schematic of the neutron EDM experiment using the Ramsey method, with the stages marked on top, and the neutron polarisation direction at those stages are marked in green below. The blue arrows indicate the direction of the magnetic field at each step. The red half arrows indicate that the electric field is flip-flopped to generate a variation in the EDM signal. [22]

3. the neutron sample enters a region of superimposed static magnetic and electric fields. Both fields are either aligned or anti-aligned to each other as the electric field is varied sinusoidally. Together, they introduce a precession of the perpendicular polarization whose frequency is given by (the plus or minus depends on the current direction of the electric field):

$$\omega = \frac{2|\mu B \pm dE|}{\hbar} \qquad \{13\}$$

4. A second RF magnetic field induces another $\pi/2$-pulse to the spins of the neutrons. The frequencies of the RF fields in steps 2 and 4 are equal and the phases are adjusted to be equal to each other. Only the perpendicular polarization component, which is in phase with the RF field, flips slowly to the vertical direction, while the other component is essentially unchanged. Therefore, the vertical polarization serves as a measure for the EDM.
5. The vertical polarization is measured by using the spin-dependent scattering on a magnetic mirror and counting the reflected neutrons.

The results of this experiment yielded an upper limit on the neutron EDM of about $5 \times 10^{-20} e \cdot cm$, and this method became the standard method for neutron EDM measurement. Since the original experiment, further advances were made in terms of technique as well as precision. The current, most stringent limit on the Neutron EDM is [24]:

$$|d_n| < 2.9 \times 10^{-26} e \cdot cm \qquad \{ 14 \}$$

1.3.2 Measurement of nucleon EDM in diamagnetic atoms

In diamagnetic atoms, the finite size of the nucleus as well as magnetic and higher-order interactions between nucleons and electrons give rise to an atomic EDM [25]. The so-called Schiff moment is created by $\mathcal{CP}$ violating nuclear forces. It can arise from the nucleon EDMs and $\mathcal{CP}$ violating nucleon-nucleon interactions and contributes to the electrostatic potential. Its interaction with the atomic electrons is the major contribution to the atomic EDM. This allows to deduce limits to the proton EDM using measurement in diamagnetic systems. Currently, the best limit was obtained in a measurement using mercury $^{199}_{80}Hg$:

$$\left|d(^{199}_{80}Hg)\right| < 3.1 \times 10^{-29} e \cdot cm \qquad \{ 15 \}$$

…which upon calculation of the Schiff's moment [26], leads to the indirect estimate of the proton EDM:

$$\left|d_p\right| < 7.9 \times 10^{-25} e \cdot cm \qquad \{ 16 \}$$

1.4 Summary

To briefly summarise the outcomes of the efforts to measure the EDM of nucleons, Table 1 shows the currently established upper limits of the most commonly measured particles.

Table 1: The current upper limits on the EDM searches in nucleons and leptons, mentioned along with confidence levels. The measurement of the proton and the electron are from indirect measurements whereas the neutron, the muon and mercury were measured directly. [22]

System	Current EDM Limit
Neutron	$2.9 \cdot 10^{-26}\, e\,\mathrm{cm}$ (90 % C. L.)
^{199}Hg	$3.1 \cdot 10^{-29}\, e\,\mathrm{cm}$ (95 % C. L.)
Proton	$7.9 \cdot 10^{-25}\, e\,\mathrm{cm}$ (95 % C. L.)
Electron	$8.7 \cdot 10^{-29}\, e\,\mathrm{cm}$ (90 % C. L.)
Muon	$1.8 \cdot 10^{-19}\, e\,\mathrm{cm}$ (90 % C. L.)

These measurements set stringent limits to extensions to the SM. For protons and electrons, the illustrated limits are deduced from indirect measurements in atoms and molecules, whose extraction requires a precise knowledge of the theory describing these systems. Direct measurements of these EDMs could exclude uncertainties, verify the theoretical calculations, and allow the distinction of different $\mathcal{CP}$ violating sources. For charged particles, direct measurements in storage rings are both, an excellent opportunity, as well as a daunting challenge.

To approach this challenge, the JEDI (Jülich Electric Dipole moment Investigations) collaboration was created in the end of 2011. The collaboration is currently based in the Forschungszentrum, Jülich, Germany, and is presently involved in spin physics experiments at the Cooler Synchrotron (COSY), located in the same facility. JEDI aims to carry out a long-term project for the measurement of the permanent electric dipole moments of charged particles in a storage ring [27], and the work of this thesis forms a part of this project.

The following chapters will introduce the concepts of beam and spin dynamics in storage rings, and then proceed to highlight the outcomes of this study as well as JEDI with respect to the ongoing efforts to measure the EDM of nucleons

2. Storage Ring Concepts

The term "ring", used widely in this work, refers to a particle accelerator that typically uses magnetic and/or electric fields to maintain moving particles on a fixed closed loop. More specifically, it refers to a synchrotron, which is a particle accelerator characterised by its use of Radio-Frequency (RF) cavities for acceleration and "bunching" of particles, and the synchronised variation of its bending fields in response to the increased momentum of the accelerated particles to maintain the radius of curvature, and thus, the fixed path of the particles.

This chapter will introduce the concept of synchrotrons and how they work. Subsequently, it will dive deeper into the specific nature of the beam, how it is maintained in the ring, the parameters to keep in mind and the perspective with which the problem is viewed. Further, the chapter discusses how the spin of the particle behaves in the system, the physics behind its variation over time, and finally, some ways in which these physical workings can be exploited to measuring the EDM of the charged particles in the ring.

2.1 The Synchrotron

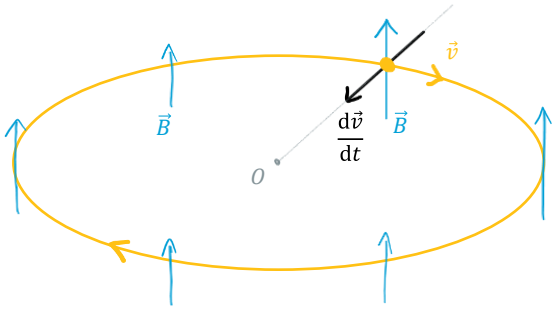

Figure 5: A depiction of particle motion in a synchrotron. A particle with a positive charge ends up traversing a circular path under the influence of a magnetic field of a specific value uniformly maintained along the desired path. The direction of the acceleration is always along the radial direction.

As mentioned earlier, a synchrotron is essentially a confinement system used to maintain moving charged particles in a fixed closed loop. A simple test case of a synchrotron is a particle with velocity $\vec{v}$ moving under the influence of a uniform (dipole) magnetic field $\vec{B}$ such that $\vec{B} \perp \vec{v}$. Figure 5 shows one such case where particles are made to follow a circular path on a horizontal plane with magnetic fields pointing vertically downward. This is possible due to the nature of the Lorentz force [28] acting on the particle:

$$\vec{F}(t) = m\frac{d\vec{v}(t)}{dt} = q\left(\vec{v}(t) \times \vec{B}\right) \quad \{ 17 \}$$

Here, $\vec{F}(t)$ is the force acting on the particle, and m and q are its mass and charge. The force which is directed radially inward is modelled by the centripetal force associated with the radius of curvature ρ of the path:

$$F = q\left|\left(\vec{v}(t) \times \vec{B}\right)\right| = qvB = \frac{mv^2}{\rho} \quad \{ 18 \}$$

This gives us the relationship between the ring's radius and the applied magnetic field:

$$B = \frac{mv}{q\rho} \quad \{ 19 \}$$

By this, we know that for a constant magnetic field, the radius of curvature of the path remains constant, i.e. the particle moves in a circular path. { 19 } also gives the exact field to set in order to maintain a particle with a given mass, charge and velocity on a circular path of radius r. Thus, if the particle were to be accelerated, the field must increase accordingly to maintain the motion path.

It is also interesting to see that { 19 } also holds true for relativistic particles as seen from the lab frame, if the mass in consideration is corrected to the relativistic mass:

$$B = \frac{\gamma mv}{q\rho} = \frac{p}{q\rho} \quad \{ 20 \}$$

…where γ is the Lorentz factor. With a setup to maintain particles at a fixed momentum in a simple closed orbit, the synchrotron would be much more useful with the ability to change the momentum of these particles. Moreover, since particle beams in practice aren't always following the path designed for it to follow, contingencies need to be put in place to recover particles that have strayed off the designed path both in terms of position and momentum. While there are several devices available to achieve these tasks, this work describes the ones in use for JEDI's experiments [8].

2.1.1 The RF cavity

A Radio-Frequency (RF) cavity is a device used to accelerate particles along a straight beamline. The name "cavity" is a reference to the structure of the device, which is essentially designed as a series of cylindrical "poles" with periodic gaps or

"cavities" in between. This specific design is used to create strong electric fields precisely in the longitudinal direction in a way that doesn't obstruct the path of the particles. The poles act as electrodes held at different voltages and the cylindrical symmetry between the poles ensure that all transverse field components get cancelled out.

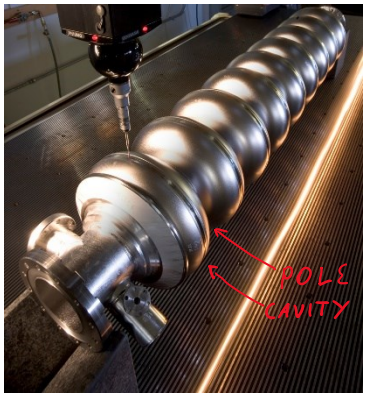

Figure 6: A photograph of a RF cavity being tested by TRIUMF at the University of Toronto [78], with markings showing the cylindrically symmetric poles and cavities.

To ensure that moving particles receive a constant field, the voltage V_c applied on the device is a RF voltage which varies sinusoidally with time t and position x along the device:

$$V_c(x,t) = V_{c_0}\sin(k_c x - \omega_c t + \phi) \qquad \{ 21 \}$$

Here, $k_c = {}^{\pi}/_{2d_c}$ where d_c is the distance along the device between a cavity and a pole. $\omega_c = 2\pi\nu_c$ where ν_c is the frequency of the RF voltage in Hz, and ϕ is the phase adjustment. Figure 7 shows the RF voltage (the red curve) put in practice for particle acceleration. The accelerator works well if the phase velocity $v_{RF} = {}^{\omega_c}/_{k_c} = 4d_c\nu_c$ of the voltage is maintained equal to the particle velocity. If this is the case, the particle feels the same potential, and thus the same accelerating field at all times.

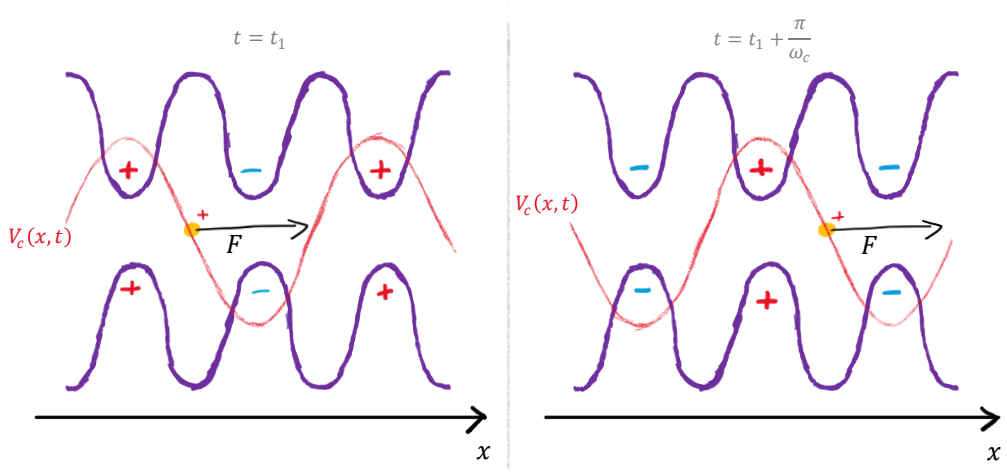

Figure 7: A schematic showing the cavity structure (violet) and the effective charges on the poles due to the applied RF voltage. The red curve shows the spatial variation of the voltage. The right side shows the same setup as the left, but half a time-period later. If the phase ϕ is adjusted so that the particle always feels a negative slope, and the frequency ν_c is varied so the phase velocity of the voltage is always equal to the particle velocity, the particle can receive a constant field for a steady acceleration.

The troughs, or lower ends of this curve are termed as the RF "buckets". This is because particles that travel at $v = v_{RF}$ and are exactly at the trough experience no acceleration. Moreover, particles that are slightly ahead receive a decelerating field whereas particles slightly behind receive an accelerating field. The same also applies if the particle velocity is slightly off v_{RF}. Slightly slower particles eventually lag behind and receive an accelerating field, while slightly faster particles eventually take a lead to receive a decelerating field.

This phenomenon effectively makes the voltage troughs into buckets or moving potential wells that transport particles (see Figure 18 [29]). In these buckets, particles with slight phase-space deviations (in position or momentum) from the bucket centers end up stably oscillating around it.

In such a paradigm, particle acceleration is carried out by gradually increasing the RF frequency ω_c, and thus, the velocity of the buckets (v_{RF}). However, for the purposes of a storage ring, RF cavities are primarily used for their bunching effects and maintaining the desired momentum of the particles. Thus, in a storage ring, v_{RF} is kept constant.

2.1.2 The Quadrupole Magnet

A quadrupole magnet (or simply, quadrupole) is a device used to keep particles as close to the center of the beamline as possible by recovering particles that have strayed off the designed path. It is a magnet with four poles arranged along the diagonals on the plane transverse to the beam propagation axis. One such configuration is depicted in Figure 8. The poles are typically those of electromagnets, and each of the coils around the cores carry the same current so that each of the poles produce the same magnetic flux.

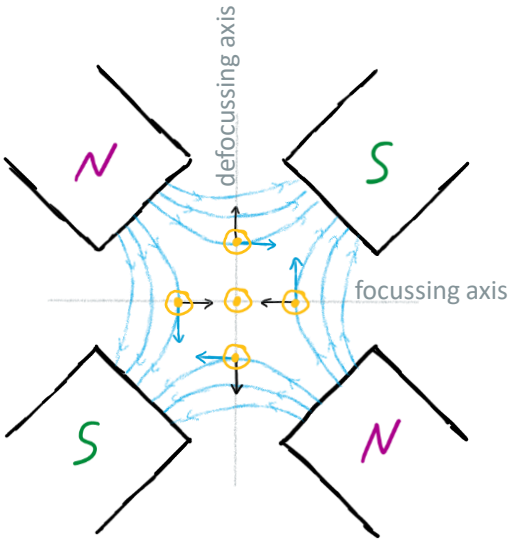

Figure 8: The arrangement of poles and the consequent field configuration of a focussing quadrupole. The diagram shows five particles at different transverse positions, all moving in the direction pointing out of the page, as well as the respective forces (black arrows) they experience due to the local magnetic field (blue arrows) they perceive.

When particles move along the longitudinal axis through this system, any particle passing through the central axis would experience no force due to the system's symmetry along the diagonal axes. However, particles which are slightly offset along the transverse plane's horizontal axis would experience a Lorentz force pushing it towards the centre. On the other hand, those which

are slightly offset along the vertical axis would experience a force pushing it away from the centre. This effect renders the horizontal axis to be the "focussing" axis and the vertical axis to be the "defocussing" axis.

Quadrupoles are typically characterised by the effect they have on particles travelling on the horizontal plane (the plane of the ring). Thus, the configuration of Figure 8 is a focussing quadrupole. If the poles were switched from North to South and vice-versa, the horizontal axis would become the defocussing one while the vertical axis would become the focussing one. Such a quadrupole would be termed a defocussing quadrupole.

Another interesting feature of a quadrupole is that the further along an axis the particle proceeds, the lesser the distance becomes between the opposing poles, and thus, the stronger the field perceived. Quadrupoles are generally designed so that the increase in the perceived field strength along the axes is linear. This way, the transverse magnetic field of a quadrupole is expressed by:

$$\vec{B} = \kappa(x\hat{y} + y\hat{x}) = \kappa\begin{pmatrix} y \\ x \end{pmatrix} \quad \{ 22 \}$$

Here, κ is a constant called the quadrupole field strength, measured in T/m (Tesla per metre). The value of κ now characterises the quadrupole: positive values imply a focussing quadrupole whereas negative values imply a defocussing one. With this expression for the field, the Lorentz acceleration experienced by a particle at a location $\vec{r} = \begin{pmatrix} x \\ y \end{pmatrix}$ on the transverse plane is given by:

$$\frac{d^2\vec{r}}{dt^2} = \frac{q}{m}\vec{v} \times \vec{B} = \kappa\frac{q}{m}\begin{pmatrix} 0 \\ 0 \\ v \end{pmatrix} \times \begin{pmatrix} y \\ x \\ 0 \end{pmatrix} = \kappa\frac{qv}{m}\begin{pmatrix} -x \\ y \end{pmatrix} \quad \{ 23 \}$$

This gives us the independent expressions:

$$\frac{d^2x}{dt^2} = -\kappa\frac{qv}{m}x \quad \{ 24 \}$$

$$\frac{d^2y}{dt^2} = \kappa\frac{qv}{m}y \quad \{ 25 \}$$

The linear dependence of the acceleration with the transverse coordinate means that the quadrupole works for charged particles exactly like a thin lens works for light. To see how this is true, the situation shown in Figure 9 is considered, where a "paraxial" (longitudinally propagating) particle is impinged on the quadrupole such that it crosses the transverse plane at a point δ on the focussing axis. Assuming

that the quadrupole field is effective in a very thin region of longitudinal thickness Δl, we can infer from { 19 } that:

$$\Delta l \approx \rho\theta \approx \rho \tan\theta \approx \rho \frac{\delta}{f} \qquad \{ 26 \}$$

$$\vec{B} = \kappa \begin{pmatrix} y \\ x \end{pmatrix} = \kappa \begin{pmatrix} 0 \\ \delta \end{pmatrix} = \kappa\delta\hat{y} \qquad \{ 27 \}$$

$$f = \delta \cot\theta = \delta \frac{\rho}{\Delta l} = \delta \frac{mv}{qB\Delta l} = \frac{mv}{\kappa q \Delta l} \qquad \{ 28 \}$$

Here, θ is the total turning angle as the particle traverses a circular arc due to the orthogonally acting magnetic field. The independence of the "focal length" f on δ demonstrates the similarity in behaviour of a quadrupole and a convex lens. Regardless of the value of the transverse offset, paraxially incident particles are converged to a single point.

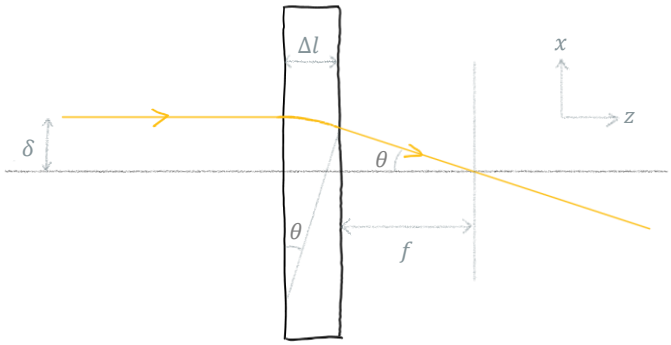

Figure 9: A figure depicting a quadrupole acting as a converging lens. A paraxial particle at any transverse distance δ from the principal (beam) axis crosses over at the same point marked by the focal length f due to the linear dependence of the Lorentz acceleration with transverse offset.

However, the differing signs of the accelerations in the two transverse axes in { 24 } and { 25 } poses the practical problem that focussing is achieved only on one axis, while the other axis diverges the particles (depending on the sign of κ). In other words, the quadrupole acts as a convex lens along the focussing axis, and as a concave lens along the defocussing axis. This means that particles that lie along the other axis will eventually be lost by hitting the walls of the synchrotron. To counteract this problem, a second defocussing quadrupole is placed at a short distance from the first focussing one. Just like how two lenses (one concave and one convex) of different focal lengths can be placed at a certain distance from each other to gain a net focussing effect, a similar approach can be adopted to obtain a net focussing effect along both axes. Such a pair of quadrupoles is termed a "unit-cell" or a FODO cell.

Finally, to always keep particles close to the design path, a single FODO cell may not be enough since particles tend to diverge after the focal point. Thus, a ring is essentially a collection of FODO cells placed at regular intervals to optimize particle confinement.

2.1.3 The Sextupole Magnet

Another type of magnet that can be used to correct for beam defects is a Sextupole magnet (or simply, sextupole). While quadrupoles are used to correct the divergent effects due to errors in particle positions, sextupoles are used to correct the chromaticity effects caused by the quadrupole magnets.

Chromaticity in particle accelerators is the phenomenon where a longitudinally travelling group of particles, each with its own small position offset, end up bending with a different radius of curvature in response to a transverse magnetic field due to them having different momentum offsets. Chromaticity effects, analogous to chromatic aberration in lenses, are seen at the ends of quadrupole magnets, which due to the combination of spatial separation and differing momenta of the particles, cannot be reliably corrected using quadrupole magnets.

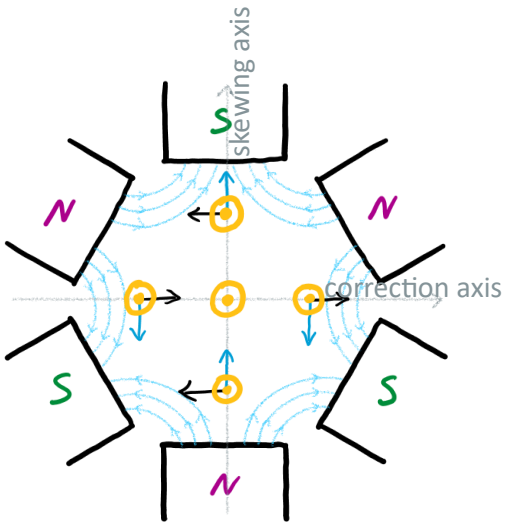

Figure 10: Configuration of a sextupole magnet for dispersion error corrections along the horizontal (xz) plane. The forces experienced by particles at different locations on the transverse plane (yellow circles) due to the apparent fields (blue arrows) are denoted by the black arrows.

As the name suggests, a sextupole magnet has six magnetic poles arranged in an alternating fashion around the beam. A sextupole meant to correct chromaticity on the horizontal plane typically has a north pole pointed along the vertical axis as shown in Figure 10. The defining design feature of a sextupole is that the apparent magnetic field varies with the second order of distance from the beam axis. More specifically, the transverse magnetic field felt by a longitudinally propagating particle impinging on the sextupole at transverse coordinates $\vec{r} = \begin{pmatrix} x \\ y \end{pmatrix}$ is given by:

$$\vec{B} = \chi\left(-xy\hat{x} - \frac{1}{2}(x^2 - y^2)\hat{y}\right) = \chi\begin{pmatrix} -xy \\ -\frac{1}{2}(x^2 - y^2) \end{pmatrix} \quad \{ 29 \}$$

Here, χ is the sextupole field strength, measured in T/m^2. Given this specific field function, the Lorentz acceleration is now given by:

$$\frac{d^2\vec{r}}{dt^2} = \frac{q}{m}\vec{v}\times\vec{B} = \chi\frac{q}{m}\begin{pmatrix}0\\0\\v\end{pmatrix}\times\begin{pmatrix}xy\\\frac{1}{2}(x^2-y^2)\\0\end{pmatrix} = \chi\frac{qv}{m}\begin{pmatrix}\frac{1}{2}(x^2-y^2)\\xy\\0\end{pmatrix} \quad \{30\}$$

The acceleration, which is now a function of the square of the transverse distance of the particle from the beam, is effectively used to correct the effects of chromaticity. The exact mechanism behind this correction is demonstrated in section 2.3.

2.2 Frenet-Serret Coordinate System

Before moving further towards the beam and spin dynamics of single particles in a storage ring, the coordinate system under which the terms are defined must be considered.

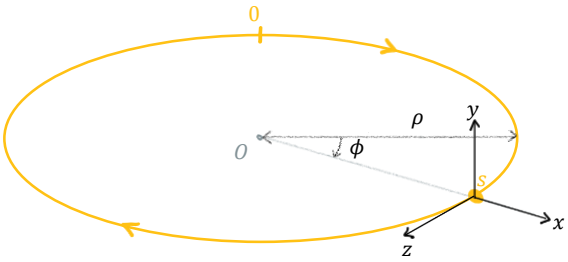

Figure 11: A drawing representing the right-handed Frenet-Serret coordinate system used to define the measurables of beam and spin dynamics in this thesis. The values marked in yellow are those of the location parameter s.

Consider that a particle traverses a fixed closed path, in a clockwise fashion. This path, called the "reference path", is typically circular but can essentially be any shape as long as it is closed. However, for the purposes of this study, the consideration is limited to paths lying on a single plane, called the "ring plane", and that the path is continuous and differentiable. Since the path is fixed, any given location on this path is simply specified by a single parameter s, which varies from 0 to L, which is the total length of the path. The "reference particle" is defined to be the particle that travels precisely on the reference path, at a fixed velocity, known as the "reference velocity".

In this paradigm, the origin is defined to be the location of the reference particle at any given moment. In other words, the coordinate system is basically designed to be the rest frame of the reference particle (the "Frenet" frame), located at s. With the origin defined, the z axis is defined to be along the tangent to the reference path at s, pointing towards its direction of motion. The y axis is perpendicular to the ring plane and pointing vertically upward. Finally, the x axis would lie along the ring plane in a direction perpendicular to the path such that it agrees with the cartesian convention ($\hat{x}\times\hat{y}=\hat{z}$). These axes are represented in Figure 11.

Based on these axes, the xy plane is generally referred to as the "transverse" plane, the yz plane as the "vertical" plane and the zx plane as the "ring" plane.

Such a coordinate system is referred to as a "curvilinear" or a "Frenet-Serret" coordinate system, named after the French mathematicians who devised the formulas describing the kinematic properties of particles moving along differentiable curves. More specifically, the coordinate system described above is a "left-handed" [30] Frenet-Serret system since the origin (particle) moves clockwise in accordance with the left-hand thumb rule. The equations of motion in this coordinate system are thus given by the Frenet-Serret formulae [31]:

$$\frac{d\hat{x}}{ds} = \frac{1}{\rho(s)}\hat{z}; \quad \frac{d\hat{y}}{ds} = 0; \quad \frac{d\hat{z}}{ds} = -\frac{1}{\rho(s)}\hat{x} \qquad \{ 31 \}$$

Here, $\rho(s)$ is the instantaneous radius of curvature at s. This system can be condensed to:

$$\frac{d\boldsymbol{Q}}{ds} = -\frac{1}{\rho(s)}\left(R_y{}^{\perp}\right)\boldsymbol{Q} \qquad \{ 32 \}$$

Here, $R_y{}^{\perp}$ is a 90° rotation matrix around the y-axis, and $\boldsymbol{Q}$ is the 3×3 matrix whose columns are the unit vectors $\hat{x}$, $\hat{y}$ and $\hat{z}$. To demonstrate the nature of each unit vector's variation, further differentiation with respect to s can be done to reduce the rotation matrix to an identity through the relation $\left(R_y{}^{\perp}\right)^2 = -I$. This gives us the new relations:

$$\frac{d^2\hat{x}}{ds^2} = -\frac{1}{\rho^2}\hat{x}; \quad \frac{d^2\hat{y}}{ds^2} = 0; \quad \frac{d^2\hat{z}}{ds^2} = -\frac{1}{\rho^2}\hat{z} \qquad \{ 33 \}$$

These equations represent the general case of a 2D harmonic oscillator on the ring plane. By applying the appropriate boundary condition of phase orthogonality to the solutions, the specific case of circular motion as described above, is obtained.

2.3 Transverse Beam Dynamics in storage rings

2.3.1 Betatron Motion

In a storage ring with a predefined reference path and velocity, with quadrupoles (but no sextupoles for the time being) for beam corrections, let u be a transverse coordinate (either x or y in the Frenet frame) of a particle. As the particle traverses the storage ring, the value of this coordinate varies depending on its initial value, and the specific locations of the quadrupoles (specified by the curvilinear

coordinate s), which apply the focussing or defocussing accelerations. In general, the variation of u can be summarised with this differential equation [30]:

$$\frac{d^2u(s)}{ds^2} + k(s)u(s) = 0 \qquad \{ 34 \}$$

This equation is known as the Hill's Differential Equation (HDE). Here, u and k both depend on s. With this factor implied, the above equation is simply written as:

$$u'' + ku = 0 \qquad \{ 35 \}$$

The apostrophes now represent derivatives with respect to s. From the formalisms derived for the quadrupole magnets in section 2.1.2, k for each coordinate becomes:

$$\begin{aligned} k_x &= \frac{1}{\rho(s)^2} + K(s) \\ k_y &= -K(s) \end{aligned} \qquad \{ 36 \}$$

Here, $K(s)$ is the "focussing function" that is proportional to the quadrupole field strength at the location s. $\rho(s)$ is the radius of curvature, which is constant for a perfectly circular ring, but has an s-dependence for non-circular rings. It is now clear that { 35 } cannot simply be solved with the expression for a harmonic oscillator due to the s-dependence of k.

With no additional constraints, solutions to the HDE are possible. However, a relatively simple approach is taken by applying the Floquet theorem [30], which states that for a periodic function k_u, such that:

$$k(s) = k(s + l') \qquad \{ 37 \}$$

…for a constant l', the HDE can be solved using the solution:

$$u = \sqrt{\epsilon}\sqrt{\beta(s)}\cos(\psi(s) + \phi) \qquad \{ 38 \}$$

…where ϕ is an arbitrary phase offset, ϵ is a constant known as the emittance, and $\beta(s)$ and $\psi(s)$ are known as the betatron amplitude function (or simply, beta function) and phase function respectively. l' is typically equal to L, the circumference of the synchrotron. However, if the devices are configured on the ring so that the ring has a "P-fold" symmetry, then l' is given by:

$$l' = \frac{L}{P} \qquad \{ 39 \}$$

Here, P is a natural number denoting the number of symmetry axes, known as the "superperiodicity" of the synchrotron.

When we substitute the solution { 38 } into { 35 } and enforce its validity at all values of s, we obtain the relations:

$$\psi' = \frac{1}{\beta} \quad \Rightarrow \quad \psi(s) = \int_0^s \frac{1}{\beta(s_1)} ds_1 \qquad \{ 40 \}$$

$$2\beta\beta'' - \beta' + 4k\beta^2 - 4 = 0 \qquad \{ 41 \}$$

For a synchrotron with a known k distribution (determined by the positions and field strengths of the quadrupoles), the beta and phase functions can now be obtained from the above expressions. Since { 41 } must remain true at all values of s, it is necessary that the beta function also possesses a matching periodicity to k, i.e.

$$\beta(s) = \beta(s + l') \qquad \{ 42 \}$$

Thus, with the beta function, determined solely from the structure of the synchrotron, guiding its amplitude and phase advance, the particle moves about the reference position according to { 38 }. This motion is called betatron motion.

Furthermore, betatron motion is a "pseudo-harmonic" motion in the sense that it is not periodic with s. However, if we define the "betatron tune" (Q):

$$Q = \frac{1}{2\pi}\psi(L) = \frac{1}{2\pi}\int_0^L \frac{1}{\beta(s)} ds \qquad \{ 43 \}$$

…which is the total phase advance at the end of one turn, then the motion according to the "pseudo-displacement" ($\eta = \frac{u}{\sqrt{\beta}}$) and "pseudo-time" ($\varrho = 2\pi\frac{\psi}{Q}$) is simple harmonic:

$$\frac{d^2\eta}{d\varrho^2} + Q^2\eta = 0 \qquad \{ 44 \}$$

The frequency term in this characteristic harmonic motion, also known as "linear" betatron motion, is in fact the betatron tune Q. This quantity is often used to

characterise the beam in a storage ring. The pair of betatron tunes (Q_x and Q_y) in each transverse dimension is together called a "working point".

Finally, from { 38 } and its derivative:

$$u' = \frac{1}{2}\beta' \sqrt{\frac{\epsilon}{\beta}}\cos(\psi(s) + \phi) - \sqrt{\frac{\epsilon}{\beta}}\sin(\psi(s) + \phi) \qquad \{ 45 \}$$

…the identity $\sin^2\vartheta + \cos^2\vartheta = 1$ allows for the elimination of the sine and cosine terms to give the expression for the Courant-Snyder Invariant [30]:

$$\epsilon = \gamma x^2 + 2\alpha x x' + \beta x'^2 \qquad \{ 46 \}$$

Where…

$$\alpha = -\frac{\beta'}{2}; \quad \gamma = \frac{1+\alpha^2}{\beta} \qquad \{ 47 \}$$

The equation { 46 } represents an ellipse in phase-space, whose tilt and eccentricity are determined by the Courant-Snyder parameters α, β and γ. The area of the ellipse is given by $\pi\epsilon$, where the emittance ϵ is also known as the Courant-Snyder invariant, which is typically used to characterise the cross-sectional "size" of the beam in each transverse direction. A typical phase-space ellipse is shown in Figure 12.

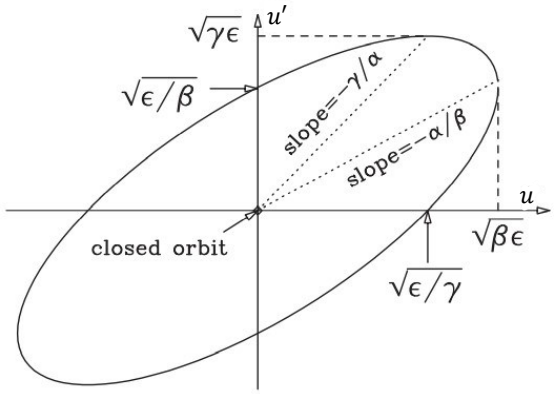

Figure 12: The Courant-Snyder ellipse drawn by a particle with emittance ϵ. The origin of the plot represents the reference particle ($\epsilon = 0$). Also marked are the maximum amplitude ($\sqrt{\beta\epsilon}$) and velocity ($\sqrt{\gamma\epsilon}$) attained during the betatron motion.

2.3.1.1 Transverse phase space: Transfer Matrix Formalism

While the equations describing the particle motion in terms of single coordinates are useful, a more optimized way to deal with different devices on the beamline, each modifying particle trajectories in their own way is through a matrix formalism.

To do this, a "state" vector must be chosen on which the various matrices, each representing a device, or even the entire ring, can operate on to "propagate" them.

Considering that the differential equation describing the general particle motion is of the second order, we devise a two-component state vector $\vec{\mu}$, with position and velocity along a transverse coordinate (x or y) as its components, which is assumed to contain all the information about a particle's state.

$$\vec{\boldsymbol{u}} = \begin{pmatrix} u \\ u' \end{pmatrix} \quad \{ 48 \}$$

To describe the formalism, it is useful to write the Floquet solutions as:

$$u = \sqrt{\epsilon\beta}\cos\phi\cos\psi - \sqrt{\epsilon\beta}\sin\phi\sin\psi \quad \{ 49 \}$$

$$u' = -\sqrt{\frac{\epsilon}{\beta}}[\cos\phi\,(\alpha\cos\psi + \sin\psi) + \sin\phi\,(-\alpha\sin\psi + \cos\psi)] \quad \{ 50 \}$$

With this, the state vector can now be formalised as:

$$\vec{\boldsymbol{u}} = -\sqrt{\frac{\epsilon}{\beta}}\begin{pmatrix} \beta & 0 \\ -\alpha & -1 \end{pmatrix}\begin{pmatrix} \cos\psi & -\sin\psi \\ \sin\psi & \cos\psi \end{pmatrix}\begin{pmatrix} \cos\phi \\ \sin\phi \end{pmatrix} \quad \{ 51 \}$$

To get the initial state vector, we set $\psi = 0$, $\beta = \beta_0$ and $\alpha = \alpha_0$:

$$\vec{\boldsymbol{u}}_0 = \begin{pmatrix} u_0 \\ u_0' \end{pmatrix} = -\sqrt{\frac{\epsilon}{\beta_0}}\begin{pmatrix} \beta_0 & 0 \\ -\alpha_0 & -1 \end{pmatrix}\begin{pmatrix} \cos\phi \\ \sin\phi \end{pmatrix} \quad \{ 52 \}$$

From this the transfer matrix $\boldsymbol{U}_{s/0}$ from $\vec{\boldsymbol{u}}_0$ to $\vec{\boldsymbol{u}}$ can be obtained:

$$\vec{\boldsymbol{u}} = \boldsymbol{U}_{s/0}\vec{\boldsymbol{u}}_0 = \sqrt{\frac{\beta_0}{\beta}}\begin{pmatrix} \beta & 0 \\ -\alpha & -1 \end{pmatrix}\begin{pmatrix} \cos\psi & -\sin\psi \\ \sin\psi & \cos\psi \end{pmatrix}\begin{pmatrix} \beta_0 & 0 \\ -\alpha_0 & -1 \end{pmatrix}^{-1}\vec{\boldsymbol{u}}_0 \quad \{ 53 \}$$

Here, $\boldsymbol{U}_{s/0}$ can either be $\boldsymbol{X}_{s/0}$ or $\boldsymbol{Y}_{s/0}$ for the horizontal and vertical phase spaces. Defining $\boldsymbol{B}(s) = \frac{1}{\sqrt{\beta}}\begin{pmatrix} \beta & 0 \\ -\alpha & -1 \end{pmatrix}$ and $\boldsymbol{B}(0) = \frac{1}{\sqrt{\beta_0}}\begin{pmatrix} \beta_0 & 0 \\ -\alpha_0 & -1 \end{pmatrix}$ results in the shorthand:

$$\boldsymbol{U}_{s/0} = \boldsymbol{B}(s)R(\psi)\boldsymbol{B}(0)^{-1} \quad \{ 54 \}$$

Thus, the transfer matrix in the Floquet basis can be seen as a coordinate rotation via R after the normalization of the phase space coordinates with $\boldsymbol{B}$. This can be further visualized in Figure 13.

Using the convenient rotation matrix framework, a general expression for the transfer matrix of a ring segment from $s = s_1$ to $s = s_2$ can also be formulated:

$$\boldsymbol{U}_{s_2/s_1} = \boldsymbol{B}(s_2)\boldsymbol{R}(\psi_2 - \psi_1)\boldsymbol{B}(s_1)^{-1} \quad \{55\}$$

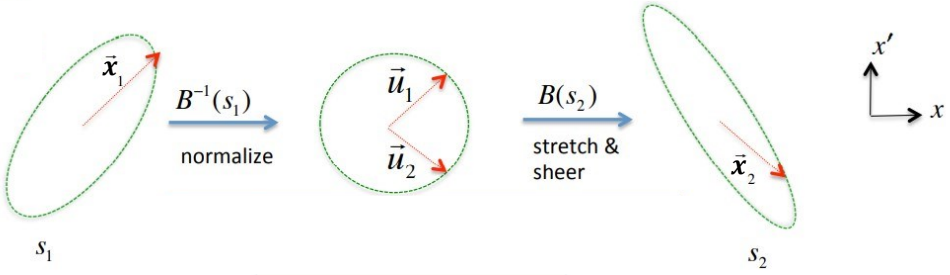

Figure 13: A visualization of the transformations to the phase space ellipse during the process of transport from $s = s_1$ to $s = s_2$.

Finally, we can calculate the transfer matrix of one superperiod $\boldsymbol{M}_{s\to s+l'}$. In this case, due to the intrinsic periodicity of the Courant-Snyder parameters, $\boldsymbol{B}(s + l') = \boldsymbol{B}(s)$, and the matrix can be parametrised as:

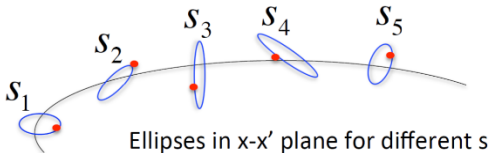

Figure 14: An illustration of the variation of the phase space ellipse during transport.

$$\boldsymbol{U}_{s+l'/s} = \boldsymbol{I}\cos\left(2\pi\frac{Q}{P}\right) + \boldsymbol{J}\sin\left(2\pi\frac{Q}{P}\right) \quad \{56\}$$

…where $\boldsymbol{I}$ is the identity matrix and $\boldsymbol{J} = \begin{pmatrix} \alpha & \beta \\ -\gamma & -\alpha \end{pmatrix}$. This is the Courant-Snyder parametrization of the one-period matrix. This parametrization makes clear some interesting properties of the matrix:

$$\left|\boldsymbol{U}_{s+l'/s}\right| = 1 \quad \{57\}$$

$$\boldsymbol{J}^2 = -\boldsymbol{I} \quad \{58\}$$

$$\left(\boldsymbol{U}_{s+l'/s}\right)^n = \boldsymbol{I}\cos\left(2\pi n\frac{Q}{P}\right) + \boldsymbol{J}\sin\left(2\pi n\frac{Q}{P}\right) \quad \{59\}$$

$$\left(\boldsymbol{U}_{s+l'/s}\right)^{-1} = \boldsymbol{I}\cos\left(2\pi\frac{Q}{P}\right) - \boldsymbol{J}\sin\left(2\pi\frac{Q}{P}\right) \quad \{60\}$$

2.3.1.2 Beam stability

The stability condition of the beam is a condition that the one-period matrix, or the one-turn matrix must satisfy for the beam to be stable. This condition is as follows:

$$\left|tr\left(\boldsymbol{U}_{s+L/s}\right)\right| \leq 2 \qquad \{ 61 \}$$

In other words, the condition enforces that the phase advance $2\pi\frac{Q}{P}$, and by extension, the betatron tune Q be a real number. An imaginary Q is possible if the ring or symmetric cell has a net defocussing effect instead of a focussing one. This would typically result in a beam that (at least along one transverse axis) diverges and is eventually lost.

2.3.1.3 Betatron Resonance

A resonance in betatron motion is a phenomenon where the beam parameters are configured in a way that slight device or field imperfections apply resonant kicks to the particle to eventually push it out of the ring. The condition for resonance is:

$$mQ_x + nQ_y = j \qquad \{ 62 \}$$

Here, m, n and j are integers. The order of the resonance is determined by $|m + n|$. The first order resonance has the form $Q = j$, i.e., the betatron tune along a transverse direction is an integer. This leads to the situation where the one-turn matrix reduces to the identity:

$$\boldsymbol{U}_{s+L/s} = \boldsymbol{I} \qquad \{ 63 \}$$

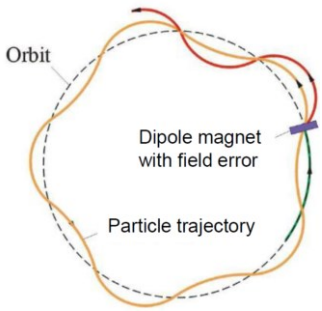

Figure 15: An example of error amplification due to betatron resonance at $Q_x = 5$. [81]

Therefore, the presence of a small defocussing defect (imaginary phase advance) by, for example, a field error in a dipole magnet, at any location s on the ring would change the one-turn matrix to:

$$\boldsymbol{U}_{s+L/s}{}^{*} = \boldsymbol{U}_{s+L/s}\begin{pmatrix} 1+\delta_d & 0 \\ 0 & 1+\delta_d \end{pmatrix} = \begin{pmatrix} 1+\delta_d & 0 \\ 0 & 1+\delta_d \end{pmatrix} \qquad \{ 64 \}$$

The trace of this system would thus become $2 + 2\delta_d$, which is greater than 2. Even for a tiny defect δ_d, this defocussing effect would magnify exponentially over several turns, resulting in the loss of the particle (see Figure 15).

$$tr\left(\begin{pmatrix} 1+\delta_d & 0 \\ 0 & 1+\delta_d \end{pmatrix}^n\right) = 2(1+\delta_d)^n \qquad \{ 65 \}$$

Thus, resonant configurations are to be avoided in closed beamline operations.

2.3.2 Off-Momentum Particles and Dispersion

So far in calculations of betatron motion, particles with position offsets from the reference particle have been considered, while essentially maintaining that they travel at exactly the design momentum. This is, however, not always the case, as was explored in section 2.1.3.

Considering a focussing quadrupole that obeys the HDE, the value of k at the location of the quadrupole can be determined from a comparison of { 35 } and { 24 } (recall that $ds = vdt$):

$$k = \kappa \frac{q}{mv} = \kappa \frac{q}{p} \qquad \{ 66 \}$$

If the particle has a small momentum offset given by $\delta = \frac{\Delta p}{p}$, the value of k would change to k_1 (approximated by considering only the first order term):

$$k_1 = \kappa \frac{q}{p + \delta p} = \kappa \frac{q}{p}(1 - \delta + \delta^2 - \cdots) \approx k(1 - \delta) \qquad \{ 67 \}$$

This results in the inhomogeneous form of the HDE:

$$u'' + ku = k\delta u \qquad \{ 68 \}$$

The solution to such an equation would take the form:

$$u = \sqrt{\epsilon}\sqrt{\beta(s)}\cos(\psi(s) + \phi) - \delta D(s) \qquad \{ 69 \}$$

Here, $D(s)$ is called the dispersion function, which is an indicator of the magnitude of dispersion effects as a function of s. The dispersion function can be calculated using the Green's function method [29]:

$$D(s) = \delta \int_0^s k(\tilde{s})G(s, \tilde{s})\, d\tilde{s} \qquad \{ 70 \}$$

The function $G(s, \tilde{s})$ is known as Green's function which is essentially defined as the solution to the marginally perturbed homogeneous equation:

$$G'' + k(s)G = \mathfrak{d}(s - \tilde{s}) \qquad \{ 71 \}$$

…with $\mathfrak{d}(s - \tilde{s})$ being the Dirac-delta function with its spike at $\tilde{s}$. The Courant-Snyder parameters together with the dispersion functions at each transverse axis are together called the "Twiss" parameters. The Twiss parameters collectively hold all

the necessary information to exactly determine the time development of a particle's motion around the ring.

2.3.3 Chromaticity

Chromaticity is the term given to the change in the effective betatron tune on a particle with a slight offset in momentum. It is denoted (in each transverse direction) by:

$$\xi = \frac{\Delta Q}{\delta} \qquad \{ 72 \}$$

To measure the chromaticity effect of a quadrupole [32], an infinitesimally thin quadrupole is assumed to be placed on a synchrotron ring at a location s. A particle with a momentum offset δ, after exiting the quadrupole slice would have an additional term in its velocity.

$$du' = u''ds = -kuds + ku\delta ds \qquad \{ 73 \}$$

$$\begin{pmatrix} u_2 \\ u_2' \end{pmatrix} \rightarrow \begin{pmatrix} u_2 \\ u_2' + ku\delta ds \end{pmatrix} \qquad \{ 74 \}$$

The transfer matrix $\boldsymbol{U}_{s+L/s}{}^{*}$ of the ring (one-turn matrix, measured from s) would now differ from the one without the added slice $\boldsymbol{U}_{s+L/s}$ by a phase error of $d\psi$ in its coordinate rotation. But this would now be equivalent to:

$$\boldsymbol{U}_{s+L/s}{}^{*} = \begin{pmatrix} 1 & 0 \\ k\delta ds & 1 \end{pmatrix} \boldsymbol{U}_{s+L/s} \qquad \{ 75 \}$$

Equating the traces of the resultant matrices on both sides gives us the expression:

$$\cos\left(2\pi\frac{Q}{P} + d\psi\right) = \cos\left(2\pi\frac{Q}{P}\right) + \frac{1}{2}\beta k\delta \sin\left(2\pi\frac{Q}{P}\right) ds \qquad \{ 76 \}$$

Upon evaluation of $d\psi$ in terms of dQ using { 43 } and further simplification, the expression for ΔQ and thus, ξ is obtained:

$$\Delta Q = -\frac{P\delta}{4\pi}\int_{s_1}^{s_2} \beta k \, ds \qquad \{ 77 \}$$

$$\xi_0 = -\frac{1}{4\pi}\int_0^L \beta k\, ds \qquad \{ 78 \}$$

The above equation talks about the chromaticity contributed by the quadrupoles in the ring and is termed the "natural" chromaticity of the ring. It also shows that lattices with a strong focussing tend to have negative natural chromaticities due to higher momentum particles being bent less by the quadrupole, thus ending up oscillating with a lower tune.

2.3.4 Chromaticity correction by sextupoles

Dispersion and chromaticity effects, which arise due to off-momentum particles are described by the dispersion function $D(s)$ at the local level, and by the chromaticity ξ at the global level. Here, the method of chromaticity correction using sextupoles is explored.

Like in the previous example, a periodic FODO cell is considered, within which an infinitesimal sextupole segment of length ds exposed to a non-zero dispersion function. From the expression { 30 } of the Lorentz acceleration due to the sextupole, we get the equation of motion along the horizontal axis:

$$x'' - \frac{\tilde{\chi}}{2}(x^2 - y^2) = 0 \qquad \{ 79 \}$$

…where $\tilde{\chi} = \chi\frac{q}{p}$ is the normalized sextupole field strength. From { 69 }, it can be seen that due to the dispersion function, the particle displacement now changes:

$$x^* = x - D\delta \qquad \{ 80 \}$$

Combining this with { 79 } results in the expression for the change in velocity due to the sextupole slice, and an additional term in the final state vector:

$$dx' = x''ds = -\tilde{\chi}xD\delta + \frac{\tilde{\chi}}{2}(D\delta)^2 + \frac{\tilde{\chi}}{2}(x^2 - y^2) \approx -\tilde{\chi}xD\delta + \frac{\tilde{\chi}}{2}(x^2 - y^2) \qquad \{ 81 \}$$

$$\begin{pmatrix} x_2 \\ x_2' \end{pmatrix} \rightarrow \begin{pmatrix} x_2 \\ x_2' - \tilde{\chi}xD\delta ds \end{pmatrix} \qquad \{ 82 \}$$

Thus, from the similarity with the example in 2.3.3, it can be seen that the effect of the sextupole slice s equivalent to a kick from a quadrupole of gradient $-\tilde{\chi}D\delta$. This, analogous to { 77 }, gives a tune shift and a chromaticity correction [32]:

$$\Delta Q = \frac{P\delta}{4\pi}\int_{s_1}^{s_2} \tilde{\chi}\beta D\, ds \qquad \{ 83 \}$$

$$\xi_\chi = \frac{1}{4\pi}\int_0^L \tilde{\chi}\beta D\, ds \qquad \{ 84 \}$$

This chromaticity contribution is termed as a correction due to its positive sign as compared to the one due to the quadrupole. The effective chromaticity ξ of the ring would now be given by:

$$\xi = \xi_\chi - \xi_0 \qquad \{ 85 \}$$

Since the correcting effect of sextupoles scale with the dispersion function, sextupoles are generally placed at locations with high dispersion. Quadrupoles and sextupoles may also be placed adjacent to each other to function effectively.

2.4 Longitudinal Beam Dynamics in Storage rings

So far, the mechanisms that govern transverse offsets in the presence of focussing devices such as quadrupoles and sextupoles have been discussed. In the longitudinal domain, the mechanisms are quite different and often decoupled from transverse beam dynamics.

A storage ring only requires a small number of bunches and does not require acceleration. Thus, in the following subsections, the mechanisms governing longitudinal beam dynamics will be discussed in the presence of a single RF cavity.

2.4.1 Path Lengthening and momentum compaction

Path lengthening is the effect of change in the length of the path when a particle has a momentum offset. This effect is primarily due to faster particles being bent at a larger radius. To see how this occurs, the situation in Figure 16 is considered, in a storage ring in the absence of RF bunching.

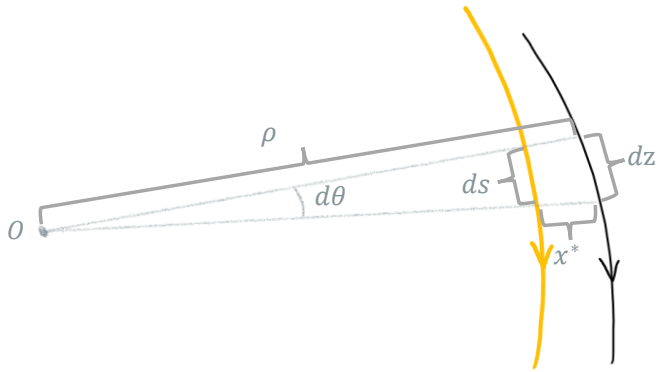

Figure 16: A diagram depicting the motion of an off-momentum particle in the absence of focussing. The motion of the offset particle (black curve) through an element $d\theta$ of the "ring angle", can be represented as a function of that of the reference particle (yellow curve).

An otherwise reference particle with a momentum offset $\delta = {}^{\Delta p}/_{p}$ is assumed to travel a path which is offset by $x^*(s)$ in the radial direction at each location s on the reference path. The total path length L^* traversed by this particle is given by:

$$L^* = \int_0^{L^*} dz = \int_0^{L} \left(1 - \frac{x^*}{\rho}\right) ds \qquad \{ 86 \}$$

Since a reference particle is considered, from { 80 }, we have $x^* = -D\delta$. The change in path length can now be calculated:

$$\frac{\Delta L}{L} = \frac{L^* - L}{L} = \frac{\delta}{L} \int_0^{L} \frac{D}{\rho} ds \qquad \{ 87 \}$$

The momentum compaction factor α_c is now defined as:

$$\alpha_c = \frac{{}^{\Delta L}/_{L}}{\delta} = \frac{1}{L} \int_0^{L} \frac{D}{\rho} ds \qquad \{ 88 \}$$

This quantity gives information about the rate of change of path length with momentum of a particle. Along with the path length, the travel time t of the particle around the ring also changes with momentum offset. The travel time is given by:

$$t = \frac{L}{v} \qquad \{ 89 \}$$

Using logarithmic differentiation, the time offset is obtained:

$$\frac{\Delta t}{t} = \frac{\Delta L}{L} - \frac{\Delta v}{v} \qquad \{ 90 \}$$

Using the relations $p = \gamma m v$ and { 88 }, the path and velocity offsets can be related to the momentum offset as:

$$\frac{\Delta t}{t} = -\left(\frac{1}{\gamma^2} - \alpha_c\right) \delta = -\eta_c \delta \qquad \{ 91 \}$$

Here, η_c is called the phase slip factor, which gives information about the rate of change of the travel time of a particle with momentum.

It is interesting to note that for a classical (slow moving) particle, the travel time remains constant with change in momentum, given the nature of the radius of

curvature { 19 }. This makes $\eta_c = 0$ and $\alpha_c = 1$. The phenomenon of phase slip can thus be seen as exclusive of relativistic particles.

Furthermore, under relativistic conditions, it is possible for a particle to have an energy such that the phase slip vanishes. This energy is called the transition energy E_T, and the Lorentz factor at this point is called the transition-γ or γ_T where:

$$\frac{1}{\gamma^2} = \alpha_c \quad \Rightarrow \quad E_T = \frac{mc^2}{\sqrt{\alpha_c}} = \gamma_T mc^2 \qquad \{ 92 \}$$

Beyond the transition energy, travel times tend to increase with momentum, due to a larger component of the energy increase going to the particle's mass rather than its velocity.

2.4.1.1 Higher order momentum compaction

At larger momentum offsets, the change in path length as a function of momentum offset may not be strictly linear. This is because for a larger δ, additional terms in the expression of the focussing function must be considered (see { 67 }) Therefore, the dispersion function that solves the HDE under these circumstances would now have additional dependencies on each order of δ. These can be calculated from the Taylor expansion of the HDE solution u^*:

$$u^* = u + \frac{du}{d\delta}\delta + \frac{1}{2!}\frac{d^2u}{d\delta^2}\delta^2 + \frac{1}{3!}\frac{d^3u}{d\delta^3}\delta^3 + \cdots = u + D_0\delta + D_1\delta^2 + D_2\delta^3 + \cdots \qquad \{ 93 \}$$

$$D^* = D_0 + D_1\delta + D_2\delta^2 + D_3\delta^3 + \cdots \qquad \{ 94 \}$$

Here, D^* is the modified dispersion function for large offsets and D_n is the n^{th}-order dispersion function. Since the change in path length depends on the dispersion function, it can now be expanded as follows:

$$\frac{\Delta L^*}{L} = \alpha_0\delta + \alpha_1\delta^2 + \alpha_2\delta^3 + \cdots \qquad \{ 95 \}$$

$$\Rightarrow {\alpha_c}^* = \alpha_0 + \alpha_1\delta + \alpha_2\delta^2 + \cdots \qquad \{ 96 \}$$

This expansion allows the capture of more realistic behaviour of path lengthening in the synchrotron. Here, α_0 is called the first-order momentum compaction factor, α_1 is called the second-order momentum compaction factor, and so on. Specifically, the n^{th}-order momentum compaction factor is given by:

$$\alpha_n = \frac{1}{L}\int_0^L \frac{D_n}{\rho} ds \qquad \{ 97 \}$$

2.4.2 Synchrotron frequency

The RF cavity demonstrated in section 2.1.1 is in fact, a device with multiple cavities. Such a device is useful for accelerating multiple bunches at a time, since every alternate cavity can accelerate its own bunch and the cavity spacing determines the bunch frequency of the beam. However, for the storage ring application, since particles are not to be used up for the experiment (such as fixed target or colliding beam experiments), additional bunches would only be required for control purposes [8]. Thus, in this thesis, a "pillbox" cavity is considered as shown in Figure 17.

An example of a single pillbox cavity centred at $s = 0$ on a storage ring is considered. The cavity runs an RF electric field according to [30]:

$$\mathcal{E}_{RF} = \mathcal{E}_0 \sin(\omega_c t) \qquad \{ 98 \}$$

Considering that a storage ring does not need a net acceleration of particles, it is now assumed that the reference particle is synchronised with the trough of the RF potential. In other words, the reference particle is at $s = 0$ at $t = 0$, and revolves around the ring at its constant design momentum p_0 and angular frequency ω_0 as it receives no additional energy per turn. The frequencies of the RF cavity and the particle are related by the harmonic number h:

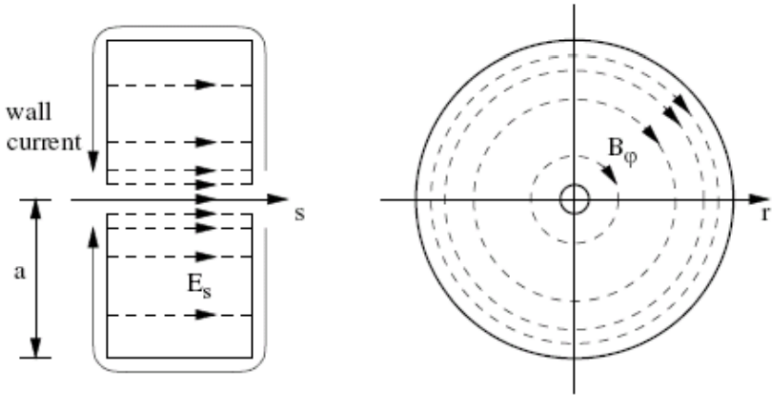

Figure 17: A cylindrical pillbox cavity. The left image shows a lateral cut-section, where the direction and distribution of the electric field, as well as wall current losses can be seen. The right image shows an axial view, where the induced magnetic field due to the varying electric field is depicted. [81]

$$\omega_c = h\omega_0 \qquad \{ 99 \}$$

This number essentially describes the maximum number of simultaneous bunches that the storage ring can hold.

Now, an offset particle is considered to be moving in the storage ring alongside the reference particle with a momentum p, a revolution frequency ω, and a resulting (time-varying) phase difference ϕ with respect to the RF field. Assuming for now that this phase difference is small, the energy gained by this particle in turn i as it passes through the RF cavity is given by:

$$E_i = q\int_{-d/2}^{d/2} \mathcal{E}_{RF}\, ds = qv\int_{-d/2v}^{d/2v} \sin(\omega_c t + \phi)\, dt = qV\sin\phi \qquad \{ 100 \}$$

Here, d is the width of the RF cavity, v is the velocity of the particle, and $V = \mathcal{E}_0 L\frac{\sin(\pi h d/L)}{\pi h}$ is the effective potential as seen by the particle. The effective potential is scaled by the width d of the cavity. For a thin cavity, the field seen would nearly be uniform during the particle's travel time through it, and $V = \mathcal{E}_0 d$. But narrow cavities have a low breakdown voltage, limiting the electric field strength. Now,

$$\frac{dE}{dt} = \frac{\omega_0}{2\pi}E_i = \frac{\omega_0}{2\pi}qV\sin\phi \approx \frac{\omega_0}{2\pi}qV\sin\phi \qquad \{ 101 \}$$

$$\frac{d\phi}{dt} = h(\omega - \omega_0) = 2\pi h\left(\frac{1}{t} - \frac{1}{t_0}\right) = -\frac{2\pi h}{t}\left(\frac{\Delta t}{t_0}\right) = h\omega\eta_c\delta = h\omega_0\eta_c\delta \qquad \{ 102 \}$$

$$\frac{d\delta}{dt} = \frac{d}{dt}\left(\frac{c^2}{{v_0}^2}\frac{\Delta E}{E_0}\right) = \frac{d}{dt}\left(\frac{c^2 E}{{v_0}^2 E_0} - \frac{c^2}{{v_0}^2}\right) = \frac{c^2}{{v_0}^2 E_0}\frac{dE}{dt} \qquad \{ 103 \}$$

Using the relations above, the equation for the synchrotron oscillations is obtained:

$$\frac{d^2\phi}{dt^2} = h\omega_0\eta_0\frac{c^2}{{v_0}^2 E_0}\frac{\omega_0}{2\pi}qV\sin\phi \approx \frac{qh{\omega_0}^2 c^2\eta_c V}{2\pi{v_0}^2 E_0}\phi = -{\omega_s}^2\phi \qquad \{ 104 \}$$

Thus, giving the expression for synchrotron frequency in a storage ring:

$$\omega_s = \omega_0\sqrt{-\frac{qhc^2 V\eta_c}{2\pi{v_0}^2 E_0}} \qquad \{ 105 \}$$

Synchrotron oscillations when the reference particles are not accelerating are known as stationary synchrotron oscillations. These oscillations give rise to ellipses in phase space. However, without the approximation for small angles in { 104 }, the solutions begin to draw out the phase space of a pendulum undergoing large oscillations. Thus, similar to a pendulum, a "separatrix" can be traced in phase space, beyond which particles follow open paths, analogous to an energetic

pendulum performing rotations. The full phase space can be visualized in Figure 18.

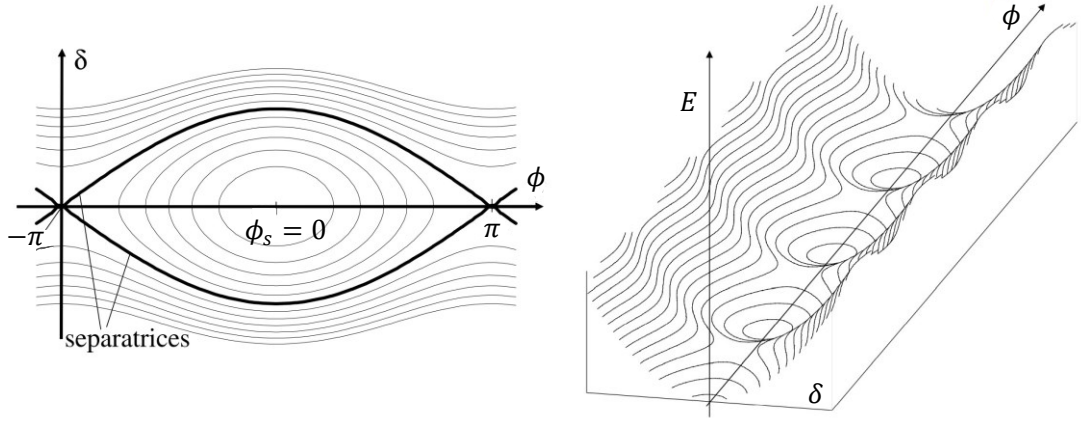

Figure 18: The phase space representation of "stationary" synchrotron oscillations. The contours in the graphs represent paths followed by particles at a certain energy. The left image shows the limits of the stable oscillations, known as separatrices. Particles with phase space parameters within the limits of the separatrices follow closed paths representing stable oscillations. Particles with phase space parameters beyond the separatrix limits follow open paths, and essentially get debunched. The right image shows the same phase space with an additional dimension of particle energy, where the RF "buckets" can be visualized. The energy of the bucket centers is the energy E_0 of the reference particle. [29]

In the case where the particles are being accelerated by the RF cavity, the reference particle would now also be at a phase difference ϕ_s from the potential troughs. However, in this setup, for the beam to be sustainable, the magnetic field must be adjusted in accordance with the increasing energy of the particles. So, the above quantities would then describe changes with respect to the synchronised reference particle, and the synchrotron frequency receives just one additional term:

$$\omega_s{}^* = \omega_0 \sqrt{-\frac{qhc^2 V \eta_c \cos\phi_s}{2\pi {v_0}^2 E_0}} \qquad \{ 106 \}$$

In acceleration mode, the reference particle receives energy at each turn, and the RF cavity and magnetic fields are synchronously adjusted so that the reference path remains fixed, and the reference particle enters the cavity at the same phase ϕ_s every turn. This is why ϕ_s is known as the "synchronous phase". The oscillations around this synchronized accelerating particle are called "moving" synchrotron oscillations. The phase space representation of moving synchrotron oscillations are shown in Figure 19.

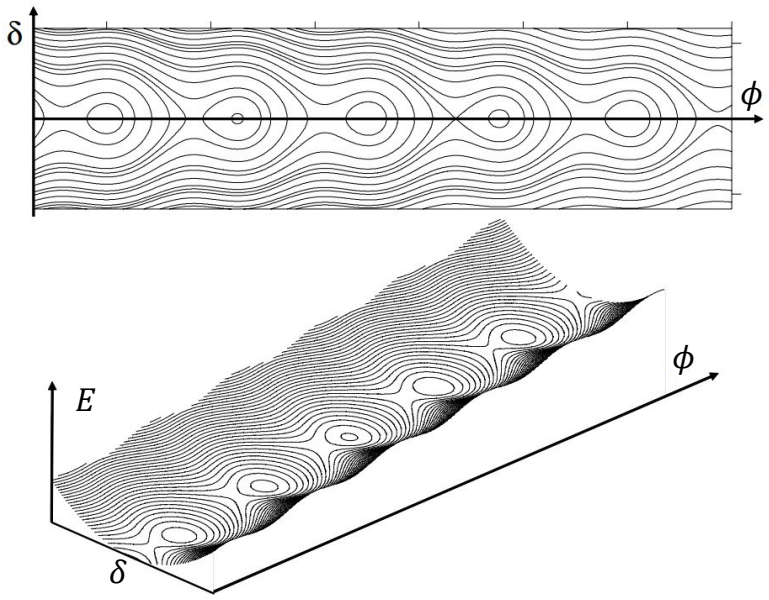

Figure 19: A phase space representation of "moving" synchrotron oscillations where $\phi_s > 0$. The top image shows the "spreading out" of the separatrices as the particle phase reduces. The bottom image shows the same with the energy coordinate, where it can be seen that each bunch is at a higher energy than the next as the bucket centres accelerate. It can also be noticed that as the synchronous phase increases, the phase space gets steeper, but the buckets get shallower. [29]

Finally, since the longitudinal displacement z in the Frenet frame is more useful in describing longitudinal phase space, the phase ϕ now translates to:

$$z = \frac{v_0}{\omega_c}\phi = \frac{v_0}{h\omega_0}\phi \qquad \{ 107 \}$$

2.4.2.1 Longitudinal phase space

With a description of longitudinal behaviour of particles, the transfer matrix formalism for the longitudinal phase space can be developed.

Considering that the equation of motion along the longitudinal axis is also of the second order, the state vector and its initial values can be defined as:

$$\vec{\boldsymbol{z}} = \begin{pmatrix} z \\ z' \end{pmatrix} \quad \vec{\boldsymbol{z}}_0 = \begin{pmatrix} z_0 \\ z_0' \end{pmatrix} \qquad \{ 108 \}$$

The equation { 104 } for a storage ring in stationary bunching mode can be solved using the solution to a harmonic oscillator with the approach similar to the one used in section 2.3.1.1:

$$\vec{\boldsymbol{z}} = \begin{pmatrix} 1 & 0 \\ 0 & \omega_s \end{pmatrix} \begin{pmatrix} \cos\psi & \sin\psi \\ -\sin\psi & \cos\psi \end{pmatrix} \vec{\boldsymbol{z}}_0 = \boldsymbol{Z}_{t/0}\vec{\boldsymbol{z}}_0 \qquad \{ 109 \}$$

Here, $\boldsymbol{Z}_{t/0}$ is the longitudinal transfer matrix from time $t = 0$ to $t = t$, ω_s is the synchrotron frequency, and $\psi = \omega_s t$.

2.4.2.2 Longitudinal beam stability

The stability criterion for longitudinal beam dynamics is satisfied when the synchrotron frequency is a real number. This can only occur in the following condition:

$$\eta_c \cos \phi_s < 0 \qquad \{ 110 \}$$

The requirement of the synchronous phase ϕ_s is that it be set within the limits of the separatrix. With a change in sign of the phase slip factor, effectively the entire phase space shifts forward by an angle of π.

In the case of no acceleration, such as in a fixed-energy storage ring, $\cos \phi_s = 0$ and the stability condition is simply that the phase slip factor η_c is a negative number, which is true in general for all relativistic particles.

2.4.2.3 Gamma transition

With the appearance of the phase slip factor η_c in the expression for the synchrotron frequency, another important factor to observe is gamma transition. When the particle energy reaches a point where the $\eta_c = 0$, synchrotron oscillations cease as travel times becomes independent of momentum offset of particles. At regions close to this point, the RF cavity fails to produce or sustain a bunching effect, and the beam essentially becomes continuous. In addition, due to the absence of longitudinal focussing, particles may gain or lose too much energy which could cause very high momentum offsets, a steep rise in emittance and subsequent beam loss.

In accelerators, where the transition through this energy is unavoidable, schemes are designed to facilitate a "jump" through methods such as a well-timed temporary modification of the momentum compaction factor via additional fast quadrupoles [33].

2.5 6D Phase Space and Transfer Matrices

With a description of the phase space at each dimension described in the previous sections, it is now possible to define a 6-dimensional state vector which can be transported via 6×6 transfer matrices. Such a formalism not only would be a unified approach, but also would be exhaustive, since the state vector would now contain all the information there is to know about a particle, and the transfer matrix (or a set of them) can completely and accurately describe the effect of a field.

The state vector can be defined as follows:

$$\vec{\mathbf{w}} = \begin{pmatrix} x \\ x' \\ y \\ y' \\ z \\ \delta \end{pmatrix} \qquad \{ 111 \}$$

The transfer matrix would now be:

$$\boldsymbol{M} = \begin{pmatrix} r_{11} & r_{12} & r_{13} & r_{14} & r_{15} & r_{16} \\ r_{21} & r_{22} & r_{23} & r_{24} & r_{25} & r_{26} \\ r_{31} & r_{32} & r_{33} & r_{34} & r_{35} & r_{36} \\ r_{41} & r_{42} & r_{43} & r_{44} & r_{45} & r_{46} \\ r_{51} & r_{52} & r_{53} & r_{54} & r_{55} & r_{56} \\ r_{61} & r_{62} & r_{63} & r_{64} & r_{65} & r_{66} \end{pmatrix} = \begin{pmatrix} \boldsymbol{X} & & 0 & 0 & 0 & -D_x \\ & & 0 & 0 & 0 & -D_x' \\ 0 & 0 & \multicolumn{2}{c}{\multirow{2}{*}{$\boldsymbol{Y}$}} & 0 & 0 \\ 0 & 0 & & & 0 & 0 \\ D_x' & D_x & 0 & 0 & \multicolumn{2}{c}{\multirow{2}{*}{$\boldsymbol{Z}$}} \\ 0 & 0 & 0 & 0 & & \end{pmatrix} \qquad \{ 112 \}$$

Here, the coloured blocks are respectively the 2×2 transfer matrices for the radial, vertical and longitudinal phase spaces as described in previous sections. The numbers other than these represent coupling strengths between the different phase spaces.

It is interesting to note that the dispersion functions, described in section 2.3.2, which could not be included in the exclusive transverse phase space, now appear in this matrix as the coupling terms between the transverse coordinates and the longitudinal momentum offset.

The final block is the radial-longitudinal coupling. This is the converse effect of dispersion affecting transverse motion and is attributed to the curved nature of the ring's bending sections. In other words, it accounts for the fact that a particle with a positive x coordinate effectively covers an additional distance in the z direction due to the reduced circumference of the axially parallel path, and that a particle with a positive x' coordinate ends up travelling an additional distance in the z direction as it curves towards the beam axis.

2.5.1 Symplectic Condition

The symplectic condition in the realm of beam dynamics is the condition which is satisfied if the transfer matrices of the ring are mathematically symplectic. A symplectic matrix S is defined as a $n \times n$ square matrix with an even number of rows/columns that satisfies:

$$S = S^T J S \qquad \{ 113 \}$$

Where J is a fixed, non-singular skew-symmetric matrix. A typical choice for J is:

$$J = \begin{pmatrix} \mathbf{0} & I \\ -I & \mathbf{0} \end{pmatrix} \quad \{ 114 \}$$

…where I is a ${}^{n}/_{2} \times {}^{n}/_{2}$ identity matrix and $\mathbf{0}$ is a corresponding zero matrix. If the transfer map (the 6D one-turn matrix) of a ring is symplectic, then a six-dimensional volume element on the phase space would obey Liouville's theorem [34]. This also means that particle emittances are invariant over time.

Such a situation is however unlikely in practice, as there may be several effects that render the matrices non-symplectic, such as the effect of space charge in highly populated bunches [30] which tend to increase emittances. Beam emittances can be reduced using techniques such as electron or stochastic cooling [35] .

Another effect which leads to a violation of this condition is hadron interactions and Coulomb scattering of the particles with the residual gases in the ring. These effects lead to emittance growth-rates as well as beam losses [36] [37].

Apart from these there are many other phenomena that deviate real-world systems from having a symplectic transport. Due to this, emittances at various locations in synchrotrons are regularly measured and tracked [38].

2.6 Spin Dynamics in Storage rings

In this section the behaviour of the spin of particles when confined using storage rings is discussed.

2.6.1 Spin Precession

Most hadrons and the fundamental particles that make them have an Electric Dipole Moment ($\vec{d}$), a Magnetic Dipole Moment ($\vec{\mu}$) and a spin (or Spin Angular Momentum) ($\vec{\boldsymbol{s}}$)[1] simultaneously present.

Moreover, the two moments are aligned with the spin, so can be represented as multiples of the spin vector [39]:

[1] A particle's spin $\boldsymbol{s}$ will be shown in bold font to not be confused with the ring coordinate s

$$\vec{\mu} = g\frac{q}{2m}\vec{\boldsymbol{s}}$$
$$\vec{d} = \eta\frac{q}{2mc}\vec{\boldsymbol{s}} \qquad \{ 115 \}$$

Here, q and m are the charge and mass of the particle. g is termed the Gyro-magnetic Ratio, and η is termed the Gyro-electric Ratio. These are characteristic values for a particle.

To measure the EDM of such a particle with a storage ring, one needs to consider that the interactions of each of the dipole moments with their respective fields introduces a precession of the particle's spin, and that they are also influenced by the relativistic motion and acceleration around the ring.

One can start with the simplest case of a particle at rest under the influence of an external magnetic field. The particle undergoes Larmor Precession, which is the precession of its magnetic moment around the field. Essentially, the field applies a torque ($\frac{d\vec{\boldsymbol{s}}}{dt}$) on the particle, which characterises the precession.

$$\left[\frac{d\vec{\boldsymbol{s}}}{dt}\right]_{MDM} = \vec{\mu} \times \vec{B} \qquad \{ 116 \}$$

Since the MDM is aligned with the spin, and the spin axis follows the direction of the torque, the axis of the precession is in fact, the direction of the magnetic field, i.e., the particle spin axis rotates around the field axis.

Similarly, the EDM of a particle interacts with an external electric field in the same way:

$$\left[\frac{d\vec{\boldsymbol{s}}}{dt}\right]_{EDM} = \vec{d} \times \vec{E} \qquad \{ 117 \}$$

So, the combined effects of the fields on the dipole moments results in a combined precession, given by the vector sum of the individual torques.

$$\frac{d\vec{\boldsymbol{s}}}{dt} = \left[\frac{d\vec{\boldsymbol{s}}}{dt}\right]_{MDM} + \left[\frac{d\vec{\boldsymbol{s}}}{dt}\right]_{EDM} = \left(\vec{\mu} \times \vec{B}\right) + \left(\vec{d} \times \vec{E}\right) \qquad \{ 118 \}$$

Classically, the precession of a spinning object under the influence of a force (like gravity) is modelled according to the precession equation [40]:

$$\frac{d\vec{\boldsymbol{s}}}{dt} = \vec{\Omega} \times \vec{L} \qquad \{ 119 \}$$

Where $\vec{L}$ is the angular momentum of the object's spinning motion. Modelling the precession of the particle in this manner, by representing it as a cross product with the spin angular momentum $\vec{s}$, has the advantage that the precession frequency and axis are directly accessible via the magnitude and direction of $\vec{\Omega}$. Using the relations { 115 }, the total torque can be written as:

$$\frac{d\vec{\boldsymbol{s}}}{dt} = \vec{\Omega} \times \vec{\boldsymbol{s}} = -\frac{q}{2m}\left(g\vec{B} + \frac{\eta}{c}\vec{E}\right) \times \vec{\boldsymbol{s}} \qquad \{ 120 \}$$

Which gives us the axis of spin precession (also known as the "invariant spin axis"):

$$\vec{\Omega} = -\frac{q}{2m}\left(g\vec{B} + \frac{\eta}{c}\vec{E}\right) \qquad \{ 121 \}$$

While this expression is useful for a particle at rest, this is not the case for particles in a storage ring. In fact, the motion of the particles at relativistic velocities, and its impact on the spin motion must also be accounted for. The way this is done is to represent the torque in its Lorentz Invariant form, which would hold true in all relativistic reference frames [41]. Applying the Lab-frame parameters in such an expression would give us the expression for the spin precession of the particles in the storage ring. This was calculated precisely in [41] and [42] for a storage ring with a vertical magnetic field and a radial electric field, both perpendicular to the direction of motion, thereby giving the expression:

$$\begin{aligned}\frac{d\vec{\boldsymbol{s}}}{dt} = -\frac{q}{m}\Bigg[&\left(G + \frac{1}{\gamma}\right)\vec{B} - \frac{G\gamma}{\gamma+1}\left(\frac{\vec{v}\cdot\vec{B}}{c^2}\right)\vec{v} - \frac{1}{c}\left(G + \frac{1}{\gamma+1}\right)\vec{v}\times\vec{E} \\ &+ \frac{\eta}{2}\left(\vec{E} - \frac{\gamma}{\gamma+1}\left(\frac{\vec{v}\cdot\vec{E}}{c^2}\right)\vec{v} + \vec{v}\times\vec{B}\right)\Bigg] \times \vec{\boldsymbol{s}}\end{aligned} \qquad \{ 122 \}$$

This is known as the Thomas-Bargmann-Michel-Telegdi (or Thomas-BMT) Equation. Here, $\vec{v}$ is the particle velocity, $\gamma = \left(1 - \frac{v^2}{c^2}\right)^{-1/2}$ is the Lorentz Factor, and $G = \frac{g}{2} - 1$ is the gyromagnetic "anomaly"; all of which typically remain constant.

For the purposes of our storage ring, both the confinement fields and the velocity are usually maintained mutually perpendicular to each other. Thus making $\vec{v} \cdot \vec{B} = 0$ and $\vec{v} \cdot \vec{E} = 0$. This reduces the above expression to:

$$\frac{d\vec{\boldsymbol{s}}}{dt} = -\frac{q}{m}\left[\left(G+\frac{1}{\gamma}\right)\vec{B} - \left(G+\frac{1}{\gamma+1}\right)\vec{v}\times\vec{E} + \frac{\eta}{2}\left(\vec{E}+\vec{v}\times\vec{B}\right)\right]\times\vec{\boldsymbol{s}} \qquad \{ 123 \}$$

From this expression, the precession components due to the electric and magnetic dipole moments are immediately discernible:

$$\vec{\Omega}_{MDM} = -\frac{q}{m}\left(\left(G+\frac{1}{\gamma}\right)\vec{B} - \left(G+\frac{1}{\gamma+1}\right)\vec{v}\times\vec{E}\right) \qquad \{ 124 \}$$

$$\vec{\Omega}_{EDM} = -\frac{q\eta}{2m}\left(\vec{E}+\vec{v}\times\vec{B}\right) \qquad \{ 125 \}$$

These frequencies are now with respect to the lab frame. However, it is often useful, especially in the experiments discussed in this thesis, to calculate the precession frequency with respect to the particle's momentum vector. The frequency of rotation of the momentum vector is given by [42]:

$$\vec{\Omega}_p = -\frac{q}{\gamma m}\left(\vec{B} - \frac{1}{v^2}\left(\vec{v}\times\vec{E}\right)\right) \qquad \{ 126 \}$$

With this, the frequency of precession on the ring-plane relative to the particle's velocity vector can be defined:

$$\left[\vec{\Omega}_{MDM}\right]_{rel} = \vec{\Omega}_{MDM} - \vec{\Omega}_p = -\frac{q}{m}\left(G\vec{B} - \left(G-\frac{1}{\gamma^2-1}\right)\vec{v}\times\vec{E}\right) \qquad \{ 127 \}$$

Finally, from this, the net precession of the particle spin with respect to the momentum can be described by the vector sum:

$$\vec{\Omega} = \left[\vec{\Omega}_{MDM}\right]_{rel} + \vec{\Omega}_{EDM} \qquad \{ 128 \}$$

…and the Thomas BMT equation from this perspective becomes:

$$\frac{d\vec{\boldsymbol{s}}}{dt} = -\frac{q}{m}\left[G\vec{B} - \left(G-\frac{1}{\gamma^2-1}\right)\vec{v}\times\vec{E} + \frac{\eta}{2}\left(\vec{E}+\vec{v}\times\vec{B}\right)\right]\times\vec{\boldsymbol{s}} \qquad \{ 129 \}$$

2.6.2 Spin transfer matrix

To obtain the matrix formalism for spin transfer, the Thomas BMT equation must be transformed into the Frenet frame:

$$\frac{d\vec{\boldsymbol{s}}}{ds} = \frac{1}{v}\frac{d\vec{\boldsymbol{s}}}{dt} = -\frac{q}{p}\left[\gamma G\vec{B} - \gamma\left(G - \frac{1}{\gamma^2 - 1}\right)\vec{v}\times\vec{E} + \frac{\eta\gamma}{2}\left(\vec{E} + \vec{v}\times\vec{B}\right)\right]\times\vec{\boldsymbol{s}} \qquad \{\ 130\ \}$$

The case of a pure magnetic ring is considered first. Using { 19 }, the above equation reduces to (ignoring the EDM effect for now):

$$\frac{d\vec{\boldsymbol{s}}}{ds} = -\frac{1}{\rho}\gamma G(\hat{y})\times\vec{\boldsymbol{s}} = -\frac{\gamma}{\rho}G\begin{pmatrix}0 & 0 & 1\\ 0 & 0 & 0\\ -1 & 0 & 0\end{pmatrix}\vec{\boldsymbol{s}} = -\frac{\gamma}{\rho}GA\vec{\boldsymbol{s}} \qquad \{\ 131\ \}$$

The above differential equation for the spin is a first order equation, thus a first order state vector, like $\vec{\boldsymbol{s}}$, would exhaustively hold all the information relevant for transport through the system. So, the solution below is used to solve the differential equation:

$$\vec{\boldsymbol{s}} = \left(e^{-\frac{\gamma}{\rho}GAs}\right)\vec{\boldsymbol{s}}_0 \qquad \{\ 132\ \}$$

The exponential above can be simplified using these relations:

$$A^2 = \begin{pmatrix}-1 & 0 & 0\\ 0 & 0 & 0\\ 0 & 0 & -1\end{pmatrix} \qquad \{\ 133\ \}$$

$$A^{n+2} = -A^n \quad A^{n+4} = A^n \quad \forall \quad n = 1, 2, 3, \ldots \qquad \{\ 134\ \}$$

$$e^{\vartheta} = \sum_{i=0}^{\infty}\frac{\vartheta^i}{i!} \quad \cos\vartheta = \sum_{i=0}^{\infty}(-1)^i\frac{\vartheta^{2i}}{(2i)!} \quad \sin\vartheta = \sum_{i=0}^{\infty}(-1)^{i+1}\frac{\vartheta^{2i+1}}{(2i+1)!} \qquad \{\ 135\ \}$$

The expression { 132 } can now be written as:

$$\vec{\boldsymbol{s}} = \begin{pmatrix}\cos\Theta & 0 & \sin\Theta\\ 0 & 1 & 0\\ -\sin\Theta & 0 & \cos\Theta\end{pmatrix}\vec{\boldsymbol{s}}_0 = \boldsymbol{S}_{s/0}\vec{\boldsymbol{s}}_0 \qquad \{\ 136\ \}$$

Here, $\Theta = \nu_s\theta = \gamma G\theta$ is the spin phase advance, ν_s is called the spin tune, $\theta = \frac{s}{\rho}$ is the ring angle as depicted in Figure 16, and $\boldsymbol{S}_{s/0}$ is the spin transfer matrix. It can be seen that in the Frenet frame, the spin precesses at a frequency of $\nu_s = \gamma G$. For a pure magnetic ring, this would be the largest contribution to the particle's spin precession.

In the case of a storage ring with both electric and magnetic fields being used for confinement (ignoring the EDM effect), the expression for the rate of change of the spin becomes:

$$\frac{d\vec{\boldsymbol{s}}}{ds} = -\frac{1}{\rho}\left(\frac{1}{{}^{E}/_{v} + B}\right)\left[\gamma GB + \gamma\left(G - \frac{1}{\gamma^2 - 1}\right)vE\right](\hat{y}) \times \vec{\boldsymbol{s}} \qquad \{ 137 \}$$

…where the radius of curvature ρ would now be determined by the combination of both fields:

$$\rho = \frac{p}{q\left({}^{E}/_{v} + B\right)} \qquad \{ 138 \}$$

Recalculating using the above process gives the updated value of the spin tune in a combined-field storage ring:

$$\nu_s = \gamma G - \frac{r(G+1)}{\gamma(\beta + r)} \qquad \{ 139 \}$$

Where $r = {}^{E}/_{cB}$ is the normalized field ratio, and $\beta = {}^{v}/_{c}$.

A general formalism for the spin transfer matrix can be obtained using a similar approach from the expression:

$$\frac{d\vec{\boldsymbol{s}}}{ds} = \frac{\vec{\Omega}}{v} \times \vec{\boldsymbol{s}} = \frac{1}{v}\begin{pmatrix} 0 & -\Omega_z & \Omega_y \\ \Omega_z & 0 & -\Omega_x \\ -\Omega_y & \Omega_x & 0 \end{pmatrix}\vec{\boldsymbol{s}} = \left(\frac{\Omega_x}{v}L_x + \frac{\Omega_y}{v}L_y + \frac{\Omega_z}{v}L_z\right)A\vec{\boldsymbol{s}} \qquad \{ 140 \}$$

Here, Ω_x, Ω_y and Ω_z are the components of the spin precession frequency $\vec{\Omega}$ of the particle. $L_x = \begin{pmatrix} 0 & 0 & 0 \\ 0 & 0 & -1 \\ 0 & 1 & 0 \end{pmatrix}$, $L_y = \begin{pmatrix} 0 & 0 & 1 \\ 0 & 0 & 0 \\ -1 & 0 & 0 \end{pmatrix}$ and $L_z = \begin{pmatrix} 0 & -1 & 0 \\ 1 & 0 & 0 \\ 0 & 0 & 0 \end{pmatrix}$ are the basis vectors of the $\mathfrak{so}(3)$ Lie Algebra associated with the group of 3D rotation matrices [43]. These can be exponentiated to get the rotation matrices around the x, y and z axes in a fashion similar to that done in the earlier example. The generalized spin transfer matrix now becomes:

$$\boldsymbol{S}_{s_2/s_1} = R_x\left(\frac{\Omega_{x_2}s_2 - \Omega_{x_1}s_1}{v}\right)R_y\left(\frac{\Omega_{y_2}s_2 - \Omega_{y_1}s_1}{v}\right)R_z\left(\frac{\Omega_{z_2}s_2 - \Omega_{z_1}s_1}{v}\right) \qquad \{ 141 \}$$

Here, $\boldsymbol{S}_{s_2/s_1}$ is a spin transfer matrix from $s = s_1$ to $s = s_2$. $R_u(\vartheta)$ is a 3D rotation matrix around the u-axis. The lower indices on the precession frequency components

accommodate for the possibility that two locations on the ring may have different turning angles on the spin.

2.6.3 Polarisation vector for fermions

In storage rings, it is often not practical to store a single particle and obtain measurables. For this reason, rings store and measure bunches or ensembles of upwards of a billion particles. These are referred to as "beams" and the process of tracking and performing measurements on beams is called beam tracking. Thus, in practice, a more convenient approach to tracking each particle's individual spin would be to track a single vector quantity associated with a bunch.

To do this, the definition of the individual spin vector is first formalised. The quantum state of a fermion (spin-$^1/_2$ particle) can be represented as a two-component "spinor" [44]:

$$\boldsymbol{\psi} = \begin{pmatrix} u \\ d \end{pmatrix} \qquad \{ 142 \}$$

Here, u and d are the complex amplitudes associated with the two spin states of the particle, which follow the normalization condition $\boldsymbol{\psi}^*\boldsymbol{\psi} = 1$. The spin component along each axis is associated with a Hermitian operator. Under the choice of z as the quantization axis, these can be defined using the Pauli spin operator:

$$\hat{\vec{S}} = \frac{\hbar}{2}\vec{\sigma} \qquad \{ 143 \}$$

Where $\vec{\sigma} = \begin{pmatrix} \sigma_1 \\ \sigma_2 \\ \sigma_3 \end{pmatrix}$ is a vector of the Pauli matrices $\sigma_1 = \begin{pmatrix} 0 & 1 \\ 1 & 0 \end{pmatrix}$, $\sigma_2 = \begin{pmatrix} 0 & -i \\ i & 0 \end{pmatrix}$ and $\sigma_3 = \begin{pmatrix} 1 & 0 \\ 0 & -1 \end{pmatrix}$.

The spin vector $\vec{\boldsymbol{s}}$ can now be obtained as the expectation value of the spin operator on the spinor:

$$\vec{\boldsymbol{s}} = \left\langle \boldsymbol{\psi} \middle| \hat{\vec{S}} \middle| \boldsymbol{\psi} \right\rangle = \begin{pmatrix} 2Re(ud^*) \\ 2Im(ud^*) \\ |u|^2 - |d|^2 \end{pmatrix} \qquad \{ 144 \}$$

This three-component real vector is the expectation value of the particle's spin. However, an actual measurement of the particle spin using a polarimeter would yield either $+^1/_2$ or $-^1/_2$, whose probability of occurrence depends on the

measurement axis. So, what this vector actually conveys is the specific axis along which the probability of measuring a spin of $+1/2$ is maximized.

With this definition of the individual particle spin, the polarisation vector $\vec{P}$ can be defined for a bunch of N particles:

$$\vec{P}(t) = \frac{1}{N}\sum_{i=1}^{N}\frac{\vec{s}_i(t)}{|\vec{s}_i(t)|} \quad \{ 145 \}$$

When a bunch of billions of particles is considered, each of which has the same expectation value, and is measured for its spin orientation along a given axis $\vec{a}$, the interpretation of probability now turns into share of outcomes, and the magnitude of the polarisation vector in such a measurement would approach:

$$\left|\vec{P}(t)\right| \approx \vec{s}.\vec{a} \quad \{ 146 \}$$

2.6.4 Spin resonances

A spin resonance, analogous to the betatron resonance, is a condition where aberrations due to device imperfections are resonantly amplified due to the state being the same at each turn. In spin resonances, the defects usually manifest as localised loss of uniformity in the spins of particles at a region of the bunch. This, combined with a resonance, results in a loss of polarization due to rapid decoherence of particles. This can be explored in an example of an idealized pure-magnetic ring. The spin transfer map (one-turn matrix) of the ring can be written as follows:

$$\boldsymbol{S}_{s+L/s} = \begin{pmatrix} \cos 2\pi\nu_s & 0 & \sin 2\pi\nu_s \\ 0 & 1 & 0 \\ -\sin 2\pi\nu_s & 0 & \cos 2\pi\nu_s \end{pmatrix} \quad \{ 147 \}$$

Just like in beam transport systems (see section 2.3.1.3), it can be observed that resonance is achieved when the transfer map becomes the identity matrix. This allows the interpretation of the resonance conditions [45]:

$$\nu_s = j \quad \{ 148 \}$$

$$\nu_s = jP + mQ_y \quad \{ 149 \}$$

$$\nu_s = j + mQ_x + nQ_y + iQ_z \quad \{ 150 \}$$

Here, i, j, m and n are integers. Condition { 148 } is known as an imperfection resonance, usually attributed to field and positioning errors of magnets. Condition

{ 149 } is known as an intrinsic resonance, which can be caused by vertical focussing defects. Finally, { 150 } describe a class of resonances called higher order resonances. These can be triggered by sextupole errors or synchrotron motion. In each case, similar to the betatron case, higher indices have a milder impact on decoherence.

2.6.5 Spin coherence time and spin tune spread

As discussed earlier, practical storage ring measurements take place on beams of particles rather than individual particles. This has the benefit of an amplification of measurables, but also the downside that for measurables in particle bunches to have a higher statistical certainty, it is important for them to behave as uniformly as possible. In the case of particle spins, it is better for the measurement of quantities like EDM for the spins of all the particles in the beam to have nearly the same spin at any given time. In the pure magnetic case, the precession frequency is given by $\nu_s = \gamma G$. Assuming that the particles are initially perfectly polarised so that $\left|\vec{P}(0)\right| = 1$, this polarization will be maintained as long as each particle in the beam is travelling at the same speed as the reference particle. However, this may not always be the case.

The largest effect from the particle phase space that directly influences the spin tune would be the momentum deviation δ, as this would create a distribution of γ values in the beam. However, this is a first order effect and can be cancelled out in the long run by bunching using an RF cavity [46]. First order effects in the transverse direction are also cancelled out by betatron oscillations. This is because the particle spends an equal amount of time with a lower γ as with a higher γ, which evens out the error in spin phase advance on average.

Second order effects on the other hand, may cause a divergence in spin tune. This can be caused by transverse as well as longitudinal motion.

2.6.5.1 Path shortening effect of transverse motion

Considering exclusively linear betatron motion, a particle travelling in a storage ring does not experience a change in path length due to the betatron motion. However, second-order betatron motion induces a change in path length. This was calculated extensively in [47], and shown to be:

$$\left(\frac{\Delta L}{L}\right)_{\beta} = -\frac{\pi}{L}\left(\epsilon_x \xi_x + \epsilon_y \xi_y\right) \qquad \{ 151 \}$$

2.6.5.2 Path lengthening effect of longitudinal motion

Second-order effects in the synchrotron motion can lead to a quadratic dependence of the path length on the momentum offset. This kind of

dependence is sign-preserving and is not cancelled out by the RF bunching. This effect is quantified by the second order momentum compaction factor α_1, defined in { 95 }.

2.6.5.3 Spin Coherence Time (SCT)

Considering the change in path length due to betatron motion and an expansion up to the second order, the effective change in path length would be given by [22]:

$$\frac{\Delta L}{L} = -\frac{\pi}{L}\left(\epsilon_x \xi_x + \epsilon_y \xi_y\right) + \alpha_0 \delta + \alpha_1 \delta^2 \qquad \{ 152 \}$$

Since first-order path lengthening is cancelled out by RF bunching, this reduces to:

$$\frac{\Delta L}{L} = \alpha_1 \delta^2 - \frac{\pi}{L}\epsilon_x \xi_x - \frac{\pi}{L}\epsilon_y \xi_y \qquad \{ 153 \}$$

This path lengthening effect in combination with the bunching due to the RF cavity implies that the particle deviates from its synchronous phase and receives energy from the cavity over each turn until its changed momentum compensates for the longer path it must travel. This also implies that this particle now precesses with a different tune, thus contributing to decoherence.

This simple model indicates the parameters that have maximum influence on the decoherence effect. However, this applies to a pure magnetic ring, which is not the case with a combined-field ring. Moreover, there may be other systematic effects that also affect decoherence. Thus, a direct measurement of this phenomenon would likely be an important diagnostic tool.

To measure and quantify the decoherence phenomenon, the spin coherence time (τ) is defined, as the time at which the magnitude of the polarisation vector reduces to $1/e$ of its initial value:

$$\left|\vec{P}(\tau)\right| = \frac{1}{e}\left|\vec{P}(0)\right| \qquad \{ 154 \}$$

The spin coherence time directly tracks the magnitude of the polarisation vector to measure the rate of decoherence. However, decoherence, depending on the distribution of the precession error, may also change the direction of the polarisation vector with respect to the reference particle. This is, in a sense, an asymmetric decoherence effect, since a bunch is usually centred at the reference particle, which by definition, has no precession error. Thus, a disagreement between the spin axes of the reference particle and the polarisation vector

indicates an asymmetry in the decoherence, which could be a phenomenon of interest.

2.6.5.4 Spin Tune Spread (STS)

The spin tune spread $\Delta\theta_x$ measures the change in the direction of the polarisation vector from the reference particle in the plane of precession (here, assumed to be the ring plane):

$$\Delta\theta_x(t) = \cos^{-1}\left(\frac{\vec{P}(t)\cdot[\![\vec{s}(t)]\!]}{\left|\vec{P}(t)\right|\left|[\![\vec{s}(t)]\!]\right|}\right) \approx tan^{-1}\left(\frac{P_x(t)}{[\![s_z(t)]\!]}\right) \qquad \{\ 155\ \}$$

Here, P_x is the radial component of the polarization vector, and the hollow square brackets $[\![\ \ ]\!]$ indicate properties of the reference particle. Also interesting is the spin tune error $\Delta\nu_x(t)$, which is the rate of change of spin tune spread.

$$\Delta\nu_x(t) = \frac{d}{dt}\left(\Delta\theta_x(t)\right) \qquad \{\ 156\ \}$$

The spin tune error can be seen as an error on the spin tune ν_s contributed by the depolarizing effects in the storage ring.

3. EDM Measurement using Spin Precession in Storage Rings

In an experiment to measure the EDM of a particle carried out in a storage ring, the focus would be the measurement of $\vec{d}$, or by extension, the gyro-electric ratio η. If the so-called "spin tune" and the invariant spin axis (given respectively by the magnitude and direction of $\vec{\Omega}$) were measured precisely, the EDM component $\vec{\Omega}_{EDM}$ can be resolved, and thus η can be determined from { 129 }.

In the case where longitudinally polarised particles are injected into the storage ring, the precession frequency can be measured precisely using polarimeters, since the precession would occur on the horizontal plane and there would be a wide enough disparity between the signal generated by the left and right polarised particles. For rings like COSY, which demonstrate spin tunes of around $120\ kHz$ [48], it can be measured using a polarimeter with only a $5\ kHz$ detection rate up to a precision level of 10^{-11} using a novel technique developed by JEDI in [49].

The measurement technique to determine the invariant spin axis, however, would depend on the configuration of the storage ring fields.

3.1.1 Strategy at pure magnetic storage rings

A pure magnetic ring is a storage ring which uses only magnetic fields to confine the particles. In the absence of electric fields, the Thomas-BMT equation { 129 } reduces to:

$$\frac{d\vec{s}}{dt} = -\frac{q}{m}\left[G\vec{B} + \frac{\eta}{2}\left(\vec{v} \times \vec{B}\right)\right] \times \vec{s} \qquad \{ 157 \}$$

This gives the precession components due to the MDM around the vertical axis ($\left[\vec{\Omega}_{MDM}\right]_{rel}$) and the EDM around the radial axis ($\vec{\Omega}_{EDM}$):

$$\left[\vec{\Omega}_{MDM}\right]_{rel} = -\frac{qG}{m}\vec{B} \qquad \{ 158 \}$$

$$\vec{\Omega}_{EDM} = -\frac{q\eta}{2m}\vec{v} \times \vec{B} \qquad \{ 159 \}$$

The invariant spin axis $\hat{\Omega}$, therefore lies somewhere along the transverse plane. Since $|\vec{\Omega}_{EDM}| \ll \left|\left[\vec{\Omega}_{MDM}\right]_{rel}\right|$, the magnitude $|\vec{\Omega}|$ can be measured with high precision using polarimeters as discussed earlier. However, to measure the direction $\hat{\Omega}$ with sufficient precision, an additional effect must be introduced, which must fulfil the following three conditions:

1. The motion of the particles must not be affected
2. The intensity depends on the direction of the invariant spin axis.
3. Its precision can be controlled.

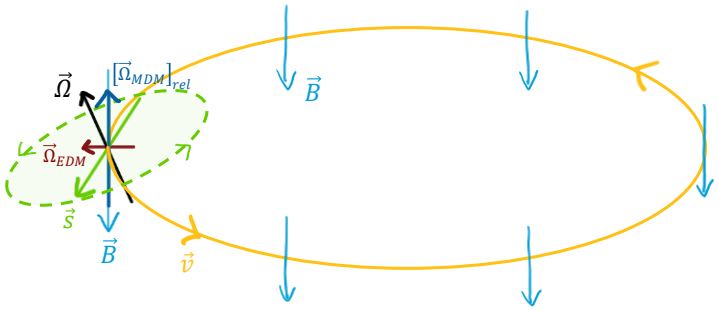

Figure 20: A diagram showing the orientation of the invariant spin axis on the transverse plane in a pure magnetic ring. The axis is tilted outward due to the EDM component of the precession.

One such method is to use a Radio-Frequency Wien filter. A Wien filter is a device which exposes a beam travelling in a longitudinal direction to simultaneous transverse electric and magnetic fields, both perpendicular to each other.

The original idea behind its design was to be able to select charged particles with a certain velocity such that the net Lorentz force acting on the particle was zero.

$$\vec{F} = q\left(\vec{E}_W + \vec{v} \times \vec{B}_W\right) = 0 \qquad \{ 160 \}$$

Here, $\vec{E}_W$ and $\vec{B}_W$ are the electric and magnetic fields applied by the Wien filter. Since the fields and the particle velocity are mutually perpendicular, this gives rise to the Lorentz force cancellation condition for the velocity:

$$v = \frac{E_W}{B_W} \qquad \{ 161 \}$$

This would be the "selected" velocity which would move through the Wien filter without being deviated from its straight path.

In the storage ring, the Wien filter is installed in a straight section, where bending fields are absent, and the particle simply drifts in a linear path. Since the storage ring is a synchrotron, the particle velocity is fixed by design. So, the Wien filter is set up such that this fixed velocity satisfies the cancellation condition. This way, the particle motion is unaffected.

However, the particle spin is affected by a torque according to { 129 }, which when combined with the situation in { 160 }, introduces a precession of the spin strictly around the Wien filter's magnetic field axis.

$$\vec{\Omega}_W = \frac{q}{m}\left(\frac{1}{\gamma^2 - 1}\right)\vec{v} \times \vec{E}_W \qquad \{ 162 \}$$

Here, the precession frequency due to the Wien filter $\vec{\Omega}_W$ may have a different direction than the default precession $\vec{\Omega}$ due to the synchrotron.

Finally, the fields of this "Radio-Frequency" Wien filter are varied sinusoidally at a frequency exactly equal to Ω, such that the cancellation condition { 161 } is always obeyed.

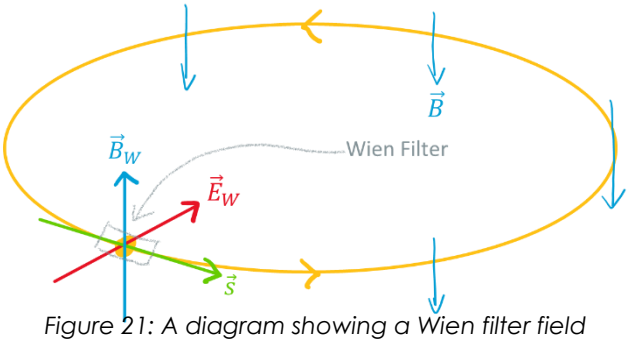

Figure 21: A diagram showing a Wien filter field configuration with the electric and magnetic fields along the radial and vertical axes. The axis of precession (kicks) due to the Wien filter would be exactly along $\vec{B}_W$.

$$E_W = E_{W_0}\cos\Omega t$$
$$B_W = B_{W_0}\cos\Omega t \qquad \{ 163 \}$$

Assuming that at $t = 0$, the particles are longitudinally polarised, and that the invariant spin axis $\hat{\Omega}$ is offset from the Wien filter's precession axis $\hat{\Omega}_W$ by an angle θ, the situation implies that the particle now begins to gradually spiral up towards becoming vertically polarised. This occurs because (assuming the Wien filter is configured according to Figure 21) the Wien filter effectively kicks the spin vector in the anticlockwise direction when it faces forward, and in the clockwise direction when it faces backward. When this happens for a non-zero θ, each kick closes the angle between $\vec{s}$ and $\vec{\Omega}$, thus steadily raising the "latitude" of the precession at a rate proportional to θ.

In such a setup, to locate the invariant spin axis, the special case can be exploited where $\vec{\Omega}_W$ is aligned with $\vec{\Omega}$ and there occurs no upshift of the spin. This is because, in this case, the kicks to the spin keep it on the same plane of precession. Since this happens only at the specific orientation of the Wien filter where $\vec{B}_W$ is aligned with $\vec{\Omega}$, the invariant spin axis can be found by rotating the Wien filter around the

beam axis by an angle φ_W with respect to the vertical axis, until the rate of observable upshift of the spin is zero. Thus, the angle φ_W would be its estimated orientation.

3.1.2 Strategy at combined-field storage rings

A combined-field storage ring is a ring which can use magnetic and electric fields simultaneously for confining particles. Such a storage ring offers an opportunity to avoid many sources of systematic errors such as Wien filters and its highly specific configuration.

In the combined ring, where the spin precession is governed by { 129 }, it is possible to set the value of $\vec{E}$ and $\vec{B}$ such that:

$$G\vec{B} + \left(G - \frac{1}{\gamma^2 - 1}\right)\vec{v} \times \vec{E} = 0 \qquad \{ 164 \}$$

At this field setting, it is clear that $\left[\vec{\Omega}_{MDM}\right]_{rel}$, which is the precession in the horizontal plane relative to the particle's velocity vector now vanishes. This implies that if not for the EDM effects, the orientation of the spin on the horizontal plane is always fixed with respect to the velocity. Thus, particles injected with longitudinal polarisation will stay that way. This condition is termed "frozen spin" and is only possible if electric fields are involved in confinement.

For frozen spin particles in the combined ring, the Thomas-BMT equation is reduced to:

$$\frac{d\vec{s}}{dt} = \vec{\Omega}_{EDM} \times \vec{s} \qquad \{ 165 \}$$

Here, $\vec{\Omega}_{EDM}$ is given by { 125 }, meaning that the invariant spin axis now lies on the horizontal plane along the radial axis. Measurement of EDM in this case is quite straightforward with progressive measurements of vertical polarisation using polarimeters.

3.1.3 Strategy at pure electrostatic storage rings

A pure electric storage ring uses only electric fields for particle confinement. In this kind of a storage ring, the Thomas-BMT equation becomes:

$$\frac{d\vec{s}}{dt} = -\frac{q}{m}\left[\left(G - \frac{1}{\gamma^2 - 1}\right)\vec{v} \times \vec{E} + \frac{\eta}{2}\vec{E}\right] \times \vec{s} \qquad \{ 166 \}$$

Where:

$$\left[\vec{\Omega}_{MDM}\right]_{rel} = -\frac{q}{m}\left(G - \frac{1}{\gamma^2 - 1}\right)\vec{v} \times \vec{E} \qquad \{ 167 \}$$

$$\vec{\Omega}_{EDM} = -\frac{q\eta}{2m}\vec{E} \qquad \{ 168 \}$$

For particles with positive gyromagnetic anomalies (such as the proton), it is possible to achieve a frozen spin in such a ring by setting the particle momentum at a specific value such that:

$$\frac{1}{\gamma^2 - 1} = G \qquad \{ 169 \}$$

In this case, the horizontal precession $\left[\vec{\Omega}_{MDM}\right]_{rel}$ vanishes. The precession in the vertical plane is directly measured with polarimeters, and the EDM, from { 168 }, which has only one field term. This would leave minimum sources of systematic errors to optimize and thus allows for maximum precision in EDM measurement.

3.2 Stages of the EDM experiment

From the three strategies described in the previous section, the progression in sensitivity is clear and can be attributed to the reduction in systematic sources of error. To this end, JEDI plans to approach the task of EDM measurement in a staged approach [8], following this progression. Details about each of the stages of the approach is shown in Figure 22.

1 Precursor Experiment	→	2 Prototype Ring	→	3 All-electric Ring
dEDM proof-of-capability (orbit and polarisation control; first dEDM measurement)		**pEDM proof-of-principle** (key technologies, first direct pEDM measurement)		**pEDM precision experiment** (sensitivity goal: 10^{-29} *e* cm)
- Magnetic storage ring - Polarised deuterons - d-Carbon polarimetry - Radio-frequency Wien filter		- High-current all-electric ring - Simultaneous CW/CCW op. - Frozen spin control (with combined *E*/*B*-field ring) - Phase-space beam cooling		- Frozen spin all-electric (at p = 0.7 GeV/c) - Simultaneous CW/CCW op. - *B*-shielding, high *E*-fields - Design: cryogenic, hybrid,…
Ongoing at COSY (Jülich) 2014 → 2021		Ongoing within CPEDM 2017 → 2020 (CDR) → 2022 (TDR) Start construction > 2022		After construction and operation of prototype > 2027

Figure 22: Some specifications of the staged approach currently pursued by the JEDI collaboration for proton EDM measurement. [8]

With each stage, important benchmarks are set, which reduce uncertainties in projected results as well as precision capabilities of future projects. The following

subsections will proceed to give a brief overview of each of the projects, highlighting the features that provide key insights to the proton EDM search.

3.2.1 Precursor stage: COSY

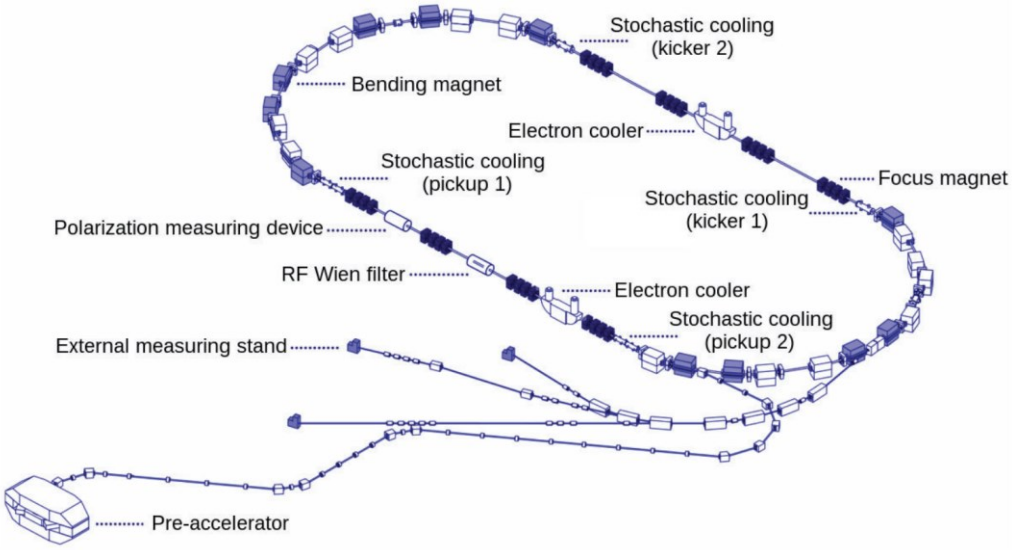

Figure 23: A picture describing the layout of COSY, showing the JULIC ion source and cyclotron, the stacked stripping injection path, and the "racetrack" style synchrotron. Also labelled are the various components. [50]

The COoler SYnchrotron or COSY accelerator facility is located at the Forschungszentrum, Jülich, Germany and consists of three main parts: an ion source the injection cyclotron (known as JULIC) and finally the main synchrotron ring. The ring was designed to function as a synchrotron to provide proton beams for fixed target experiments, and also as a storage ring for precision measurements on polarized protons [7].

In practice, the COSY synchrotron can also be used to store deuterons, as the ion source is actually capable of producing either polarized or unpolarized H^- or D^- [51]. The initial cyclotron is capable of pre accelerating the H^- or D^- ions up to kinetic energies of 45 or 75 MeV respectively [52]. The pre accelerated beam is then injected into the main synchrotron ring via a stacked stripping injector where the two electrons are stripped from each of the ions using a carbon foil before they enter the ring, resulting in a final beam of protons or deuterons.

The COSY synchrotron can accelerate particles up to a maximum of 3.7 GeV. This acceleration is carried out using an RF cavity located in the middle of one of the straight sections. The ring has 24 bending magnets each of which can reach a maximum magnetic field of 1.67 T for maintaining the closed loop. For focusing the beam COSY has 56 quadrupole magnets which are grouped into families of four. Quadrupoles within a family have the same dimensions and a common

power supply. Eight of these families are located in the straight sections, and 6 of them in the arcs. In addition, COSY also has 17 sextupoles, of which 7 are in the straight sections and 10 are positioned in the arcs. Finally for orbit measurements and corrections COSY makes use of 59 beam position monitors and 41 "steering" magnets (small dipoles for minor transverse path corrections).

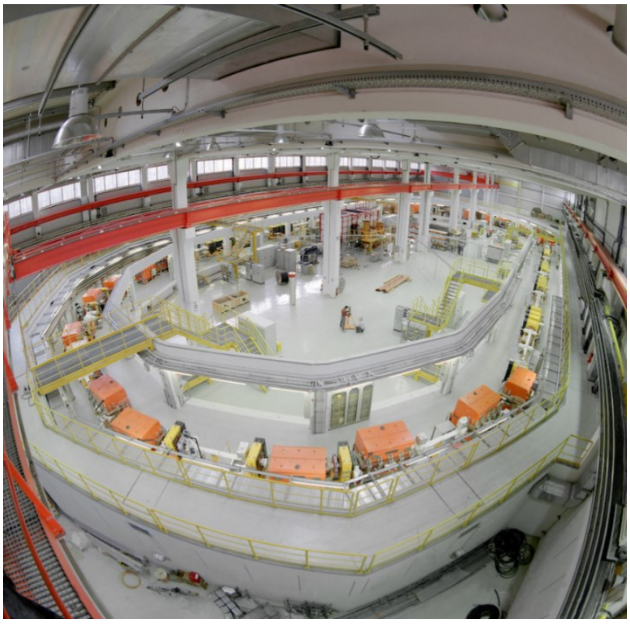

Figure 24: A photograph of the COoler SYnchrotron (COSY) accelerator and storage ring at the Forschungszentrum, Jülich, Germany. [82]

More importantly, COSY is called the cooler synchrotron because of its phase space cooling devices. There are two electron coolers for phase space cooling at particle momenta up to 0.6 GeV [53] [54], as well as stochastic cooling mechanisms for those with momenta above 1.5 GeV [55]. A combination of all these devices is used to ensure the lowest possible emittances on the beam.

Apart from being able to maintain a highly precise beam, the COSY synchrotron has 2 polarimeters called WASA (Wide Angle Shower Apparatus) and JEPO (JEdi POlarimeter) for measurement of beam polarization, an RF Wien filter to help with the EDM measurement and solenoids for spin axis adjustments. Besides all this COSY also has three exit beam lines with magnetic septa for extraction of the beam towards external experiments [50].

3.2.2 Proof-of-concept stage: The Prototype EDM Storage ring

The prototype EDM ring is the storage ring which plays the role of the intermediate step in order to obtain the crucial data about the systematics, which would be needed to construct the final ring with the necessary precision in proton EDM measurement. Since the ring is designated to be a proof of principle experiment, it is designed to be as inexpensive as possible while consistent with being capable of achieving its goals.

The ring will be smaller than most synchrotrons with a circumference of around 100m. The ring will feature the presence of simultaneous electric and magnetic fields for bending, which would allow for higher energy particles to be confined within a smaller ring.

In addition to this the ring will be optimized to run in two modes: a combined mode where particles of 239 or 294 MeV are stored in frozen spin mode, and an all-electric mode where horizontally precessing particles of 239 MeV are stored. The all-electric mode will have the capability of storing counter-rotating beams simultaneously. The specific beam parameters with respect to these configurations are listed in Table 2. The figure below shows the basic layout of the prototype EDM ring.

Table 2: A table listing the Basic beam parameters for the prototype ring. [8]

	E only	E & B, frozen spin		Unit
Bending radius	8.86	8.86	8.86	m
Kinetic energy	30	30	45	MeV
$\beta = v/c$	0.247	0.247	0.299	
γ (kinetic)	1.032	1.032	1.048	
Momentum	239	239	294	MeV/c
Electric field E	6.67	4.56	7.00	MV/m
Magnetic field B		0.0285	0.0327	T
r.m.s. emittances $\epsilon_x = \epsilon_y$	1	1	1	π mm mrad
Transverse acceptance $a_x = a_y$	>10	>10	>10	π mm mrad

3.2.2.1 Ring design and tuning

The prototype ring is in the shape of a squared ring with a fourfold symmetry. It features two families of quadrupoles labelled QF and QD, as well as an additional optional family named QSS at the centre of the long straight sections. This gives the storage ring access to a range of betatron tunes from 1 to 2 for Q_x and from 0.1 to 1.6 for Q_y. With optical flexibility being one of the key design features of this ring, the lattice can be adjusted for ultra-weak to moderate focussing.

This way the ring can either be adjusted to have a long beam lifetime with strong focussing, or the lowest possible radial magnetic fields with ultra-weak vertical focusing.

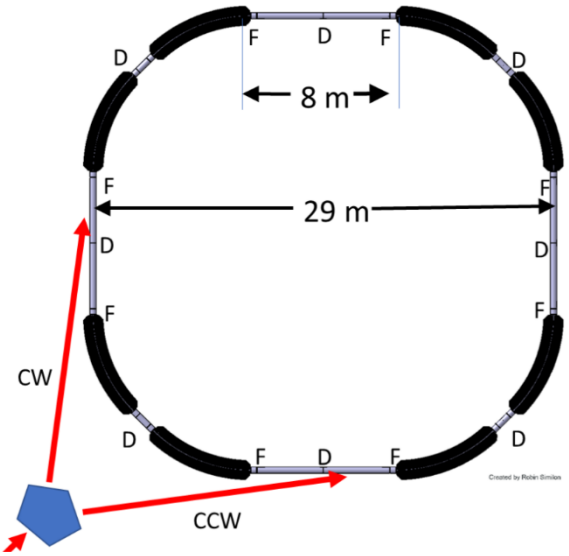

Figure 25: Basic layout of the prototype ring, consisting of eight dual superimposed electric and magnetic bends and two families of quadrupoles (F, focusing; D, defocusing), with an optional skew quadrupole family at the midpoints. [8]

3.2.2.2 *Beam injection*

Beam injection into the prototype EDM storage ring can take place through two injection channels either one at a time or simultaneously. Injector will provide an already bunched and polarized beam, either polarized longitudinally for the measurement, or vertically for running diagnostics. This injected beam will be protons already in the target energy range in a cooled phase space of 1 $\pi\, mm \cdot mrad$, in a beam that is bunched into 2, 4, 6 or 8 bunches. These bunches would be distributed into the clockwise and counterclockwise injection channels using switching magnets.

3.2.2.3 *Electric bends*

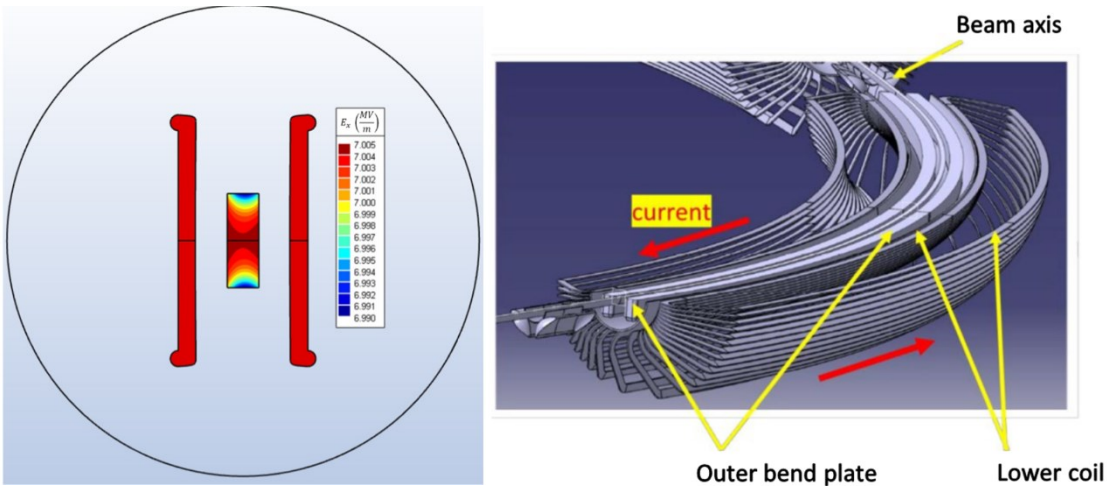

Figure 26: Left: Cross-section of the capacitor (in red) inside the beam tube (outer circle). Right: One-quarter of the combined electric and magnetic prototype ring. Two $\cos\theta$ iron-free dipoles surround the beam tube, in which the capacitor plates are accommodated. [8]

The electrostatic deflectors used to provide the radial electric field in the prototype storage string consist of two parallel metal plates held at equal and opposite electric potentials. The reference path of the particle would therefore lie on the contour of 0 potential. To be able to confine particles in the desired momenta and modes, the electrostatic deflectors need to provide electric field ranging from 5 to 10 MV/m. This means that even if the gap between the deflectors is about 60 mm, which is much less than the electrostatic deflectors currently used in accelerators, they would have to be connected to High voltage power supplies upwards of 300 kV. Since this would be a relatively new application, studies on the areas of field breakdown, dark current, electrode surface and conditioning on flat electrostatic plates are currently ongoing.

3.2.2.4 *Magnetic bends*

The prototype storage ring is designed to facilitate the suppression of systematic errors through symmetry. Thus, the magnetic coils used to produce the field are iron free to allow for quick and efficient field reversals.

3.2.3 Final experiment stage: pure-electric storage ring

The all-electric ring would be the final stage of the JEDI collaboration's EDM experiment, which would be designed to reach the target precision of $10^{-29} e \cdot cm$. It is a storage ring that will use only electric fields for particle confinement and measure the EDM using the strategy described in section 3.1.3. It will also be the first storage ring to have simultaneously counter-rotating proton beams in frozen spin state. Similar to the prototype ring, a series of bunches entering the ring in the same direction of travel will also be alternately polarised (one bunch facing forwards while the next faces backwards), which would be important for the cancellation of the geometric errors at the polarimeter [8].

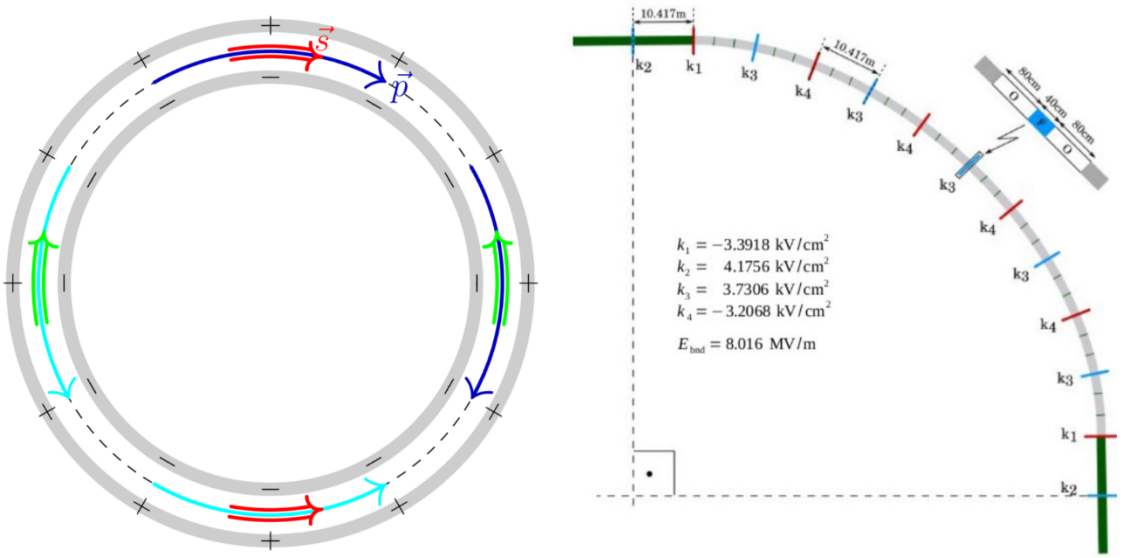

Figure 27: Left: Electric storage ring with simultaneously clockwise and counterclockwise circulating beams (dark and light blue arrows), each with two helicity states (green and red arrows for each beam). The grey circles represent electric field plates.
Right: One quadrant of a full-scale, all-electric, frozen-spin EDM storage ring. The straight sections are marked in green whereas the bending sections are marked in grey. The ticks on the beamline mark the electric quadrupoles whose field strengths are mentioned. The blue ticks are focussing quadrupoles while the red ones are defocussing. [8]

The design was first proposed by the SREDM collaboration at Brookhaven national lab [5], then later analysed for or possible sources of systematic errors by [56]. The current consensus on the design is of a ring with a total circumference of 500 m capable of holding up to 100 bunches of protons at a momentum of around 700 MeV. The electrostatic deflectors used for particle confinement will have a field of

8.016 MV/m, within a deflector gap of 3 cm. A general scheme of the storage ring is shown in Figure 27 (left).

In addition to an all-electric bend, the Ring will also feature electrostatic quadrupoles, to minimize the possibility of a stray magnetic field in the ring. The specific arrangement of these quadrupoles is shown in Figure 27 (right).

The all-electric ring in many ways is a scaled-up version of the prototype storage ring, which means they have many systematic features in common. Therefore, the key areas where more investigation is required, such as simultaneous rotating beam operation, the beam current limit, the sparking cost for electric bends, and regenerative breakdown; can be addressed by conducting experiments at the prototype storage ring.

3.2.3.1 Statistical sensitivity and sources of systematic errors

A system designed to definitively measure an EDM with a sensitivity of the order of $10^{-29}\, e \cdot cm$ would also be extremely sensitive to systematic errors which can drastically impact the overall precision of measurement. Therefore, suppressing these errors down to this level is probably the most challenging aspect of the design of the experiment [56].

The statistical error incurred over one single machine cycle was estimated to be:

$$\sigma_{stat} \approx \frac{2\hbar}{\sqrt{Nf}\tau PAE} \qquad \{ 170 \}$$

Table 3 lists the quantities represented, and the values for the relevant parameters in statistical error reduction for the Proton EDM experiment that are optimized for maximum feasibility, and the achievement of the target sensitivity for EDM precision in a one-year operation:

Table 3: The list of parameters mentioned in { 170 } which are relevant for the statistical error in the proton experiment. [8]

Beam intensity	$N = 4 \times 10^{10}$ per fill
Polarization	$P = 0.8$
Spin coherence time	$\tau = 1000\,\mathrm{s}$
Electric fields	$E = 8\,\mathrm{MV/m}$
Polarimeter analysing power	$A = 0.6$
Polarimeter efficiency	$f = 0.005$

$$\sigma_{stat}(1\ year) \approx 4.6 \times 10^{-29} e \cdot cm \qquad \{ 171 \}$$

While Table 3 serves as an effective guide as to what needs to be achieved given idealistic conditions, there are several sources of systematic errors that need to be considered [56], which have also been examined in the feasibility study [8]. These are discussed here.

3.2.3.1.1 False EDM signals due to stray fields

Sensitivity of the area measurement can be easily compromised by any phenomenon other than an EDM which generates a vertical component of the spin at the polarimeter. For instance, such an effect may be caused by unwanted electric fields due to bending or focussing device imperfections, or by stray magnetic fields inside the beam line or RF cavity.

3.2.3.1.2 Gravity

The influence of gravity on the beam dynamics is quite negligible, so much so that the effect of the beam "falling" is accounted for in the initial calibration of the electrostatic deflectors. However, the small vertical component of the electric field that must be keeping the beam from falling is perceived as a radial magnetic field in the rest frame of the particle. The eventual interaction of the magnetic dipole moment with this effective radial field creates a false EDM signal.

3.2.3.1.3 Radial magnetic fields

A largely dominating systematic effect is an average static radial magnetic field existing in the whole ring. This is a concern because even if such a field is as small as $10^{-17}T$, it can generate the same vertical spin precession as would an EDM of $10^{-29}e \cdot cm$.

Systematic errors such as stray electric fields, gravitational fields, and many others can be eliminated by running simultaneous clockwise and counterclockwise beams, which is one of the capabilities of a pure electric storage ring. A counter-rotating beam within the same beamline would essentially emulate a time reversed version of the same beam. This would mean that in principle, any time-even effects (effects that are invariant under a time inversion) are cancelled out. To mitigate a radial magnetic field effect (which would be time-odd), the ring can be installed in an advanced magnetic shield that reduces residual effects at the nanotesla level [57].

Another way to mitigate systematic errors is by improving the spin coherence time, which effectively increases the time available for the signal to become statistically significant. It is due to this reason that long spin coherence is an important prerequisite for precision, which forms the basis for the motivation for this study.

4. The Precursor Experiments at COSY

The precursor experiments are a series of experiments performed at the cooler synchrotron COSY to lay the groundwork for future experiments at more precise storage rings which are dedicated for the task of measuring proton EDM.

As described in previous chapters as well as extensively in the feasibility study [8], these experiments function as a series of proof of capability tests, centring around the primary goal of measuring the EDM of deuterons using COSY.

In a pure magnetic ring like COSY, it is possible to achieve a much higher precision in the measurement of the deuteron EDM as compared to the proton. This is owed to the fact that the deuteron has a lower gyromagnetic anomaly than the proton, which can improve precision in the invariant spin axis measurement as well as the spin coherence time.

The following sections will briefly run through the specifics of the precursor experiment, some preliminary results and a summary of the insights gained for the next stage of the experiment.

4.1 Spin Coherence Time Study

As discussed in the earlier section, every technique of measuring the EDM of charge particles using spin precession requires the beam to have a long spin coherence time. This is also the case for the experiment to measure the EDM of deuterons using COSY, where the strategy described in this section is used.

The requirement of the spin coherence time to be above $1000\ s$ is imposed by the limits on the statistical error as calculator in section 3.2.3.1. With this as a goal a study was conducted at COSY with a deuteron beam [58].

4.1.1 Experimental setup

Deuterons at an energy of about $970\ MeV$ were injected into the synchrotron in the form of polarized bunches with the initial polarization along the vertical axis.

These polarization axes were then rotated onto the horizontal plane by means of an RF solenoid. Once the horizontal polarization component vanishes, the particles would then begin to precess on the horizontal plane, at a frequency that was known and optimized in a previous analysis. An event time marking system recently implemented at COSY made it possible to continuously track the in-plane precession. The polarization was measured using a polarimeter which used a $17mm$ thick carbon block located 3 mm above the beam centre line. A small sample of the beam was extracted using electric field white noise onto the carbon block, which scatters the sample. The scattered particles were then detected by the EDDA scintillation detectors [59] [60], which measures the spatial asymmetry which indicates the initial polarization upon impact with the target. The polarimeter events were tagged with a clock time, which allowed the tracking of the precession history.

4.1.2 Experimental Results

The in-plane precession tracking technique described above was used to track the magnitude of the "normalized polarisation", which was measured from the amplitude of the sine-curve-fit of the polarimeter data [46]. The resulting trends are plotted in Figure 28 for two different settings of the sextupoles.

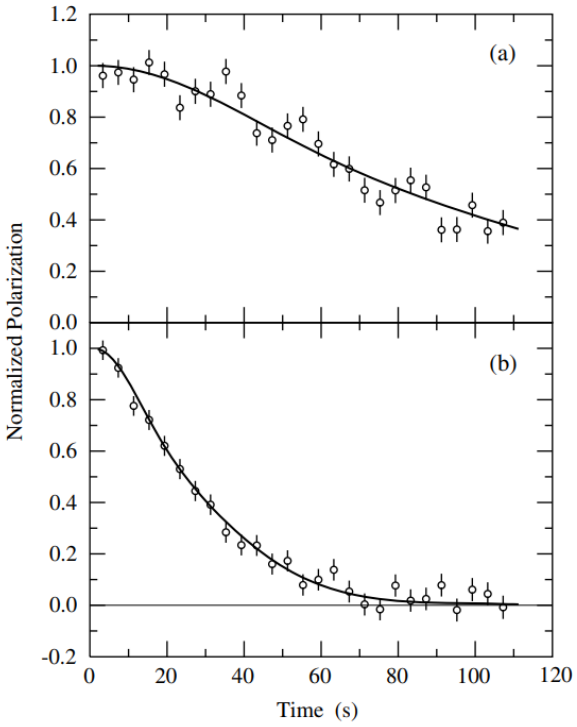

Figure 28: Measurements of the in-plane polarisation of the precessing bunch as a function of time. The scale is set so that the normalized polarization is unity at $t = 0$ s. The two panels represent two different sextupole field settings, resulting in polarization lifetimes, defined in [58] as the time for the normalized polarisation to reach 0.606, are 64.7 ± 5.4 s and 18.6 ± 2.6 s in (a) and (b), respectively. [58]

The study also set out to experimentally verify the pre-existing argument that the sextupole field setting of highest polarisation lifetime (spin coherence time) must coincide with zero effective chromaticity [61]. In other words, the spin coherence time is expected to be highest when the sextupoles exactly cancel out the natural chromaticity.

For the experiment, three families of sextupoles labelled MXS, MXL and MXG were used for second order beam corrections. The result of the study [58], as well as an extensive analysis [46] on the same have concluded that the arguments made by [61] hold true in the case of deuterons at COSY. This is also demonstrated in Figure 29.

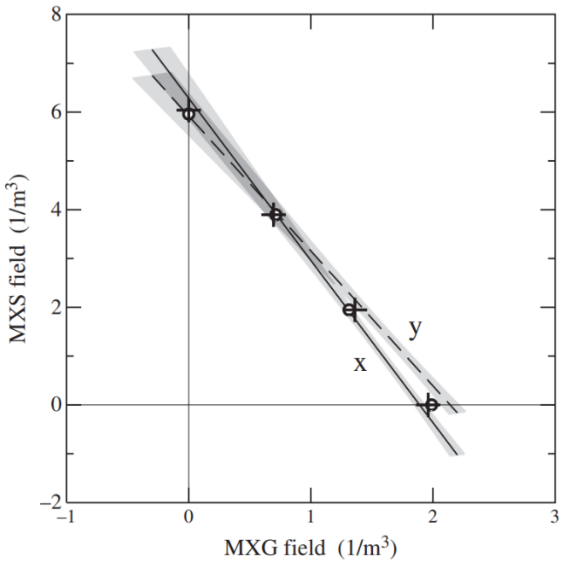

Figure 29: Two lines with error bands show the places where the x and y chromaticities were consistent with zero. The locations of the points of largest polarisation lifetime (spin coherence time) are shown by the circles and plusses. Circles indicate the results with a beam with high horizontal emittance, while the plus signs indicate those by a beam with a large longitudinal width. [46]

4.2 Deuteron EDM Measurement

The deuteron EDM experiment was essentially one that aimed at measuring the invariant spin axis of a deuteron as it precesses around the ring. This would be done by adopting the strategy discussed in section 3.1.1.

While in principle, such an experiment can directly provide a measurement of the EDM itself, the practical situation is somewhat more complex. This is because in a lattice like COSY with so many devices and a precisely focussed beam, the chances of magnetic field misalignments, among other systematic effects, are high, which can affect the orientation of the invariant spin axis. Due to this, the invariant spin axis may receive an offset in both the transverse and longitudinal directions. Thus, an accurate estimation of EDM from the measured invariant spin axis will require a careful investigation of the systematic effects through beam and spin tracking simulations [62]. That being said, the measurement of the invariant spin axis on its own, is an important proof of capability from the overall perspective of the EDM search.

4.2.1 Experimental Setup

The relevant beam parameters during the experiment are listed in Figure 30.

A vertically polarised deuteron beam is injected into the ring and accelerated to a momentum of $970\ MeV$, and cooled. The beam spins are then rotated onto the horizontal axis using a solenoidal field. This begins the horizontal precession around the invariant spin axis which was measured using a polarimeter. From the precession frequency the spin tune was calculated to be -0.16. the negative sign

indicates that the direction of precession of the spin is opposite to the direction of the revolution of the particle.

deuteron momentum	p	$0.970\,\mathrm{GeV/c}$
rel. velocity	β	0.459
Lorentz Factor	γ	1.126
gyromagnetic anomaly	G	≈ -0.143
revolution frequency	f_{cosy}	$752\,543\,\mathrm{Hz}$
precession frequency	$\lvert\vec{\Omega}^{\mathrm{MDM}}\rvert$	$121\,173\,\mathrm{Hz}$
cycle length		$270\,\mathrm{s}$
RF Wien Filter	f_{WF}	$872\,949\,\mathrm{Hz}$

Figure 30: Relevant parameters for the deuteron EDM experiment at COSY. [9]

4.2.2 Methodology

Were it not for the existence of an EDM, the invariance spin axis would be exactly parallel to the axis of the vertical magnetic field. The angle of tilt ζ_{EDM} caused by the EDM in the radial direction is given by:

$$\zeta_{EDM} = \tan^{-1}\left(\frac{\eta v}{2cG}\right) \qquad \{\ 172\ \}$$

However as mentioned earlier, the presence of field misalignments could also offset the invariant spin axis both in the radial as well as the longitudinal direction. Therefore apart from the RF Wien filter, a solenoid (known as the "Siberian Snake") was also used to provide kicks along the procession but about a longitudinal axis. Therefore with a combination of kicks provided by both devices, the net result will be a polarisation buildup unless the vector sum of their angular impulses are perfectly aligned with the invariant spin axis.

$$\Delta\vec{L}\cdot\vec{\Omega} = \left(\Delta\vec{L}_{RF} + \Delta\vec{L}_{sol}\right)\cdot\vec{\Omega} = 0 \qquad \{\ 173\ \}$$

The figure shows the effect of turning on the RF Wien filter and the Siberian snake. Apart from the Wien filter rotation angle ϕ^{WF} and the angular displacement ξ^{sol} on the spin due to the solenoid, the rate of polarisation buildup would also depend on the relative phase ϕ_{rel} of the Wien filter field oscillations (assumed to be 0 in { 163 }):

$$\begin{aligned} E_W &= E_{W_0}\cos(\Omega t + \phi_{rel}) \\ B_W &= B_{W_0}\cos(\Omega t + \phi_{rel}) \end{aligned} \qquad \{\ 174\ \}$$

The variation of the normalised build-up rate with this relative phase is shown in Figure 32.

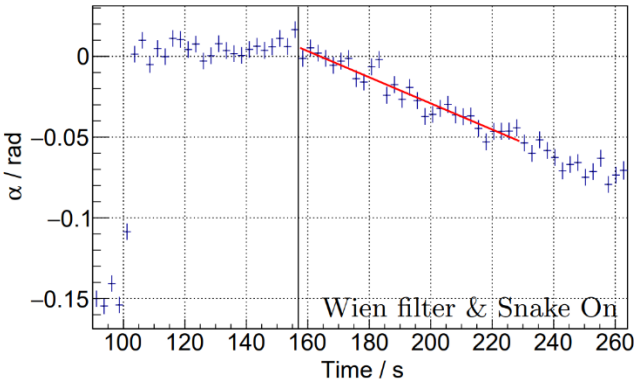

Figure 31: The angle α of the polarisation vector with the horizontal (ring) plane, as a function of time. At $t = 100\ s$, the vertically polarised beam is rotated onto the horizontal plane. At $t = 155\ s$, the RF Wien filter and the Siberian Snake are turned on and the vertical polarisation begins to linearly build up. In this measurement, the settings were $\phi^{WF} = 0.945\ mrad$, $\xi^{sol} = 0\ rad$, $\phi_{rel} = 0.79\ rad$. [9]

Operating at the relative phase where the the polarisation build-up is maximum would make the situation exactly the same as the one described in section 3.1.1. The rate of build up at this point is known as the resonance strength ϵ.

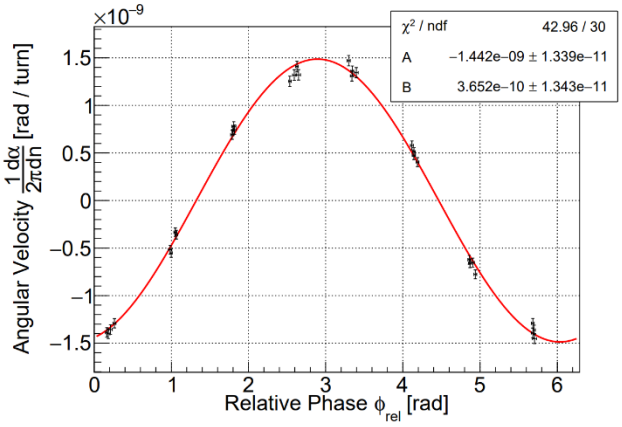

Figure 32: A plot showing the dependence of the rate of the vertical polarisation build-up calculated from the linear fit of Figure 31 with the relative phase ϕ_{rel} of the RF Wien filter. The points were fitted with a sinusoidal model $\frac{1}{2\pi}\frac{d\alpha}{dn} = A\sin\phi_{rel} + B\cos\phi_{rel}$. The amplitude of the function $\epsilon = \sqrt{A^2 + B^2}$ is the resonance strength. [9]

4.2.3 Experimental results

The resonant strengths at various values of and are plotted in the Figure 33 [9]. These points were fitted using the theoretical description of the resonance strength described in [63]:

$$\epsilon\left(\phi^{WF}, \xi^{sol}\right) = \left({A_{WF}}^2 (\phi^{WF} - \phi_0^{WF})^2 + \frac{{A_{sol}}^2}{4\sin^2(\pi\nu_s)} \left(\xi^{sol} - \xi_0^{sol}\right)^2 \right)^{1/2} \qquad \{\ 175\ \}$$

Here, A_{WF} and A_{sol} are free scaling factors and ϕ_0^{WF} and ξ_0^{sol} are the minima location to be determined from the fit. With this description and several measurement points, the minima of the distribution was found, which gives the estimation of the invariant spin axis:

$$\phi_0^{WF} = -2.91(8)\ mrad$$
$$\xi_0^{sol} = -5.22(7)\ mrad \qquad \{\ 176\ \}$$

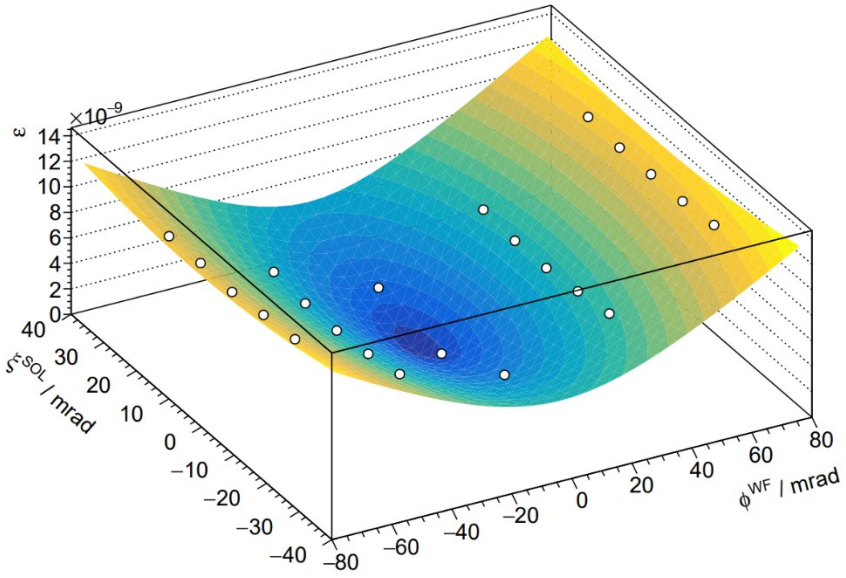

Figure 33: Resonance strength ϵ , plotted against the Wien filter rotation angle ϕ^{WF} and the angular displacement of the spin due to the Siberian snake ξ^{sol}. The points are fitted with the function { 175 }, and the minima of the surface gives the orientation of the invariant spin axis. [9]

While the fact remains that without a rigorous model of the field misalignments from simulations, the estimation of EDM from these numbers would be highly inaccurate; the study does comment on the measurement sensitivity that a tilt of $1\ mrad$ in the radial direction is equivalent to an EDM of $10^{-17} e \cdot cm$.

5. Simulations of the Prototype Storage Ring

With the results of the precursor experiment being able to provide many insights on the systematics required for EDM searches, the next stage of the experiment can be initiated. The prototype storage ring is the experiment which forms the primary focus of this thesis. Since this ring is still in the developmental stages at the moment [8], simulations were performed on an idealized lattice based on the most up-to-date design as of the beginning of this work. This design has been reviewed by the JEDI collaboration in detail in their latest feasibility study.

In this chapter, the specifics on the simulations of spin decoherence and the optimization methods employed to maximize it shall be presented. The first section mentions details about the software used for the simulation, the reasons for choosing it and some of the studies and ongoing experiments used to benchmark it. The next section talks about the lattice structure, how the field settings are adjusted, and the choice of operation modes explored for the decoherence study. Once the orbit is closed, the subsequent sections discuss how the remaining lattice parameters that affect spin coherence time are organized and systematically searched for initial collection of data on decoherence patterns. These include also the specific quantities recorded among the beam and spin parameters as well as models used to derive key measurements from them. The next sections after that deal with the interpretation of the initial data and their modelling to make predictions. The final section then discusses how the optimizer is used to obtain the field settings which maximize spin coherence time.

5.1 BMAD

To perform simulations of beam and spin tracking around a specific arrangement of devices (a "lattice"), a software library named BMAD was chosen to devise accurate transfer parameters and handle the calculations.

BMAD [64] is a subroutine library (or a library of scripts and functions) for relativistic charged–particle and X-Ray simulations in accelerators and storage rings. BMAD has been developed at Cornell University's Laboratory for Elementary Particle Physics and has been in use since 1996.

BMAD has routines for calculating transfer matrices, emittances, Twiss parameters, dispersion, coupling, etc. The elements that BMAD knows about include quadrupoles, RF cavities (both storage ring and LINAC accelerating types), solenoids, dipole bends, Bragg crystals etc. Elements can also be defined to control the attributes of other elements, allowing for the creation of composite devices. In addition, BMAD has various tracking algorithms including Runge-Kutta and symplectic (Lie algebraic) integration.

The BMAD subroutine library uses an object-oriented approach and is (currently) written in Fortran 2008.

5.2 The Prototype Lattice "V3"

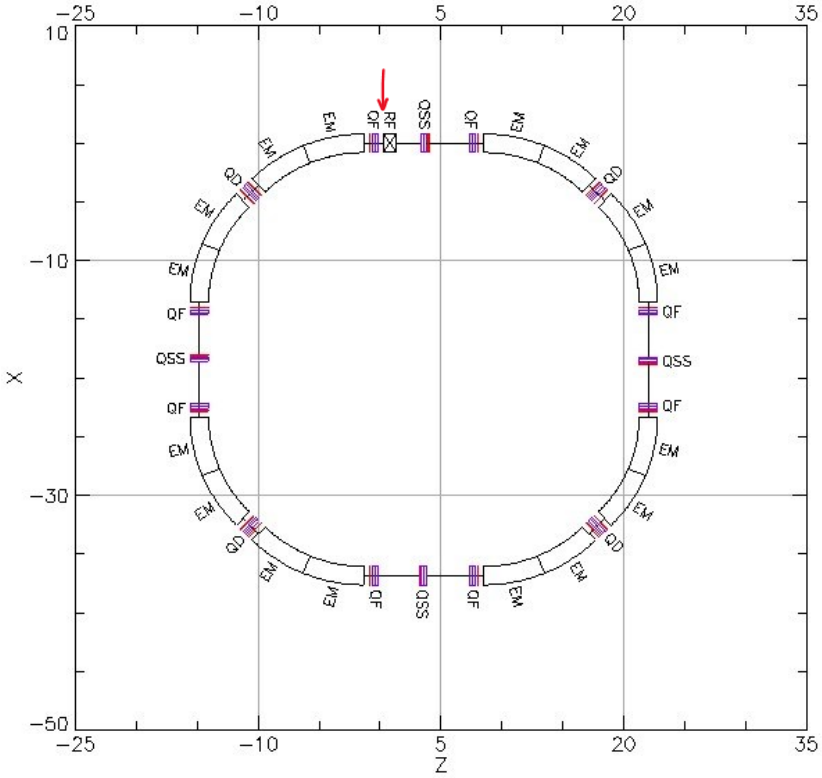

Figure 34: A floor plan of the V3 prototype lattice, generated by Tao [66]. The devices marked EM are the electromagnetic bends, QF, QD, and QSS are the quadrupoles of the three different families, and RF is the RF cavity. The red arrow points to the spot on the beamline that is considered the origin of the laboratory coordinate system used in the plot ($X = 0$, $Z = 0$). This point corresponds to $s = 0$ in the Frenet frame.

The prototype lattice V3 is the BMAD description and representation of the prototype storage ring design as conceptualised by [65] and also described in the feasibility study [8]. Once described, the BMAD user program "Tao" [66] can be

used to visualise and diagnose the lattice. The figure shows a floor plan as generated by Tao.

5.2.1 Dipole magnet settings

As can be seen from Figure 34, the prototype lattice has eight electromagnetic bends, each of which carry out a 45-degree turn of the particles at a given radius of curvature. A "lattice" in BMAD is characterised by the particle path being closed. In other words, the fields must be adjusted in accordance with the particles energy such that it always stays on the beam path. Given this constraint the dipole settings of the lattice are simply characterised by two parameters: the particle momentum and the length of the electromagnetic bends. Figure 35 shows a part of the lattice file where the dipole fields are described.

```
1  !-------------------------------------------------------------------------!
2  !                                                                         !
3  !              BMAD PROTOTYPE LATTICE VERSION 3.0                         !
4  !                                                                         !
5  !-------------------------------------------------------------------------!
6
7  N.Ebend         =   16
8
9  l.Ebend         =   4.809875
10 l.Quad          =   0.200
11 l.DQ            =   0.200
12 l.DQS           =   0.120
13 l.DS            =   1.600
14 l.DRF           =   0.300
15 l.BPM           =   0.080
16 l.DEM           =   0.420
17
18 k.focus         =   -0.0329
19 k.defocus       =   -0.16
20 k.straight      =   +0.000
21 k.sexf          =   -0.0001
22 k.sexd          =   +0.0001
23 k.sexs          =   +0.000
24
25 !-------------------------------------------------------------------------!
26
27 momentum    =   294.057e6
28 angle       =   2*pi/(N.Ebend)
29 energy      =   sqrt(momentum*momentum+m_proton*m_proton)
30 gamma       =   energy/m_proton
31 beta        =   momentum/energy
32 G           =   anom_moment_proton
33 r           =   l.Ebend/angle
34
35 bfield      =   angle*momentum/(c_light*l.Ebend)
36 efield      =   gamma*m_proton*beta*beta / (r*((1/(gamma*gamma-1)-G)*(beta*beta/G)+1))
37 bfield_err  =   bfield - efield/(beta*c_light)
38
39 !-------------------------------------------------------------------------!
```

Figure 35: A snippet from the BMAD file description of the V3 lattice. The length of the EM bends and the particle momentum are set in lines 9 and 26 respectively. Line 35 sets the "default" magnetic field required to close the path. The actual magnetic field is set in line 37, and the electric field required for satisfying the frozen spin condition (see { 164 }) is calculated in line 36. The quadrupole field strengths are set in lines 18, 19 and 20, while the sextupole field strengths are set in lines 21, 22 and 23.

Since both electric and magnetic fields are present in the bends, one additional parameter that needs to be set is the ratio of E to B. However, since this study focuses on simulations in the frozen spin condition, this parameter, together with the particle momentum, are also constrained to fulfil this requirement.

The frozen-spin condition is defined by the situation where the reference particle in the storage ring has a spin tune of zero. When this is applied to the expression in { 139 }, one can deduce the value of the normalized field ratio $r = {}^{E}/_{cB}$ for the proton:

$$\nu_s = \gamma G - \frac{r(G+1)}{\gamma(\beta + r)} = 0 \quad \Rightarrow \quad r = \frac{\beta\gamma^2 G}{1 - \beta^2\gamma^2 G} = 0.7147 \qquad \{ 177 \}$$

The end result is a single degree of freedom as described in the bending radius contour in Figure 36. The study [65] prescribes two points or "modes" for investigation as also shown in Table 2. In this thesis, simulations were conducted on the 295 MeV mode.

5.2.2 Quadrupole and sextupole magnet settings

As can be seen in the Figure 34, the lattice has three families of quadrupoles labelled QF, QD and QSS just like the prototype design. In addition, there are also three corresponding families of sextupoles named SXF, SXD and SXSS. However, this being an idealised lattice meant to develop a preliminary understanding of frozen spin dynamics, the sextupole fields used in this lattice are superimposed on the quadrupole fields for simplicity and ease of simulation. The field strengths κ_F, κ_D and κ_{SS} of the quadrupoles and χ_F, χ_D and χ_{SS} of the sextupoles are the parameters that remain to be set according to the desired qualities of the particle beam and spin during storage. In this thesis, these are the settings that are eventually optimised for maximising spin coherence time.

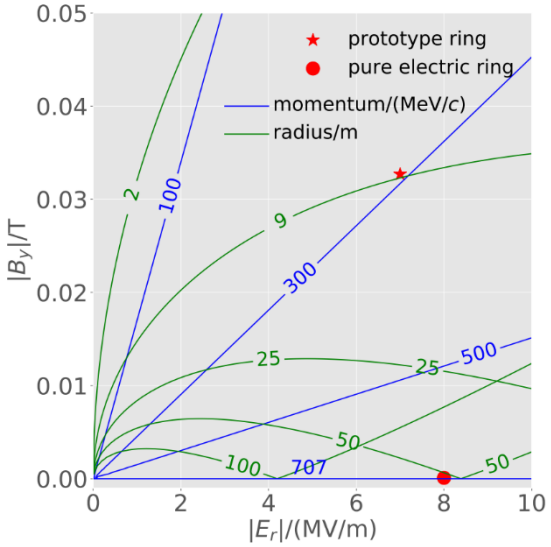

Figure 36: Bending radius (green curves) and particle momentum (blue lines) contours plotted as a function of electric and magnetic fields. The red star plots the configuration of the prototype ring (currently investigated in this thesis) and the red circle plots that of the all-electric ring (described in section 3.2.3) [83]

5.3 Measurement of Twiss Parameters

The Twiss parameters of the lattice can be measured directly via a dedicated routine in BMAD. These include the Courant-Snyder parameters α, β and γ (see section 2.3.1), as well as the dispersion function (see section 2.3.2).

The values and variation of these parameters depend on the quadrupole settings. However, at reasonably low field strengths, sextupole fields do not affect the Twiss parameters. Figure 37 shows the distributions of the Twiss parameters across the lattice at a quadrupole setting that satisfies the stability conditions.

The point $s = 0$ in Figure 37 is a point shortly before the RF cavity (see the red arrow in Figure 34). It can be seen that the focussing quadrupole effect restricts the beta function's evolution along each transverse axis. The higher the beta function, the stronger the focusing effect. Also observable, is the fact that the quadrupoles that focus (bend towards the s-axis) along one transverse direction simultaneously defocus (bend away from the s-axis) along the other.

The dispersion function is high in the long straight section due to the effects of the bends. The bend after a straight section tends to recombine the beam and the bend before tends to disperse it.

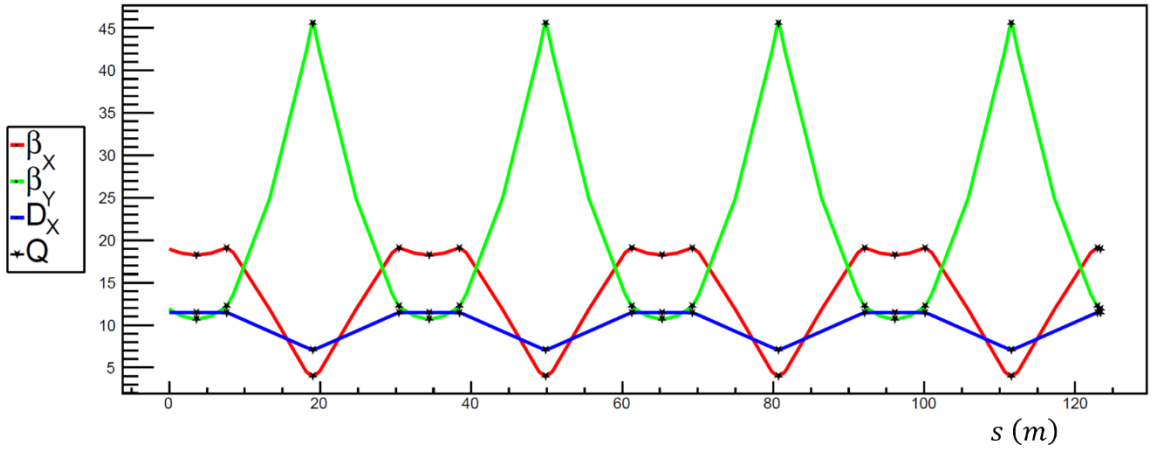

Figure 37: Twiss parameters measured at quadrupole settings given by $\kappa_F = 0.077$ and $\kappa_D = -0.242$. The straight-section quadrupole is currently turned off. The red, green, and blue curves represent the horizontal beta function, vertical beta function and the horizontal dispersion function respectively as functions of the distance s along the ring. The points marked by stars are the locations of quadrupoles (also the superimposed sextupoles). All units are in metres.

5.4 Parameter Space

With the momentum of the particles fixed and the reference path being closed, it is now possible to assess the optical parameters of the lattice.

5.4.1 First-order optical parameters

5.4.1.1 Transverse motion

As demonstrated in the previous section, in BMAD, it is possible to characterise any given lattice on the basis of the Courant-Snyder parameterization. This means that the optical functions can be directly acquired from BMAD closed orbit calculations, provided that there exists a real solution to the Hill's differential equation at that setting. Imaginary or complex solutions as discussed in section 2.3.1.2, occurs when a combination of quadrupole fields lead to a net defocusing effect along a transverse axis.

So, a scan was done across all quadrupole configurations of the lattice to find those which have real solutions to the HDE, and thus real betatron tunes, in both transverse directions. A configuration with a pair of real betatron tunes is known as a working point. The results of the scan are depicted in Figure 38.

The results of the scan are consistent with previous simulations of this lattice. In [65],1D scans of the betatron tunes were performed while keeping two sextupoles fixed and varying a third (κ_F or κ_D), which show the same behaviour. A finer 2D scan was done in [67] which also is reflected in these results.

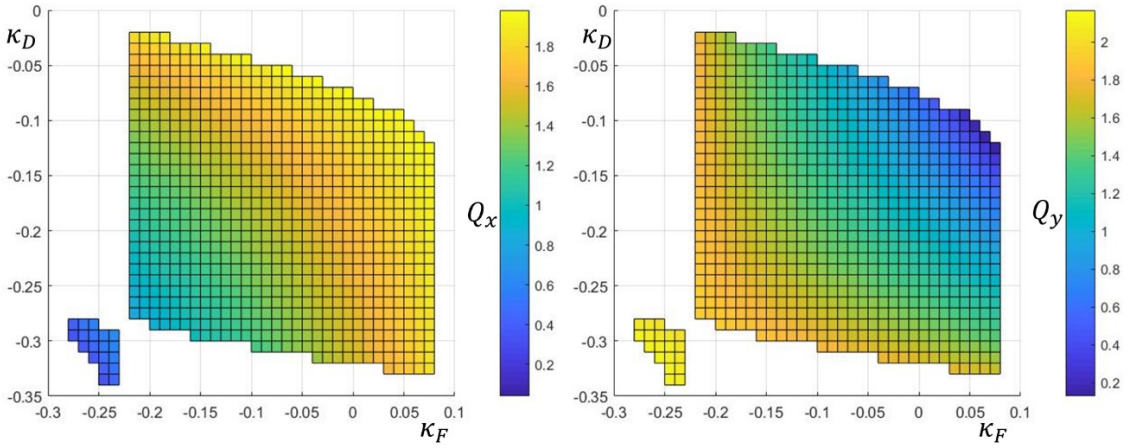

Figure 38: A scan of all possible working points. The area covered by the colours are the regions with real values of betatron tunes. The colour-bar on the left plot shows the horizontal betatron tune, and the one on the right shows the vertical betatron tune.

It was also seen in [65] that when κ_{SS} was varied while keeping κ_F and κ_D fixed, very little change in the tunes were observed per unit change in the field strength. This is likely because of the placement of the quadrupole in a straight section and in close proximity (very little phase advance) between two others of the same family (see Figure 34). Therefore, in the simulations performed in this thesis, in order to avoid non-linear behaviour as much as possible, all tunes were accessed with the straight section quadrupole kept off.

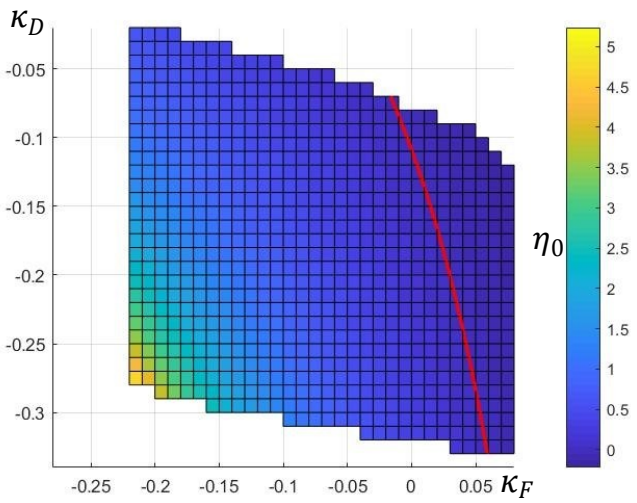

Figure 39: A scan of the phase slip factor over all working points on the lattice. The red curve represents the gamma-transition line where $\eta_0 = 0$. Points to its right fulfil the stability condition of $\eta_0 < 0$.

5.4.1.2 Longitudinal motion

First-order longitudinal motion can be characterised by the first-order phase slip factor η_0, which is defined in { 91 }. This quantity also determines the synchrotron frequency ω_s expressed in { 105 }. A scan of the phase slip factor over all working points in the lattice is shown in Figure 39.

Since the storage ring currently functions in a non-acceleration mode with stationary RF buckets, the RF phase is set to zero. This means that the longitudinal phase stability is achieved only for points where the phase slip factor is negative (see { 110 } and section 2.4.2.2). These are the points to the right of the red curve in Figure 39.

5.4.2 Second-order optical parameters

The chromaticities ξ_x and ξ_y can be obtained from the closed orbit calculations of BMAD. However, in consideration of the result in section 2.6.5.3, an important quantity to track would be the second order momentum compaction factor α_1, as it directly influences the spin coherence time.

Due to a dedicated routine for calculation of second-order momentum compaction not being available in BMAD, a customized measurement process was used to estimate it through the tracking of the z coordinate of a single (otherwise) reference particle with a longitudinal momentum offset δ, and the RF cavity turned off. With a simulation of several turns, Δz is obtained, which is the gain in the particle's z per turn. In BMAD, $z(n, s)$ during the n^{th} turn at the location s is calculated by [64]:

$$z(s) = -v^*(s)\big(t^*(s) - t(s)\big) \qquad \{ 178 \}$$

Here, $v^*(s)$ is the velocity of the offset particle, $t^*(s)$ is the time at which the particle was at s, and $t(s)$ is the time at which the reference particle was at s. With a fixed momentum offset and no bunching, v^* is constant and z builds up linearly. A fit allows the measurement of $\Delta z(s)$:

$$\Delta z = z(s) - z(s-L) = -v\big(t^*(s) - t(s) - t^*(s-L) + t(s-L)\big) = -v\Delta t \qquad \{ 179 \}$$

Here, Δt represents the difference in the times taken by the offset and the reference particles to travel one turn. This would hold the same meaning as the Δt in { 91 }.

The change in path length, without performing the first order approximation, is given by:

$$\frac{\Delta L}{L} = \frac{\Delta v}{v} + \left(1 + \frac{\Delta v}{v}\right)\frac{\Delta t}{t} = \frac{\Delta v}{v} + \left(\frac{1}{v + \Delta v}\right)\left(\frac{v + \Delta v}{v}\right)\frac{\Delta z}{t} = \frac{\Delta v}{v} - \frac{\Delta z}{L} \qquad \{ 180 \}$$

Considering up to the second order in δ, the velocity offset can be written as:

$$\frac{\Delta v}{v} = \frac{\delta}{\gamma^2} - \frac{3v^2\delta^2}{2\gamma^2 c^2} + \cdots \qquad \{ 181 \}$$

Thus, the change in path length can be measured by:

$$\frac{\Delta L}{L} = \frac{\delta}{\gamma^2} - \frac{3v^2\delta^2}{2\gamma^2 c^2} - \frac{\Delta z}{L} = \alpha_0\delta + \alpha_1\delta^2 + \cdots \qquad \{ 182 \}$$

The change in path length can be plotted as a function of momentum offset to obtain a distribution which can be fitted by a polynomial of second order to estimate the momentum compaction factors.

The chromaticities and the second-order momentum compaction factor together make up the second-order optical parameters. While these parameters are affected by the quadrupole settings κ_F and κ_D, changes to the sextupole field strengths χ_F, χ_D and χ_{SS} would affect only the second-order parameters while leaving the first order ones intact. For a given working point, each of these parameters was found to vary linearly with the sextupole settings, which is representative of the result of { 84 }, and the direct contribution of sextupole fields to the second-order dispersion [68]. A linear variation of chromaticities with sextupole fields was also observed in COSY [46].

In fact, simulations on the current lattice show that the second order parameters can each be modelled as a fixed potential in χ-space with a constant gradient:

$$\vec{\nabla}_\chi \xi_x = \vec{a}_F \quad \vec{\nabla}_\chi \xi_y = \vec{a}_D \quad \vec{\nabla}_\chi \xi_x = \vec{a}_{SS} \qquad \{ 183 \}$$

Here, $\vec{a}_F$, $\vec{a}_D$ and $\vec{a}_{SS}$ are constant vectors in the χ-space with a basis formed by the unit-vectors $\hat{\chi}_F$, $\hat{\chi}_D$ and $\hat{\chi}_{SS}$. The gradient operator is given by:

$$\vec{\nabla}_\chi = \frac{\partial}{\partial \chi_F}\hat{\chi}_F + \frac{\partial}{\partial \chi_D}\hat{\chi}_D + \frac{\partial}{\partial \chi_{SS}}\hat{\chi}_{SS} \qquad \{ 184 \}$$

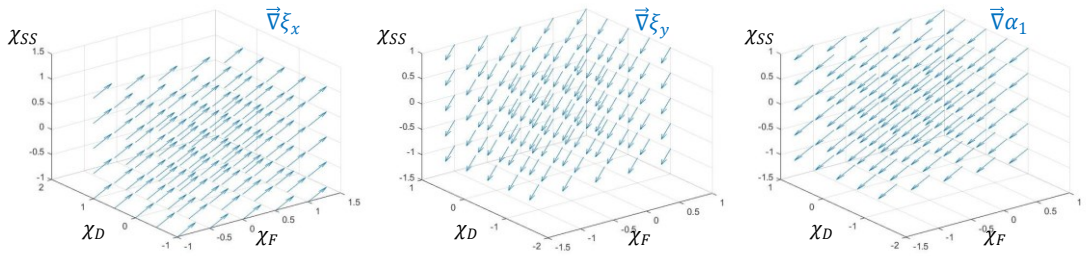

Figure 40: Vector-field plots of the gradients of the second-order parameters in the sextupole field space at a working point with $\kappa_F = 0.062$ and $\kappa_D = -0.165$. The length and direction of each arrow in the three plots represents the magnitude and direction of the gradient of the quantities ξ_x (left), ξ_y (centre) and α_1 (right). The arrows within a plot having a common magnitude and direction is indicative of a constant gradient across space.

Figure 40 demonstrates the invariance of the gradients of the second-order parameters measured at a given working point. The second-order parameters at a given sextupole field configuration can thus be expressed as:

$$\vec{\xi}(\vec{\chi}) = \vec{\xi}(\vec{0}) + \boldsymbol{C}\vec{\chi} \qquad \{ 185 \}$$

5.4.3 Structure and organization of parameters

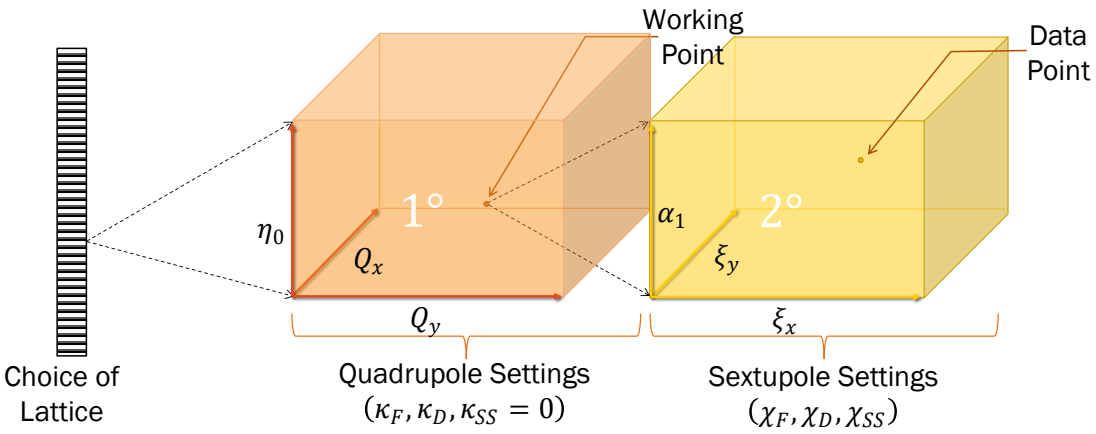

Figure 41: The organization of the parameter space explored in this study. The space formed by the betatron tunes Q_x, Q_y and the phase slip factor η_0 is the first-order (1°) space, and the one formed by the chromaticities ξ_x, ξ_y and the second-order momentum compaction factor α_1 is the second-order (2°) space. A point in the first-order space is termed a working point, and one in the second-order space is termed a data point.

Here, $\vec{\xi} = \begin{pmatrix} \xi_x \\ \xi_y \\ \alpha_1 \end{pmatrix}$ represents the second-order optical parameters, $\overrightarrow{\xi_0} = \begin{pmatrix} \xi_{x_0} \\ \xi_{y_0} \\ \alpha_{1_0} \end{pmatrix}$ represents their "natural" values (i.e., the values when the sextupoles are turned off), and $\vec{\chi} = \begin{pmatrix} \chi_F \\ \chi_D \\ \chi_{SS} \end{pmatrix}$ represents the sextupole field strengths. The matrix $\boldsymbol{C}$ (known as

the C-matrix) represents the linear transformation from the field-strength space to the second-order optics space. The rows of the matrix are in order, the gradients $\vec{\nabla}_\chi \xi_x$, $\vec{\nabla}_\chi \xi_y$ and $\vec{\nabla}_\chi \alpha_1$. $\boldsymbol{C}$ is therefore constant and characteristic of a given working point.

The quadrupole field strengths κ_F and κ_D determine the first-order optical parameters: the betatron tunes Q_x, Q_y and the first order phase slip factor η_0. However, the mapping from the quadrupole fields to the first-order parameters is neither linear nor surjective (i.e., one set of optical properties may have more than one field setting that gives rise to it). Moreover, the mapping cannot be represented as a function since not every field setting is a "working point" that has a set of optics associated with it (e.g., it doesn't fulfil the stability criteria). Finally, there are working points which have well-defined tunes but are unstable due to resonance effects.

It is for these reasons that the lattice is explored through the optical parameters rather than the field settings themselves. This way, the relevant systematics are readily apparent. This also applies to the case of the second-order parameters despite having a linear and bijective mapping, since as discussed in section 2.6.5, the second-order optics have a direct influence on the spin coherence time.

Thus, the parameter space explored in the optimization of spin coherence time of this thesis is depicted in Figure 41.

5.4.4 Choice of first working point

The study [58] on spin coherence times at COSY concludes that highest spin coherence times should coincide with working points with lowest natural chromaticities. To test this hypothesis, the first working point examined in this study is the one with chromaticities as close to zero as possible. To find the field settings of this point, the natural chromaticities of all available working points were measured (shown in Figure 42) and the working point with both chromaticities as close to zero as possible was estimated from the contours (shown in Figure 43). The defining parameters and optical properties of this point is shown in Table 4.

Table 4: Field settings and optical properties of the zero-chromaticity working point.

κ_F	κ_D	Q_x	Q_y	ξ_{x_0}	ξ_{y_0}	α_{1_0}
0.0769	-0.2417	1.855	1.095	0.00	0.00	-0.2578

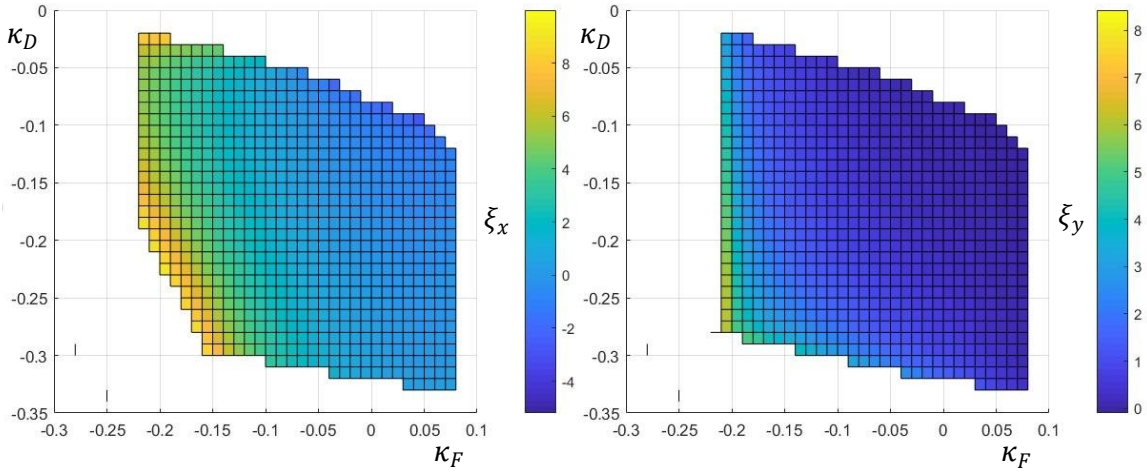

Figure 42: Natural chromaticities measured over all available working points where chromaticity measurement was possible.

5.4.5 C-matrix

The C-matrix, defined in section 5.4.2, was calculated by measuring the chromaticities and 2° momentum compaction factors at a grid of sextupole settings, and fitting the data to the model described in { 84 }.

The C-matrix and its inverse were found to be:

$$\boldsymbol{C} = \begin{pmatrix} 55.64 & 3.657 & 26.72 \\ -35.76 & -41.15 & -15.67 \\ -28.42 & -2.867 & -14.05 \end{pmatrix} \quad \{ 186 \}$$

$$\boldsymbol{C}^{-1} = \begin{pmatrix} 0.5403 & -0.0255 & 1.056 \\ -0.0585 & -0.0236 & -0.085 \\ -1.08 & 0.0564 & -2.1876 \end{pmatrix} \quad \{ 187 \}$$

$\boldsymbol{C}^{-1}$ can be used to calculate the sextupole field settings that give rise to a desired set of 2° optics. This way a custom range or "slice" of optics can be scanned to measure spin coherence time.

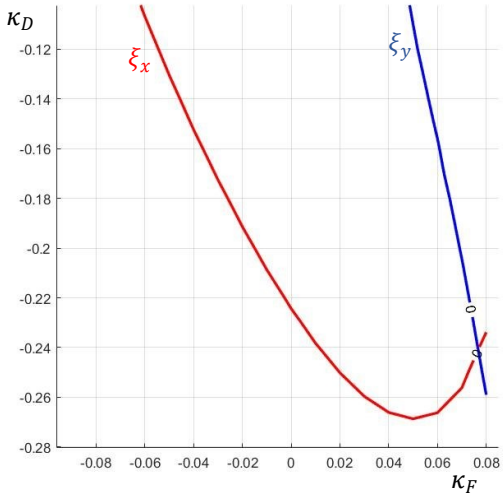

Figure 43: Contour curves for $\xi_x = 0$ (red) and $\xi_y = 0$ (blue) based on interpolations from the graphs in Figure 42. The intersection point gives the field settings of the working point with zero natural chromaticity.

5.5 Investigations of Spin Decoherence

As discussed in previous chapters, spin coherence time can be measured by tracking the magnitude of the polarisation vector. In particle tracking mode,

BMAD's spin tracking module tracks each individual particle's spin vector $\vec{\boldsymbol{s}}$. In beam tracking mode, the program returns the polarisation vector calculated according to { 145 }. While measurements of relevant beam parameters such as tunes, chromaticities and momentum compaction factors are done in particle tracking mode, simulations of spin physics during this study are always conducted in beam tracking mode.

5.5.1 Decoherence in frozen spin

The frozen spin condition requires the reference particle to have a net spin tune of zero. However, this is not necessarily the case with offset particles. From the BMT equation, it is clear that apart from extra fields (such as quadrupole or sextupole fields), the spin tune is affected by a velocity change. Here we consider the change in the spin tune up to the second order, with change in momentum. Expressing the relevant parameters as functions of the momentum, the following expressions are obtained:

$$\beta' = \frac{d\beta}{dp} = \frac{1}{m\gamma^3}, \quad \gamma' = \frac{d\gamma}{dp} = \frac{\beta}{m}, \quad \Delta\nu_s = \nu_s'\delta p + \frac{1}{2}\nu_s''(\delta p)^2 \qquad \{\ 188\ \}$$

This, when calculated under the condition $\nu_s = 0$, gives…

$$\begin{aligned}\Delta\nu_s = {} & \frac{\beta x(G+1)}{\gamma}\left(1 + \frac{1-x^2}{(\beta+x)^2}\right)\delta \\ & - \frac{\beta^3 x(G+1)}{2\gamma}\left(1 + \frac{1-x^2}{(\beta+x)^2} + \frac{2(1-x^2)}{\beta\gamma^2(\beta+x)^3}\right)\delta^2\end{aligned} \qquad \{\ 189\ \}$$

…which upon evaluation for the kinematic parameters of the prototype ring gives…

$$\Delta\nu_s = \zeta_0\delta + \zeta_1\delta^2 \qquad \{\ 190\ \}$$

…with $\zeta_0 \approx 0.8408$ and $\zeta_1 \approx -0.1104$. The direct verification of these numbers through simulations can be challenging considering that it would require simulations with all focussing magnets turned off. However, it would stand to reason that the expression holds true for modified values of the coefficients when corrected for the effects of the quadrupole and sextupole fields on the spin tune.

From single-particle simulations of the prototype lattice, it was observed that ζ_0 takes on a different value at each working point and ζ_1 takes on different values at each data point.

5.5.2 Beam Distribution

For this study, a beam distribution was generated using the in-built algorithms in BMAD, with each of the six phase space parameters assigned a random value picked from a zero-centred Gaussian distribution function. The Gaussian functions of the transverse phase space coordinates were assigned standard deviations based on the desired emittance of the half-maxima particles. The longitudinal phase space parameters were assigned directly from user input. A description of the beam is shown in Figure 44.

```
1  &beam_track_params
2    beam_init%species                  = 'proton'
3    beam_init%n_particle               = 1000
4    beam_init%n_bunch                  = 1
5    beam_init%distribution_type(1)     = 'RAN_GAUSS'
6    beam_init%distribution_type(2)     = 'RAN_GAUSS'
7    beam_init%distribution_type(3)     = 'RAN_GAUSS'
8    beam_init%a_emit                   = 5e-7
9    beam_init%b_emit                   = 5e-7
10   beam_init%sig_z                    = 1e-3
11   beam_init%sig_pz                   = 1e-4
12   beam_init%spin(1)                  = 0
13   beam_init%spin(2)                  = 0
14   beam_init%spin(3)                  = 1
15   nturn                              = 20000
16   savedir                            = 'exp'
17 /
18
```

Figure 44: A snippet from the beam distribution user input file. The type of distribution is defined for each of the spatial directions in lines 5, 6 and 7. The x and y emittances are set in lines 8 and 9, and the standard deviations of the longitudinal position and momentum offsets are set in lines 10 and 11.

From the result of { 153 }, it was seen that the parameters of the beam phase space: the emittances (ϵ_x, ϵ_y), and the momentum offset (δ) play a crucial role in determining the path length and thus, spin physics. So, the relevant standard deviations of these parameters (set in lines 8-11 in the beam distribution file shown in Figure 44) were not changed during the investigations in this thesis. In fact, in the interest of comparability among results and overall reproducibility of findings, it

was also decided that a single beam distribution, consisting of the initial phase space parameters of 1024 particles, be initially generated and only this be reused in each simulation. Thus, only the system settings of the storage ring (like fields and optics) are varied between simulations, while the beam distribution is kept constant.

5.5.3 Parallelization Scheme

One of the primary challenges to simulations of spin dynamics in BMAD is the long computation times. This is due to a variety of factors, such as the small step size in the quantization of the lattice to ensure accuracy of transport, to the large number of matrices to process in the closed-orbit calculations [64].

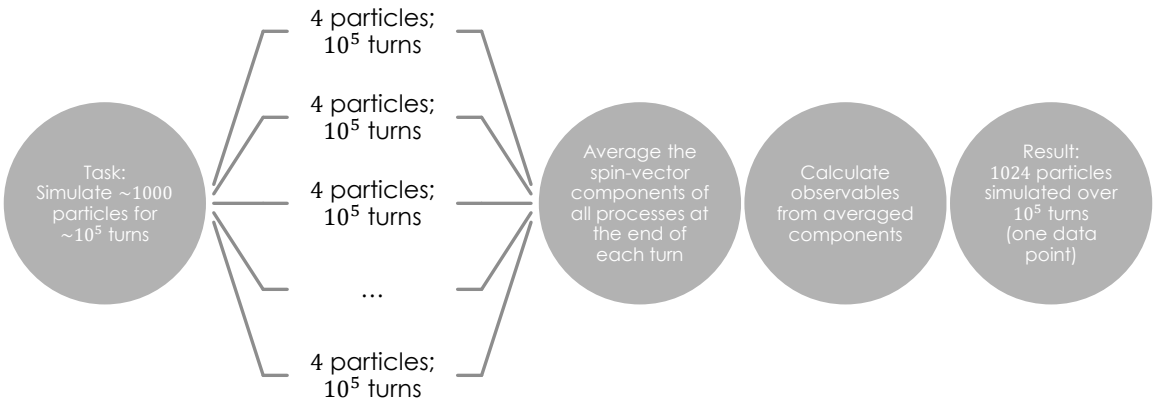

Figure 45: Parallelization scheme for simulation of 1024 particles in a computing cluster with 256 cores.

In beam tracking mode, the transportation is performed on each individual particle, one-by-one. The time required to do this, as expected, rises linearly with the number of particles simulated, unless the job is parallelized. However, BMAD does not provide a default scheme for multithreading, due to which, parallelization must be implemented by hand.

Since this study neglects the effect of intra-beam interactions on beam and spin transport, a method was devised to distribute the job among the 256 cores available in the IKP, Jülich computing cluster.

The number of particles to simulate was decided on the idea of optimizing between statistical accuracy and computing time. Following the example of [67], the number of particles was decided to be at least 1000.

Thus, to each core in the cluster, the simulation of 4 particles were assigned in standalone programs, whose data was then merged by averaging. The scheme is shown in Figure 45.

This scheme managed to cut the processing time by more than 99% as compared to earlier single-program simulations, while keeping the results invariant.

5.5.4 Time development of polarisation vector magnitude

Shown in Figure 46 is a plot showing the variation over time of the spin polarisation vector of the 1000-particle bunch.

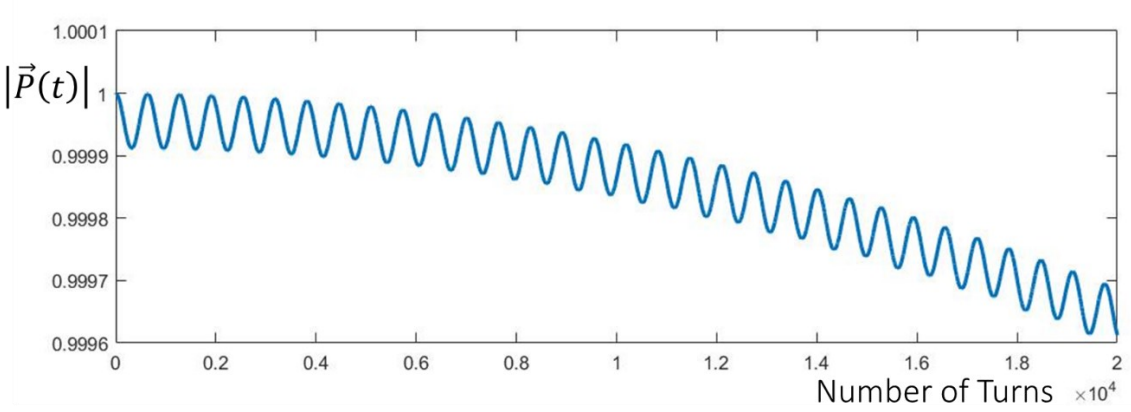

Figure 46: A plot showing the development of the magnitude of the polarisation vector of 1000 particles in a Gaussian bunch as a function of number of turns simulated. The decoherence phenomenon is observed as the steady decline in value after several turns.

The plot shows a clear demonstration of two phenomena that affect the polarisation vector. In the short term the observed oscillations (or "fluctuations") of the magnitude is indicative of the effect of the synchrotron oscillations on the momentum offset. Essentially any variations on the momentum offset also induce a change in the particle's Lorentz factor, which in turn causes a change in the particle's spin tune. This is why the fluctuations on the polarisation vector magnitude is on the same time scale as the synchrotron oscillations.

However, when measured specifically, the fluctuations appear to be exactly twice as frequent as the synchrotron oscillations. A possible explanation for this could be that the frequency with which a particle's spin returns to its mean position depends on its initial position on the longitudinal phase space. From { 109 }, the momentum offset of a particle at a given time is:

$$\delta(t) = \delta_0 \cos\psi - z_0 \sin\psi \qquad \{ 191 \}$$

Since the harmonic number of the prototype lattice is 1 (i.e., only one bunch is simulated with a single RF cavity), the spatial period (distance between the separatrices) of the longitudinal phase space spans the entire ring circumference. Considering that the initial longitudinal beam width is several orders of magnitude lower than this, one can essentially consider $z_0 \approx 0$. This fact is further visualized in Figure 48. From this, the contribution of a particle to the spin decoherence can be calculated as:

$$\Delta\theta(t) = -\frac{v}{\rho}\int_0^t \Delta\nu_s\, dt = -\frac{v}{\rho}\int_0^t (\zeta_0\delta + \zeta_1\delta^2)\, d\psi$$
$$= -\frac{\zeta_0\delta_0}{\omega_s}\sin(\omega_s t) - \frac{\zeta_1{\delta_0}^2}{2}t - \frac{\zeta_1{\delta_0}^2}{4\omega_s}\sin(2\omega_s t) \qquad \{\ 192\ \}$$

From the above expression, it can be noticed that the spins of particles with an initial momentum offset but no position offset tend to return to their mean position twice in one synchrotron oscillation. The mechanism of this is graphically described in Figure 47.

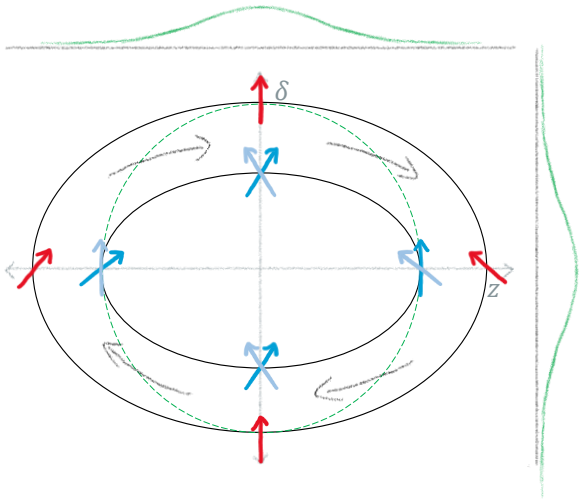

Figure 47: A comparison of the motion paths of particles with different initial phase space coordinates lying on the same Gaussian σ-contour. The projections of the function are drawn in green on the outset. Initially off-momentum particles (red) fluctuate symmetrically on their respective phase space ellipse, returning to their mean position every half turn. Initially off-position particles on the other hand (blue staring from +z and light-blue starting from −z), return to their mean position only once every turn. However, since they follow a much smaller phase-space ellipse, they contribute less to the fluctuations.

The time development of the direction of the polarisation vector on the horizontal plane is tracked by the spin tune spread $\langle\Delta\theta(t)\rangle$, which represents the value of the expression in { 192 } averaged over all the particles. Shown in Figure 49 is a plot of the spin tune spread of the same polarisation vector as measured in Figure 46.

In this plot as well, fluctuations induced by the synchrotron motion can be observed, this time perfectly in phase with the synchrotron motion. This resembles the effect of the first term in the expression of the spin tune spread:

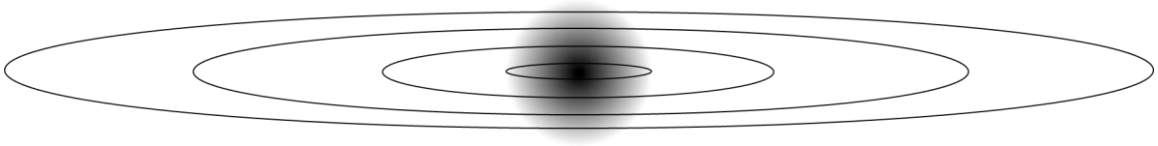

Figure 48: A depiction of the phase space ellipses followed by particles in a typically spatially precise Gaussian distribution. Here the horizontal direction represents position offset, and the vertical represents momentum offset. Since the phase space ellipse is highly eccentric in comparison to the bunch, most particles end up being initially located close to the minor axis of their respective phase space ellipses.

$$\langle \Delta\theta(t) \rangle = -\left(\frac{\zeta_0}{\omega_s}\sin(\omega_s t)\right)\langle \delta_0 \rangle - \left(\frac{\zeta_1}{2}t + \frac{\zeta_1}{4\omega_s}\sin(2\omega_s t)\right)\langle {\delta_0}^2 \rangle \qquad \{ 193 \}$$

The gradual linear shift in the polarisation vector's direction is a direct reflection of the second term in this equation. Normally, one should not see any fluctuations since one would expect the mean momentum offset $\langle \delta_0 \rangle = 0$ in the first term, because that is the initial setting. The presence of fluctuations on the time development suggests an additional effect that introduces a shift in the mean of the momentum spread. In this and other simulations, the amplitude of these fluctuations was found be positive or even negative (initial kick being clockwise instead of anticlockwise). Examples of each of these cases occurring at the same working point (fixed synchrotron frequency) is shown in Figure 50.

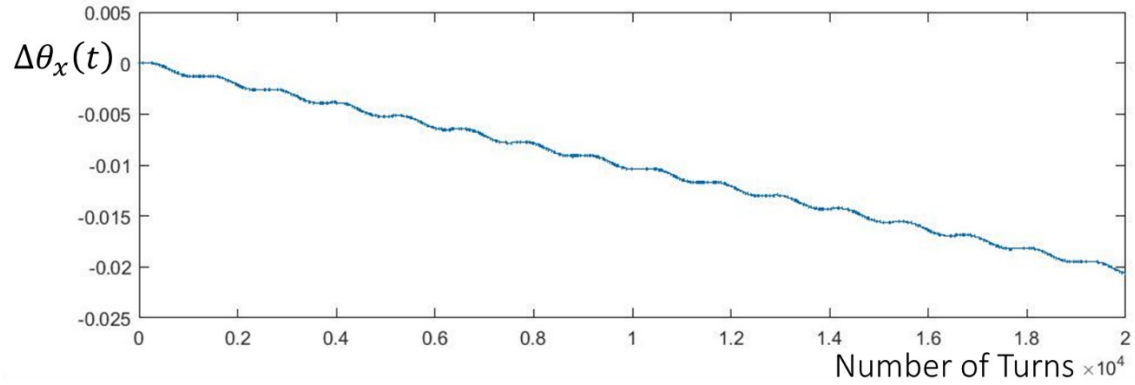

Figure 49: A plot showing the spin tune spread of the polarisation vector measured simultaneously with the experiment in Figure 46.

This "distribution bias" which mostly leans towards positive fluctuation amplitude may be interpreted as the effect of a majority of particles having a shortening in path length per turn, causing them to be initially pushed lower on the δ-axis in the longitudinal phase space (see Figure 47). In other words, the mean of the Gaussian distribution gets shifted down, resulting in a higher contribution from negatively off-momentum particles. If the particles systematically remain evenly distributed along the δ-axis at the start of every synchrotron oscillation, it stands to reason that the spin tune spread would not fluctuate (like in the centre plot in Figure 50), as particles with opposite momentum offsets would be kicked in opposite directions after a quarter cycle, cancelling each other's contributions to the spin tune spread and making the first term in { 193 } zero. The most likely reason behind this is the effect of path lengthening as described in { 153 }. Path lengthening manifests as a fixed shift in δ of all particles with a transverse emittance, which is essentially independent of position on the longitudinal phase space.

The steady directional fluctuation of the polarisation vector is quantified by the fluctuation amplitude $m_v = -{}^{\zeta_0}/_{\omega_s}\langle \delta_0 \rangle$. It can be surmised that in regions with

positive m_ν, the mean momentum offset of the beam is decremented due to the path lengthening while in regions with negative m_ν, the mean momentum offset is incremented.

From the above observations on the depolarization and the change in the polarisation vector's direction, the 9 distinct decoherence modes can be qualitatively defined. These are shown in Figure 53.

The classification of the optimized settings for high spin coherence time into these modes could give insights into the mechanisms governing decoherence.

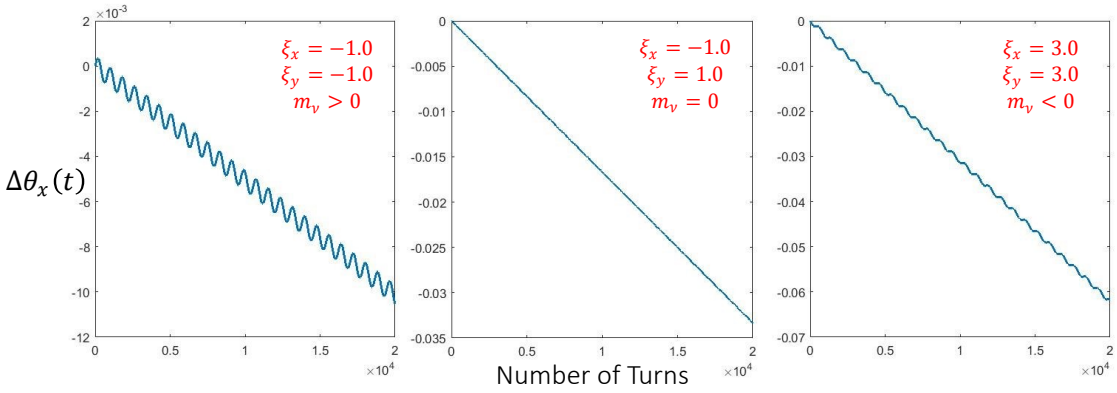

Figure 50: Examples of positive (left), zero (centre) and negative (right) fluctuation amplitudes occurring at different 2° optical settings of the same working point.

From { 192 }, the polarisation vector magnitude can be calculated as follows:

$$\left|\vec{P}(t)\right|^2 = \langle\cos(\Delta\theta(t))\rangle^2 + \langle\sin(\Delta\theta(t))\rangle^2$$
$$= \left(\sum_{i=0}^{\infty}(-1)^i \frac{\left\langle(\Delta\theta(t))^{2i}\right\rangle}{(2i)!}\right)^2 + \left(\sum_{i=0}^{\infty}(-1)^i \frac{\left\langle(\Delta\theta(t))^{2i+1}\right\rangle}{(2i+1)!}\right)^2 \qquad \{ 194 \}$$

This expression when computed, models the loss of magnitude as well as the fluctuations in the form of an expression with both polynomial and harmonic terms. More precisely, if only the linear term in { 193 } is retained the expression becomes a pure polynomial in time t:

$$\left|\vec{P}(t)\right|^2 = \left(\sum_{i=0}^{\infty}(-1)^i \frac{\left(-\zeta_1 t/2\right)^{2i}}{(2i)!}\langle\delta^{4i}\rangle\right)^2 + \left(\sum_{i=0}^{\infty}(-1)^i \frac{\left(-\zeta_1 t/2\right)^{2i+1}}{(2i+1)!}\langle\delta^{4i+2}\rangle\right)^2 \qquad \{ 195 \}$$

When evaluated up to the required number of terms, this model traces out the loss of magnitude as observed in the simulations, but independently of the

fluctuations. A comparison of the model behaviour with an example simulation result is shown in Figure 51.

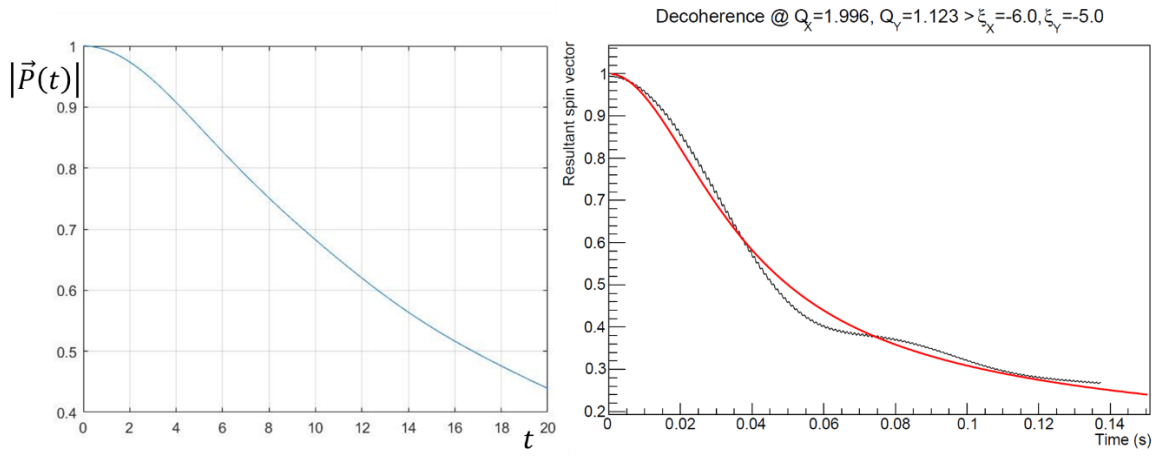

Figure 51: A comparison of the pure polynomial in { 195 } evaluated up to its first 20 terms for a random gaussian sample distribution of δ (left), and the result of a simulation tracking the magnitude of the polarisation vector of 1000 particles at a setting with particularly fast decoherence (right, black curve). The model is observed to represent the nature of the decoherence quite accurately. The red curve on the simulation result represents a 20-term even-powered polynomial being used to fit the data.

Interestingly, it was observed that the amplitude of the directional fluctuations being zero does not necessarily imply minimum decoherence or the disappearance of the magnitude fluctuations. In fact, it was observed that the polarisation vector magnitude continues to fluctuate and the rate of decoherence in such settings were relatively high. The inference drawn from this observation is that the bunch by default has an ensemble spin tune which makes the polarisation vector turn and lose its magnitude in the process. The path lengthening effect which induces a longitudinal shift may be needed to counteract the default turn of the polarisation vector to stabilize it so it maintains its direction with the reference particle spin. Finding this balance could be key to maximizing spin coherence time.

5.5.5 Variation of spin tune error with second-order optics

Based on the result of { 153 }, as well as the findings of the simulations done by [67], the spin tune error is expected to vary linearly with chromaticity. This was observed to be the case when either chromaticity or both were varied. This is shown in Figure 52.

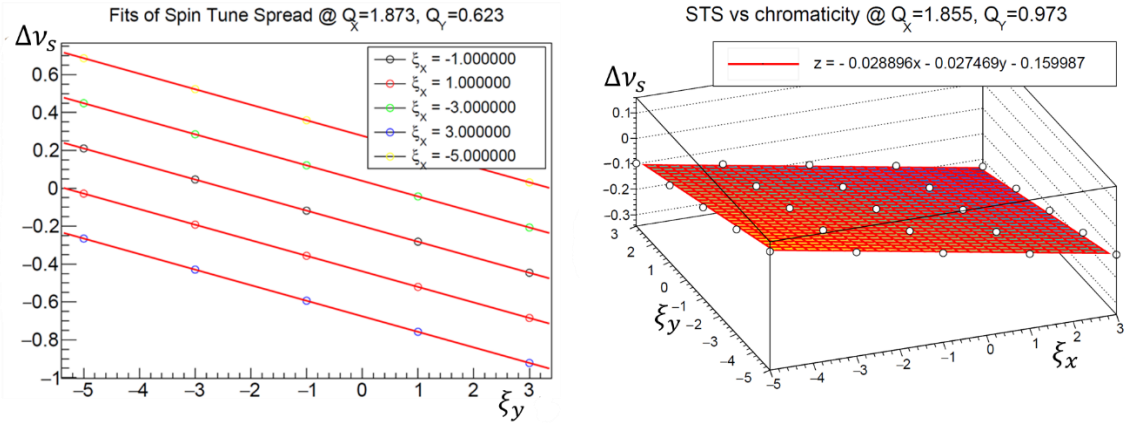

Figure 52: Plots showing the variation of spin tune error with chromaticity. The left plot shows 1D scans varying ξ_y at different fixed values of ξ_x. The right plot shows a 2D scan of a mesh of points that were accurately fit with a plane, whose equation is expressed on top.

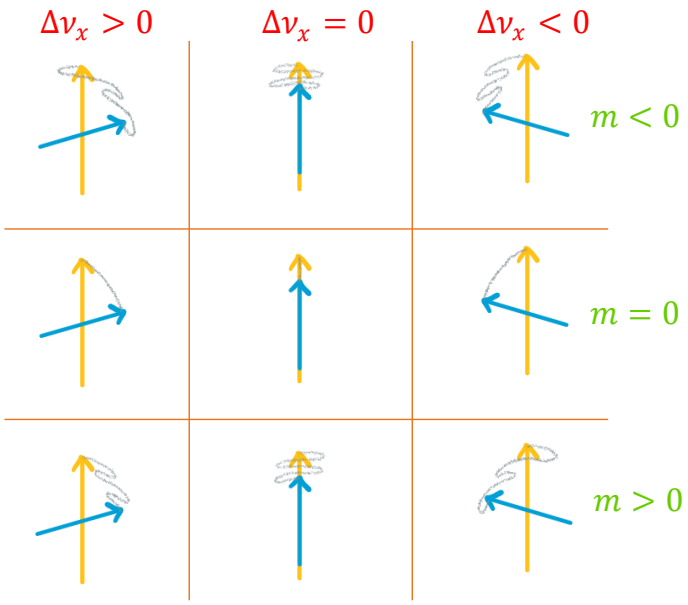

Figure 53: A figurative depiction of the nine distinct modes of decoherence of the polarisation vector observed on the prototype storage ring operating on frozen spin. The yellow arrows represent the initial position of the polarisation vector, the blue ones represent the final positions. The grey curves trace out the trajectory of the top of the vectors as they move from the initial to the final position.

5.5.6 Measuring spin coherence time

The Figure 46 shows a simulation of polarisation vector over 20000 turns in the storage ring. The simulation was performed using the computing cluster at IKP, Forschungszentrum, Jülich, and took about 12 minutes to complete. On an average, this computing cluster with 256 cores manages to complete the simulation of 1000 particles for 100000 turns in 1 hour. However, when measured in time this accounts for only 0.2 seconds of beam time. While it is possible to simulate and measure spin coherence times of the order of hundreds of seconds directly from the data, this is definitely not practical as a single simulation would take too long. Therefore, a method is required to accurately estimate the spin coherence

time from a short beam time simulation. This would also require an accurate modelling of spin depolarization. While { 195 } does present an accurate estimate, it requires the sampling of data for δ for each particle, which may give rise to uncertainties in the estimations at later t values without computational challenges.

Dennis Eversmann in [69] proposes a simpler model that describes spin depolarization in a pure magnetic ring:

$$p_n(n) = \frac{1}{\Delta n}\left[1 + \bar{\epsilon}_0\left(\left[1 - \sqrt{\pi}\gamma_s(n)e^{-{\gamma_s}^2(n)}\,\mathrm{erfi}\left(\gamma_s(n)\right)\right]^2 + \pi{\gamma_s}^2(n)e^{-2{\gamma_s}^2(n)}\right)^{\frac{1}{2}} \times \sin\left[\Omega_s(n) + \frac{\pi}{2} - \tan^{-1}\left(\frac{e^{{\gamma_s}^2(n)}}{\sqrt{\pi}\gamma_s(n)} - \mathrm{erfi}\left(\gamma_s(n)\right)\right)\right]\right] \qquad \{ 196 \}$$

The model tracks the probability of a particle at turn number n to have a polarisation along the longitudinal axis, which in a pure magnetic ring, oscillates with a frequency Ω_s due to a non-zero horizontal precession. It was theorized that this model could be applied to the frozen spin condition, if only the depolarization amplitude were used directly:

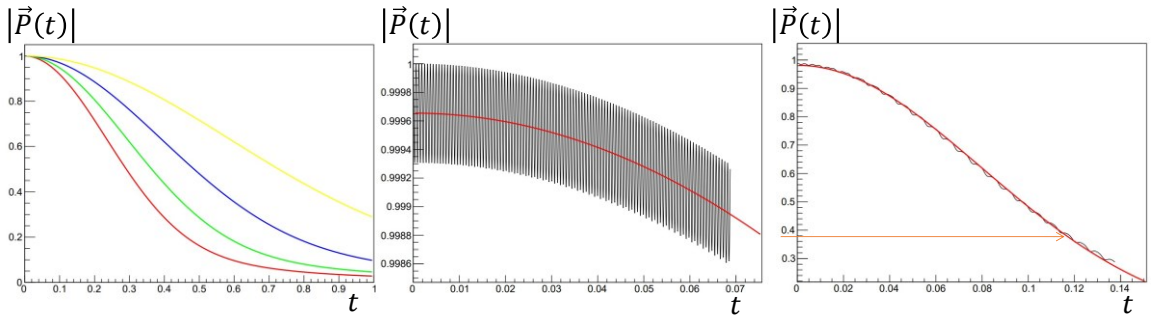

Figure 54: Graphs plotting the Eversmann model shown in { 197 }. The plot on the left shows the development of the model at different values of the damping parameter. The plot in the centre is an example of the model used as a fitting function for the decoherence of the polarisation vector. The plot on the right shows the agreement of the model up to and beyond the $|\vec{P}(t)| = {}^1/_e$ line.

$$\bar{\epsilon} = \bar{\epsilon}_0\left(\left[1 - \sqrt{\pi}\gamma_s(n)e^{-{\gamma_s}^2(n)}\,\mathrm{erfi}\left(\gamma_s(n)\right)\right]^2 + \pi{\gamma_s}^2(n)e^{-2{\gamma_s}^2(n)}\right)^{\frac{1}{2}} \qquad \{ 197 \}$$

Here, $\gamma_s(n) = \sqrt{2}\pi\sigma n$ is termed the "damping parameter" where σ can be obtained from the fit. This model has the advantage of having exactly one free parameter to be determined from fits. Using this as a fitting function, as shown in Figure 54, allows for accurate determination of the spin coherence time from short-term simulations.

5.5.7 Variation of spin coherence time with second-order optics

Studies such as [58] and [46] suggest a linear relationship between chromaticities and the reciprocal of spin coherence time. The applicability of this idea on the prototype ring was tested initially using linear scans. These are shown in Figure 55.

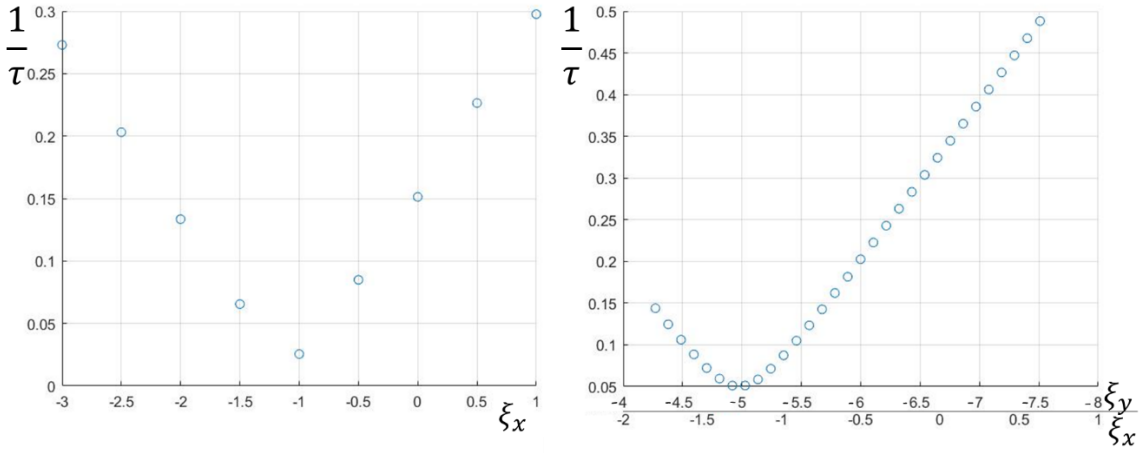

Figure 55: Linear scans measuring the reciprocal of spin coherence time with chromaticity with $\chi_{ss} = 0$. The left plot fixes ξ_y and varies ξ_x. The right plot varies both simultaneously to scan a line on the ξ_x-ξ_y plane.

At first glance, the linear relationship seems apparent. However, at finer scans, such as the one shown on the right in Figure 55, the slight curvature close to the axis suggests the possibility of a different relationship that resembles linearity at sizable values. To find this relationship, a planar scan was carried out as shown in Figure 56. Contour lines generated via interpolation take the shape of a family of ellipses, which led to the idea of a quadratic polynomial in two variables explaining the variation.

Eventually, it was found that a "paraboloid" expression of the form:

$$\frac{1}{\tau^2} = \frac{1}{{\tau_0}^2} + L(\xi_x - \xi_x^o)^2 + M\left(\xi_y - \xi_y^o\right)^2 + N(\xi_x - \xi_x^o)\left(\xi_y - \xi_y^o\right) \qquad \{ 198 \}$$

…would represent a family of ellipses, as well as resemble linear behaviour at large distances from the vertex. Here, ξ_x^o, ξ_y^o are the coordinates of the vertex (these would be the chromaticities optimized for spin coherence time), τ_0 is the maximum spin coherence time (at the optimized point), and L, M, N are the geometrical parameters of the paraboloid. These six parameters are the free parameters to be obtained from the fit.

The model was observed to fit the data precisely at every simulated setting with the errors between the model and simulation data points having a standard deviation in the range of 10^{-12} to 10^{-6} from zero.

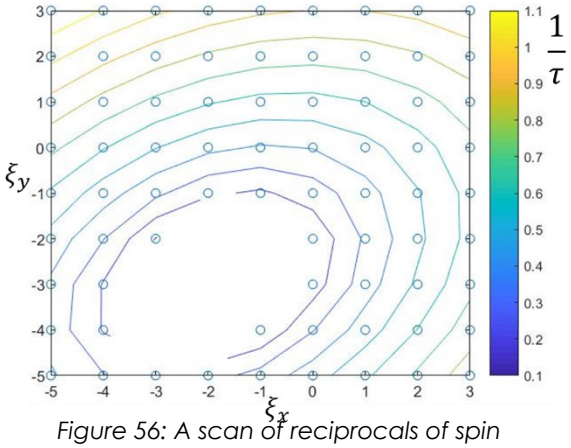

Figure 56: A scan of reciprocals of spin coherence times at a mesh of data points on the ξ_x-ξ_y plane. The coloured curves are interpolated contour lines whose colours represent the value of $1/\tau$ on those contours.

5.6 Grid tests

Using the chosen first working point, parameter space and measurement methods discussed above, it is now possible to perform scans of the quantities of interest over a uniform grid of points in space, which can reveal valuable insights on the "landscape" of the 2° parameter space. Described here, are the outcomes of the first grid tests.

5.6.1 Grid test 1

A scan was done on a grid of points in the ξ-space. Each of the coordinates: ξ_x, ξ_y and α_1, were varied in steps of 2 from -6 to 4, resulting in a grid of 216 data points. These were simulated each for 10000 turns or an equivalent beam time of about $0.014\ s$. In each of these points, the spin coherence time τ, spin tune spread $\Delta\theta_x$, the spin tune error $\Delta\nu_s$, and the amplitude fluctuation coefficient m_ν (qualitatively) were measured.

Based on earlier simulations as well as the results from [67], the spin tune error was expected to vary linearly in all directions. However, the results of this scan show non-linear behaviour in certain regions. This is shown in Figure 57.

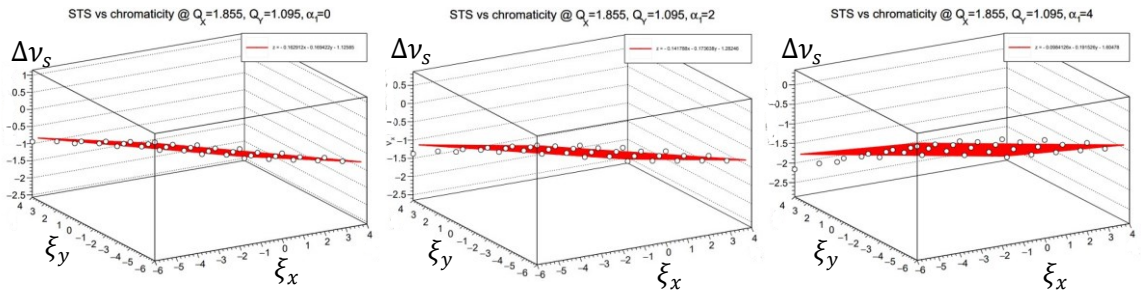

Figure 57: Variation of the spin tune errors with chromaticity at three different values of α_1. The nonlinearities are observed when the values (white dots) are more and more misaligned with the plane fit of the data as α_1 increases.

It was thought possible that due to the placement of the sextupoles SXF and SXSS adjacent to each other in the straight sections, not every optical setting is accessible without setting extremely large sextupole fields. For example, the point $\vec{\xi} = \begin{pmatrix} 4 \\ -6 \\ 4 \end{pmatrix}$, when calculated using { 187 }, requires a field setting of $\vec{\chi} = \begin{pmatrix} 8.0 \\ -0.55 \\ -16.5 \end{pmatrix}$. Strong sextupole fields such as these can cause unprecedented changes in the particle motion, which in this case would lead to unavoidable errors in optimization. To avoid this, the field strength of the straight-section sextupole (χ_{SS}) was henceforth, directly used as a parameter in conjunction with the chromaticities.

5.6.2 Grid test 2

Since the ξ-space is obtained via a fixed linear transformation from the sextupole field space, a space made from a combination of coordinates is also linearly transformable. To get the sextupole settings for the desired chromaticities in this case, the matrix $\boldsymbol{D}$ is defined as follows:

$$\boldsymbol{D} = \begin{pmatrix} 1 & 0 & 0 & 0 \\ \xi_{x_0} & C_{11} & C_{12} & C_{13} \\ \xi_{y_0} & C_{21} & C_{22} & C_{23} \\ 0 & 0 & 0 & 1 \end{pmatrix} \qquad \{ 199 \}$$

Here, C_{ij} is the C-matrix element at row i and column j. Using this, the required sextupole settings are obtained via:

$$\begin{pmatrix} 1 \\ \chi_F \\ \chi_D \\ \chi_{SS} \end{pmatrix} = \boldsymbol{D}^{-1} \begin{pmatrix} 1 \\ \xi_x \\ \xi_y \\ \chi_{SS} \end{pmatrix} \qquad \{ 200 \}$$

This new vector space can be referred to as the λ-space where a vector $\vec{\lambda} = \begin{pmatrix} \xi_x \\ \xi_y \\ \chi_{SS} \end{pmatrix}$ has components along the basis vectors $\hat{\xi}_x$, $\hat{\xi}_y$ and $\hat{\chi}_{SS}$. In this new paradigm, a new grid was defined for simulations:

$$\begin{gathered} \xi_x \in \{-5, -3, -1, 1, 3\} \\ \xi_x \in \{-5, -3, -1, 1, 3\} \\ \chi_{SS} \in \{-5, -2.5, 0, 2.5, 5\} \end{gathered} \qquad \{ 201 \}$$

…leading to a total of 125 points. These were simulated each for 20000 turns or an equivalent beam time of about $0.028\ s$.

5.6.2.1 *Grid test 2 Results: Variation of spin tune spread and spin tune error*

As expected, the spin tune spread measured at all 125 points showed linear behaviour and were fitted with linear polynomials to extract the spin tune errors. The variation of spin tune error in each direction was also very linear now that the straight-section sextupole fields are controlled manually. Shown in Figure 58 is a vector field plot of the gradient of the spin tune error. The constant gradient implies that the spin tune error can be modelled according to a linear polynomial in three variables:

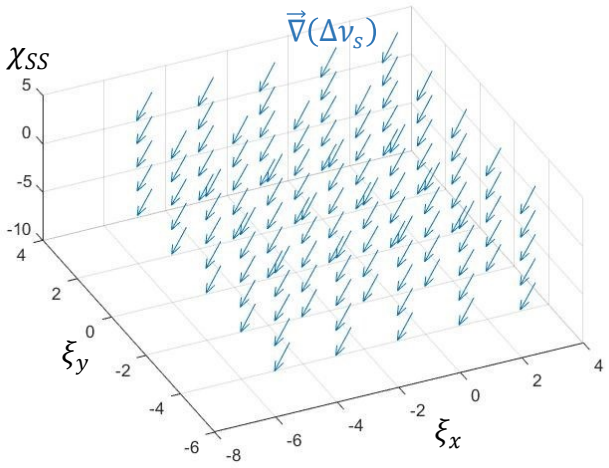

Figure 58: A vector field plot of the gradient of the spin tune error, which demonstrates the linearity of the spin tune error in all directions.

$$\Delta\nu_s(\vec{\lambda}) = \vec{\nabla}_\lambda(\Delta\nu_s)\cdot\vec{\lambda} + \Delta\nu_{s_0} = a\xi_x + b\xi_y + c\chi_{SS} + \Delta\nu_{s_0} \qquad \{\ 202\ \}$$

Here, a, b and c are the components of $\vec{\nabla}_\lambda(\Delta\nu_s)$, where $\vec{\nabla}_\lambda$ is the gradient operator in λ-space, and $\Delta\nu_{s_0}$ is the spin tune error at the origin.

Finally, the specific decoherence mode according to Figure 53 was recognised for each point, transformed into the full optical space, and plotted accordingly to discern a possible spatial pattern. This is shown in Figure 59.

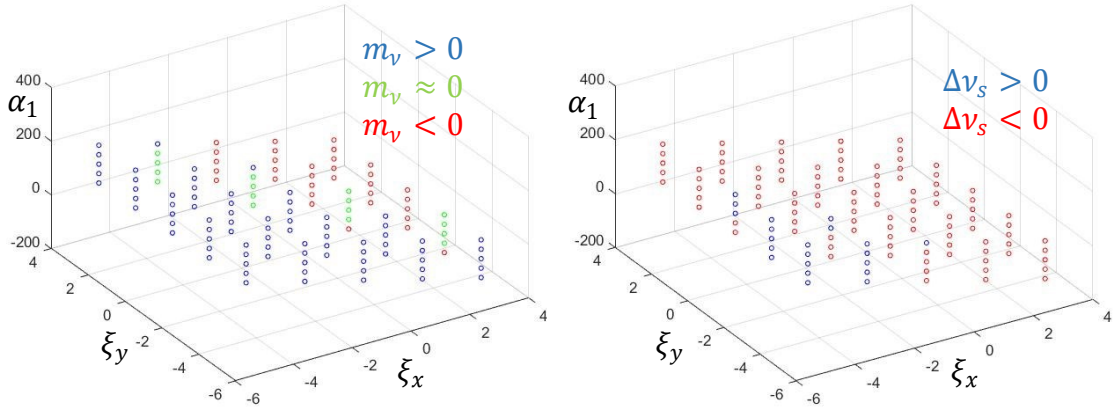

Figure 59: 3D plots of the grid points used in the scan. The left plot colours the points according to the fluctuation amplitude coefficient m_ν. The right plot colours the points according to the spin tune error $\Delta\nu_s$.

From the plots, it can be seen that positive spin tune errors predominantly occur at regions where $\xi_x, \xi_y < 0$ and $\alpha_1 > 0$. This is consistent with the implication of { 153 }, that in these cases, the change in path length would be strictly positive (i.e., the path length increases per turn), giving the particle a higher momentum offset and inducing a positive tune shift.

A similar effect is seen when the fluctuation amplitude is examined. Negative amplitudes predominantly occur when $\xi_x, \xi_y > 0$ and $\alpha_1 < 0$, which is consistent with a strictly negative change in path length and a shifting of the bunch mean down on the δ-axis, which increases participation by $-\delta$ particles in the amplitude fluctuations.

However, an interesting phenomenon to observe from this is the disjoint between the boundaries (zero planes) of $\Delta\nu_s$ and m_ν. This means there are many points with $m_\nu > 0$ and $\Delta\nu_s < 0$. In other words, there are several points where the amplitude fluctuations see a positive change in path length and yet the spin tune receives a negative contribution. This could be a consequence of the first order effect of a momentum offset, which doesn't contribute to the spin tune error, participating in creating the fluctuations. In other words, the effective change in path length is according to { 152 } for the fluctuations, but according to { 153 } for the spin tune error. Additionally, it also implies that some of the modes illustrated in Figure 53 may never be observed, such as $(m_\nu < 0, \Delta\nu_s > 0)$, or $(m_\nu \approx 0, \Delta\nu_s \approx 0)$.

5.6.2.2 Grid test 2 Results: Variation of spin coherence time

The spin coherence time was observed to vary across the grid according to { 198 }. This was verified in each slice of the grid. Shown in Figure 60 are two of the slices where τ and $1/\tau^2$ were measured. The model was fit to $1/\tau^2$ with a standard deviation of less than 10^{-6}, and the parameters were used to directly calculate the fit of τ.

With an accuracy depending on the precision of the fit, the model is also able to estimate the vertex of the paraboloid, which translates to the most optimized setting in that slice. Details about the vertices at each point are given in Table 5. The estimates of spin coherence time at these points are obtained from evaluations of the model but have large errors since the paraboloid vertices are very close to the floor.

Table 5: Locations of the optimum points as estimated by the fitting function, along with (not very precise) estimates of the spin coherence time at these points.

χ_{ss}	ξ_x^o	ξ_y^o	Error on ξ_x^o	Error on ξ_y^o	Estimated τ
-5	-1.376	-5.137	0.163	0.351	71.2
-2.5	-1.349	-4.980	0.170	0.365	18.7
0	-1.183	-4.764	0.163	0.371	16.5
2.5	-1.052	-4.602	0.149	0.374	18.3
5	-1.068	-4.517	0.140	0.337	56.6

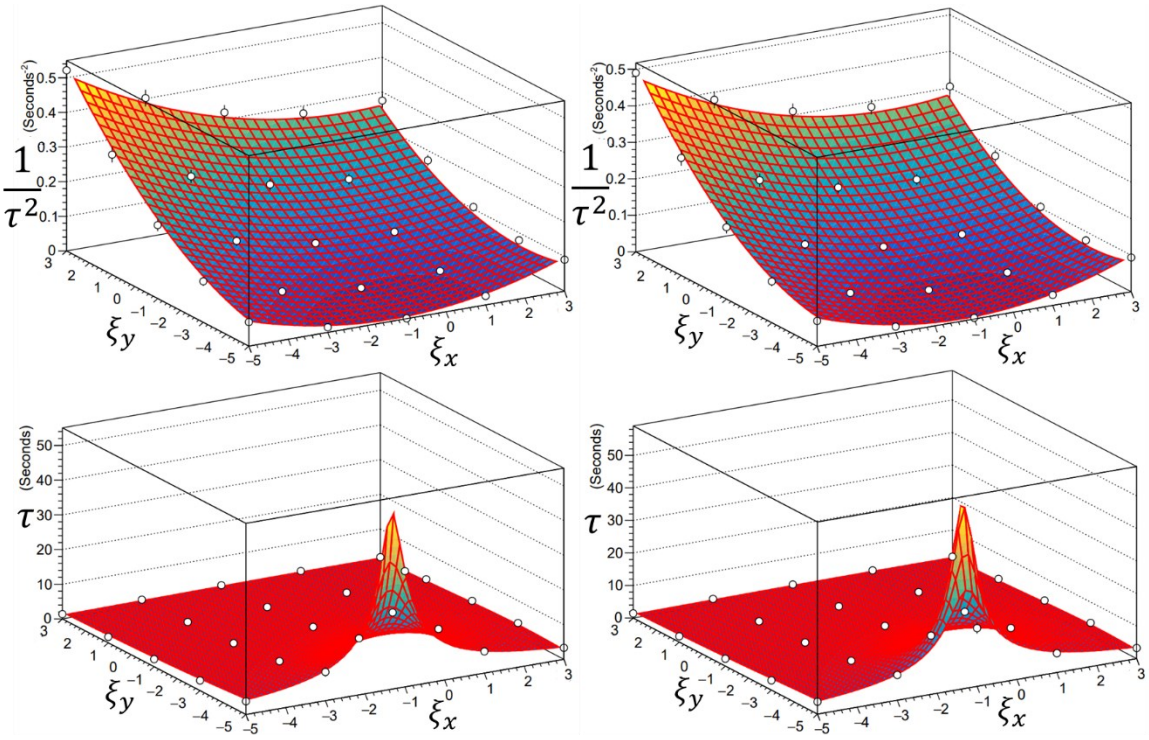

Figure 60: Measurements of spin coherence time (bottom) and its inverse square (top) at the chosen working point with $\chi_{ss} = -5$ (left) and $\chi_{ss} = 5$ (right). The data on the top graphs were fit using the expression in { 198 } and that of the bottom ones were fit with its inverse square root.

The errors on the optimized point locations are also not very insignificant. However, they can be reduced further by increasing the number of turns simulated at each data point. Since this has the downside of increasing computation time, subsequent simulations used a grid with a resolution of 4 (total 64 points) instead of 5 and increased the number of turns simulated to 50000.

The initial expectation from grid test 2 was that the maximum spin coherence time would be where the sextupoles exactly counteract the natural chromaticity and momentum compaction effects, rendering the net effect in the ring to be zero. In other words, the maximum, based on conclusions drawn from pure magnetic rings [46] [58] [61], should be at the origin of the ξ-space. This is however not the case in the prototype ring, where the spin coherence time measured at the origin of this working point was about 3.2 s, which is much lower than not only the estimates

of the five vertices but also than several other sample points considered in the scan.

In fact, just like the minimum spin tune error, the maximum spin coherence time also seems to occur in regions with negative chromaticities. Moreover, it was also observed that $m_y > 0$ in all of the optimized points, which further demonstrates the effect of the first-order momentum offset term in the fluctuations.

5.7 Maximum Spin Coherence Time and Analysis of Grid test Results

From the results of the grid scan in the previous section, it is possible to find the point of maximum spin coherence time in the entire ξ-space associated with the working point. However, it is important to do this as precisely as possible while not spending too much time on the simulation of additional points.

Fortunately, based on previous studies [69] [61] [22] which have broadly investigated the relations between spin coherence times and spin tune spread, it can be reasonably assumed that in the prototype ring as well, maximum spin coherence time would likely coincide with minimum (zero) spin tune spread. This would also stand to reason from a common-sense perspective since a spread in the spin tune in a frozen spin situation basically implies decoherence by definition because the reference particle does not turn.

Therefore, the optimization can be narrowed to the places where the spin tune error is zero. Using the parameters obtained from the gradient of the spin tune error, the equation of a plane representing all points with zero spin tune error is given by:

$$a\xi_x + b\xi_y + c\chi_{SS} + \Delta\nu_{s_0} = 0 \qquad \{ 203 \}$$

This effectively narrows down the optimization problem to a plane of points. However, obtaining this plane itself required simulations of an entire grid. So, to save the time of doing a second planar search, a method was devised to combine the information gained from the grid analysis and the zero-plane to arrive at an estimate of the optimized point.

It was found that when the individual vertices from the paraboloid fits at each slice are plotted on the ξ_x-ξ_y plane, they always tend to lie on a straight line. This is shown to be true for the above grid scan as well, which can be seen in Figure 61.

The collinearity of the local vertices was also thought to be the case based on the hypothesis that the overall function governing the variation of spin coherence time across the ξ-spcae is a 3D paraboloid with an equation of the form:

$$\frac{1}{\tau^2} = \frac{1}{{\tau_0}^2} + L(\xi_x - \xi_x^o)^2 + M\left(\xi_y - \xi_y^o\right)^2 + N(\alpha_1 - \alpha_1^o)^2 + O(\xi_x - \xi_x^o)\left(\xi_y - \xi_y^o\right) + P\left(\xi_y - \xi_y^o\right)(\alpha_1 - \alpha_1^o) + Q(\alpha_1 - \alpha_1^o)(\xi_x - \xi_x^o) \quad \{ 204 \}$$

With L, M, N, O, P, Q as geometric parameters, ξ_x^o, ξ_y^o, α_1^o as the optimized point and τ_0 being the maximum spin coherence time.

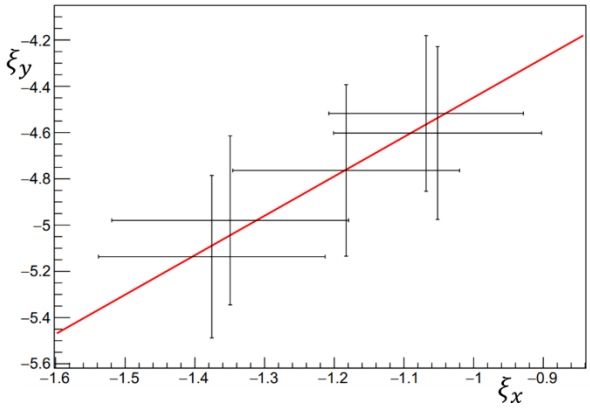

Figure 61: A plot of the vertex points (listed in Table 5) obtained from the paraboloid fits at each slice on the grid scan, plotted on the ξ_x-ξ_y plane with error bars. The straight line represents a linear fit of the data.

The existence of this relation can be loosely justified based the idea that there exists a certain condition ($\zeta_1 = 0$), where the polarization vector as modelled according to { 195 }, maintains its magnitude for a long time. Perhaps this implies that a minimum of three sextupole families are required to achieve this condition, and there seems to exist only one combination of sextupole fields where this is achieved.

While further investigation is required to fully understand the origins of this behaviour, the collinearity of the vertices of the 2D fits, from a purely geometric perspective, strongly suggests that this is in fact how the spin coherence time varies in the parameter space.

While the model { 204 } can be directly used on the grid as a fitting function, a more robust approach was employed, making use of the idea of the zero-plane from { 203 }. The three-dimensional line that best fits the vertex points was found using Principal Component Analysis [70]. Such a line can be represented by the vector equation:

$$\vec{r} = \vec{r}_0 + m\vec{d} \quad \{ 205 \}$$

…where $\vec{d}$ represents the "first principal component" of the dataset, or the vector along the direction of the line of best fit, $\vec{r}_0$ is the position vector of a point on the line, and m is an arbitrary parameter. So, if the idea that the optimized point must lie on the zero plane is true, and all possible vertices obtained from scans of constant-χ_{SS} slices lie on the 3D line given by { 205 }, the optimized point must be

the intersection point of the line and the plane. To find the intersection point, the value of m at that point can be solved for via:

$$\vec{\nabla}_{\lambda}(\Delta\nu_s) \cdot \left(\vec{r}_0 + m\vec{d}\right) + \Delta\nu_{s_0} = 0 \qquad \{ 206 \}$$

…which can be substituted into { 205 } to get its position vector. Figure 62 shows a depiction of the method along with a two-million-turn simulation result from that point.

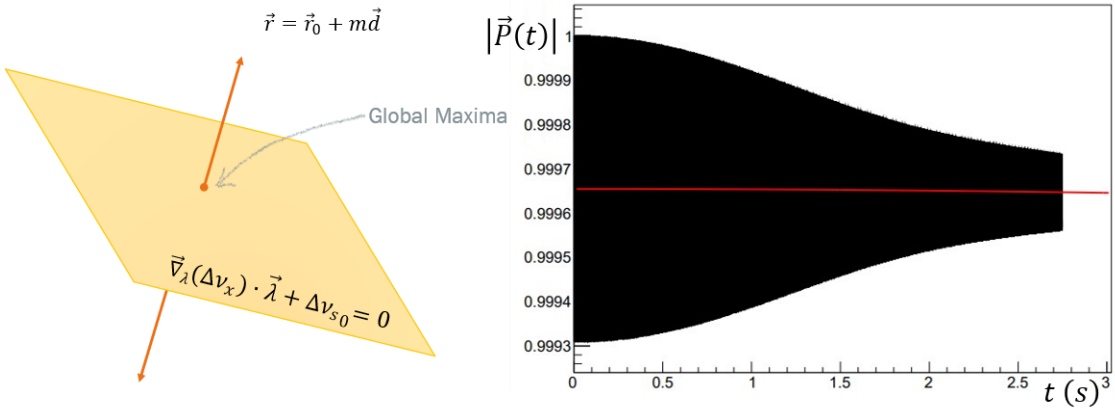

Figure 62: A depiction (left) of the optimization strategy of finding the optimum point via the intersection of the 3D line that best fits the vertices obtained from slice fits, and the plane of zero spin tune error. The graph (right) shows a simulation of two million turns (equivalent to about 2.8 s of beam time) at the optimized point which shows virtually no decoherence. The fitting curve (red) measures a spin coherence time of 1472 s.

This method was also successfully applied to other working points with remarkable success. Many of these points are shown to exhibit 2° settings that lead to spin coherence times of more than 1000 seconds. Shown in Table 6 is a list of working points optimized using this method, along with the estimated lower limits of the maximum spin coherence times at those points.

5.8 Optimization of working point

As discussed earlier, the first working point was chosen on the basis of having natural chromaticity as low as possible. However, this being a very idealized lattice allows the freedom to choose among many working points, which may not be practically workable in a real setting. Thus, it was deemed wise that subsequent explorations have criteria for working point selection which maximizes potential applicability based on current knowledge of applied beam and spin dynamics. Here, three criteria were used: Longitudinal stability, resonances, and beam lifetime, which are described in this section.

5.8.1 Longitudinal stability

As previously discussed in section 2.4.2.2, the condition for longitudinal stability of the beam is that the synchrotron frequency ω_s, which in this case is given by { 105 }, be a real number. For this to be the case, the phase slip factor η_0 must be a negative number. Since the phase slip is related to the change in path length, which is determined by the dispersion function, it can vary with the quadrupole settings. This means that only those working points whose quadrupole settings give rise to a negative phase slip can be chosen. These are any of the points to the right of the red line in Figure 39.

While the possibility of accessing the other working points by changing the RF phase by π radians was considered, it wasn't fully certain if this would keep all other systematic factors invariant. Moreover, since quadrupoles can be finely tuned, what is accessible is still a large number of working points with distinct properties, which would already require a lot of time to simulate and analyse. Therefore, it was decided to keep the RF phase at 0, and proceed with the investigation of only the accessible working points.

5.8.2 Betatron and spin resonances

Resonances as discussed previously are phenomena which lead to severe or possibly fatal instabilities in the beam or in spin polarisation, but usually isolated to a small vicinity of a very specific setting. For example, if a betatron tune or the spin tune is an integer, it leads to even the smallest imperfection in the lattice being resonantly applied and its effects magnifying exponentially. Depending on whether it is a betatron or a spin resonance, it would lead to eventual particle loss or rapid spin depolarisation.

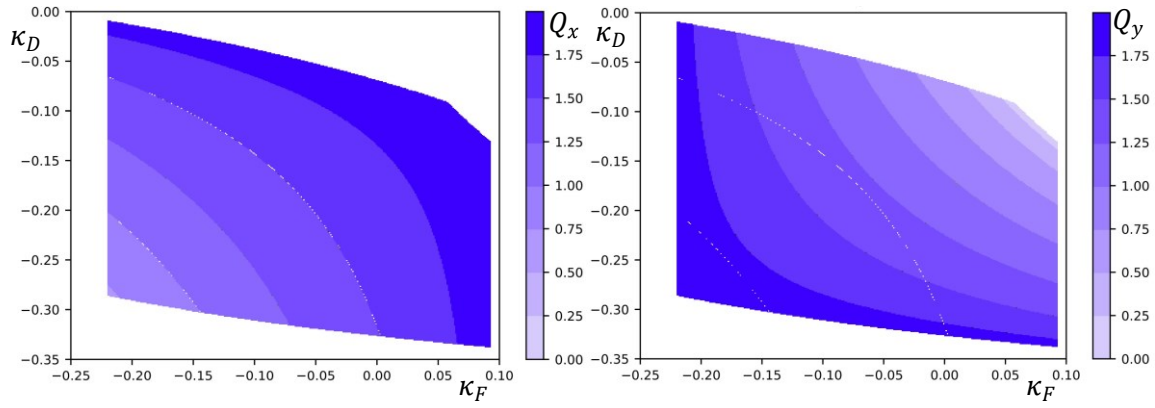

Figure 63: A scan of betatron tunes at all quadrupole settings that fulfil the stability criteria. This is similar to the scan shown in Figure 38, but done by [67] with a higher resolution. The sparse white "curves" are gaps in the data due to beam instability at betatron resonance conditions.

Since this study considers an idealized lattice with very few imperfections, resonances affect stability only when the system is set very precisely on the resonance setting. In other words, resonances in the simulation are very sharp, which is why in the betatron tune scan whose results are shown in Figure 38 wasn't affected by resonances. The field values simulated didn't result in the exact tunes that fall on a resonance. However, a finer scan done in [67] (shown in Figure 63) show gaps of missing data in the interpolated surfaces due to hitting resonance tunes.

Working points at or close to resonances are best avoided in real-life storage rings. Thus, the working points recommended to be implemented in a real storage ring are chosen with this criterion. Shown in Figure 64 is a tune diagram where points lying on any line represents a resonance setting. The working points simulated and optimized for spin coherence time in this study are also marked on the tune diagram.

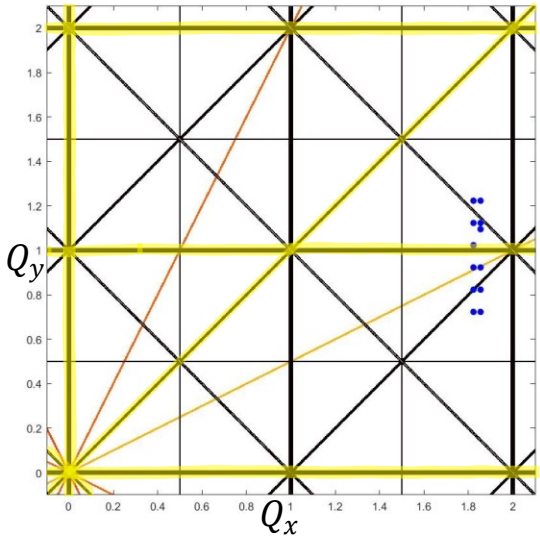

Figure 64: A tune diagram generated for the prototype ring in frozen spin mode, showing the various resonance configurations across the betatron tune spectrum. The black lines represent betatron resonances up to second order and the coloured lines represent spin resonances up to third order. The highlighted lines are settings where both resonances coincide.

It can be seen that some of the points on Figure 64 lie close to a resonance configuration. While these are points which were simulated and optimized in the lattice-wide survey, these would be points not recommended for potential beam tests in the real prototype ring.

5.8.3 Beam Lifetime

Apart from stability and resonance conditions, it is also important to consider the configurations which make it easier for the beam to remain confined and continue to exhibit the properties it had on injection for as long as possible.

While the lattice used in this study doesn't consider this, the beam stored in the ring is subject to many processes that tend to erode the beam of particles over time as it continues to traverse the ring. Some of the most significant of these: Hadron interactions and Coulomb scattering with residual gas particles and intra-beam scattering due to space charge are studied extensively in [71].

5.8.3.1 Hadron interactions and Coulomb scattering

This type of beam loss mechanism involves residual gas atoms and molecules being present in the beamline due to imperfect vacuum conditions. The beam

loss rate due to beam particles undergoing these interactions can be calculated from the interaction cross section:

$$\frac{1}{\tau_{HC}} = n_t \sigma_{HC} f_0 \qquad \{ 207 \}$$

Here, τ_{HC} is the "beam lifetime", defined in a similar fashion to spin coherence time, as the time taken for the beam's viable population to reduce by $1/e$. n_t is the areal particle density of the target (residual gas) particles, and $f_0 = \omega_0/2\pi$ is the revolution frequency of the beam. The interaction cross section $\sigma_{HC} = \sigma_H + \sigma_C$ is the sum of those of Hadronic interactions, which can be modelled according to Regge theory [72], and Coulomb scattering, which can be modelled according to the Rutherford scattering model [73].

5.8.3.2 Intra-beam scattering

In this mechanism, the particles in the beam Coulomb-scatter amongst themselves to cause longitudinal heating of the beam, leading to a loss due to particles crossing the separatrix (see section 2.4.2). These can be modelled according to the Touschek effect [74], giving the beam loss rate:

$$\frac{1}{\tau_I} \approx \frac{r_p c^4}{4\gamma^3 v^3 \langle\sqrt{\beta}\rangle \delta_a^2} \sqrt{\frac{\pi N}{L\epsilon^3}} \qquad \{ 208 \}$$

Here, r_p is the classical proton radius, γ is the Lorentz factor, $\langle\sqrt{\beta}\rangle$ is the average value of the square root of the beta function across the ring, N is the total number of particles, ϵ is the emittance, and δ_a is the momentum offset acceptance of the beam.

5.8.3.3 Total beam loss rate

The total beam loss rate is given by the sum of the individual ones:

$$\frac{1}{\tau_{loss}} = \frac{1}{\tau_I} + \frac{1}{\tau_{HC}} \qquad \{ 209 \}$$

…where τ_{loss} is the effective beam lifetime.

5.8.3.4 Working point criteria

The study [36] calculates these effects specifically on the lattice being studied in this thesis, but at the all-electric mode with particle momenta at 247 MeV/c. These are still useful as a reasonable upper limit of beam loss rates as most beam losses scale inversely with beam momentum due to increased rigidity of the beam [75].

The study compares simulations in the same lattice with different focussing strengths through different quadrupole settings and finds that in general, lattices with maximum values of beta function: $\beta_{max} < 100\,m$ in either direction are a reasonable choice for longer beam lifetimes, typically with $\tau_{loss} > 1000\,s$. This criterion is fulfilled by all working points chosen in the lattice-wide survey for spin coherence time optimization.

5.9 Lattice-wide Optimization Survey

The lattice-wide survey forms the main experimental venture of this thesis, where the criteria, techniques, strategies, and adjustments optimized based on the insights gained from the preliminary scans and grid tests are applied and repeated systematically to survey as many working points as possible.

Besides the working point $(Q_x = 1.855, Q_y = 1.095)$ already optimized in the grid tests, the set of points surveyed were a 2D grid consisting of two lines of values on Q_x:

$$\begin{matrix} Q_x \in \{1.823, 1.855\} \\ Q_y \in \{0.723, 0.823, 0.923, 1.023, 1.123, 1.223\} \end{matrix} \quad \{\ 210\ \}$$

This survey took about 500 hours of simulation time at the IKP computing cluster at FZ-Jülich, not counting the simulations rendered unusable due to coding or human error. The results of this survey, as well as insights gained from the overall analysis of the data collected are discussed in the following chapter.

6. Results and Discussion

In this chapter, the results of the lattice-wide survey, which is the main dataset acquired during the course of this work, is presented, and discussed along with overall insights gained from the analysis of simulations of the V3 lattice.

With the setup of the prototype ring and the V3 lattice being relatively new and not many roadmaps available from previous studies, the investigation of this lattice has been more of an exploration than a rigid procedure, as the strategies and techniques employed have evolved as new information was acquired. Shown in Figure 65 is a rough retrospective map of the investigation conducted.

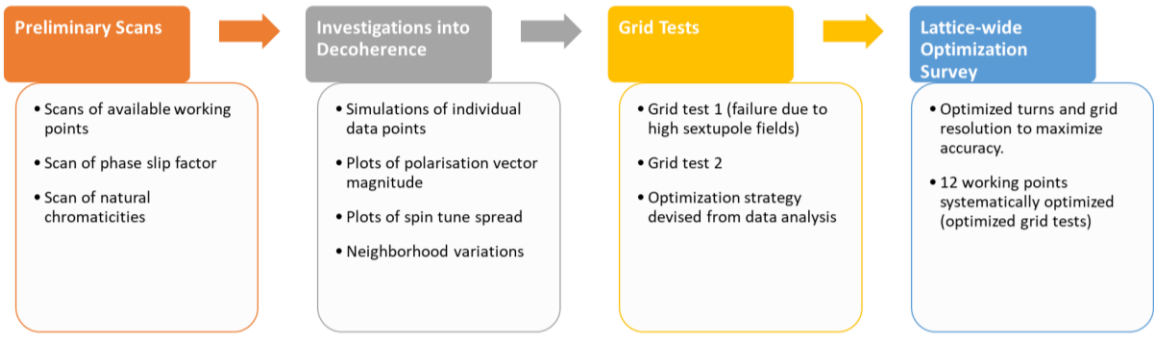

Figure 65: A temporal "map" describing the sequence of actions that form the investigation of the lattice

6.1 Achievements of this study

A previous study, [67], has simulated the exact same V3 lattice that is currently investigated in this thesis, with the objective of finding the optimized second-order settings which maximize spin coherence time at a single working point $(Q_x = 1.823, Q_y = 1.123)$ characterised by relatively low natural chromaticities. However, with V3 having been developed recently at the time of this study, and simulation times being long, only nine data points were simulated in the course of the work. The maximum spin coherence time measured in this study was about 5 seconds.

One of the key achievements of this work is the achievement of spin coherence times of more than $1000\,s$ at multiple working points through an empirical

modelling of the lattice parameters, combined with an optimization based on the understood theory of magnetic storage rings.

This was also achieved with the help of an optimization of the simulation scheme to support parallel programming, which drastically reduced computing time. This is described in section 5.5.3.

To obtain the relevant and necessary parameter of second-order momentum compaction factor, which could not be calculated by BMAD at the unique setup of the prototype storage ring, a method was devised to measure this straight from the data, which is described in further detail in section 5.4.2. This method provided a parameter that varied linearly with the sextupole field strengths, which is exactly as expected of the second-order momentum compaction factor based on the currently accepted models [76] [61].

The current research also presents a method of optimization which has demonstrated robustness in optimizing second-order parameters in a way that is universally applicable at any given working point. This can be particularly useful when further research on the circumstances of the prototype ring renders one or more of the currently studied points unviable for practical application.

Furthermore, insights gained as well as data collected on the factors that influence the error on the spin tune and its distribution across the phase space of the beam seem to suggest the existence of contributions external to the current models that describe it. These are most likely the consequence of the electric bending, which is a relatively unexplored area in spin physics [8].

A model describing the variation of spin coherence time with the second-order optical parameters is also presented in this thesis. This model has shown consistent success (normalized Chi squared errors of less than 10^{-6} at slices with above 50000 turns per data point) in fitting the data points at over 1000 simulations in over 20 working points in the lattice, offering confidence that the description is indeed a reflection of phenomena. At larger distances from the optimized point, the model reduces to the linear behaviour very similar to the one observed in experiments at COSY [58] [46], where the limited number of data points makes it difficult to assertively distinguish between linear behaviour and this more nuanced model.

A dataset of 12 optimized working points has been presented which exhibit spin coherence times well above $1000\ s$. These are tabulated in Table 6. However, due to the high uncertainty on the estimations from the model, the table also quotes the lower limits of the spin coherence time calculated using a limiting function. The table also mentions the chromaticity tolerances, i.e., the maximum error in chromaticity within which the spin coherence time is still above $1000\ s$. The tolerances also give information about the width of the maximum spin coherence

time peak, which help in assessment of the required sensitivity of the sextupoles in achieving such spin coherence times.

Finally, from the overall analysis of the results, conclusions are drawn about the advantages and the disadvantages of this lattice when it comes to achieving high spin coherence times. Also discussed are the possible improvements to the lattice that may not only increase the spin coherence time but also the means to achieve it in practice.

In the following sections, some of these results are discussed in further detail.

6.2 Optimization method

The strategy for optimization of second-order parameters was developed over the course of simulations of the first and second grid scans, as detailed in section 5.6. Apart from the first working point, the method has shown success with 12 other working points leading to the detection of settings with more than the targeted spin coherence time. The method is described as follows:

1. Perform a grid scan of the 3D space formed by the coordinates ξ_x, ξ_y, and χ_{ss}, typically on a cubic grid with 4 or more points along each edge and simulating each point for 50000 or more turns around the storage ring lattice. The grid size and the number of turns must be large enough to have accurate fits by the paraboloid model in { 198 }, on whose estimations the optimizer heavily relies on. At each simulated point, measure spin coherence time τ and spin tune error $\Delta\nu_s$.
2. Fit the spatial distribution of the spin tune error with a linear polynomial in three variables like { 202 }, and estimate the plane of zero tune error.
3. Perform fits of the spin coherence time on each slice of constant χ_{ss} with the paraboloid model and use the fit parameters to estimate the local maximum on the slice.
4. Fit a three-dimensional line to the points in space that represent the slice maxima and locate the point where the line intersects the zero-plane estimated in step 2. The coordinates of this point should be

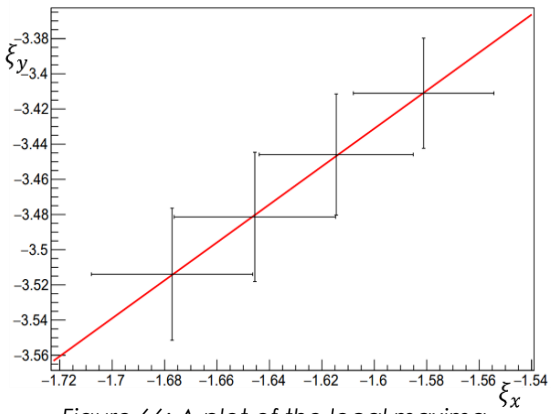

Figure 66: A plot of the local maxima (paraboloid vertices) detected in the slices of constant χ_{ss} at the working point $Q_x = 1.855$, $Q_y = 0.823$. The plot highlights the reduced uncertainty and the stricter collinearity of the vertices as compared to Figure 61, as a result of increasing the number of turns simulated per point.

the optimized settings with the highest spin coherence time at that working point.

The accuracy of steps 3 and 4 since the grid scan described in section 5.6, has significantly improved after increasing number of turns simulated from 20000 to 50000, despite reducing the number of simulated points from 125 to 64. Shown in Figure 66 is a plot of the local maxima detected at the working point $\mathrm{Q_x} = 1.855$, $\mathrm{Q_y} = 0.823$. With this, the maximum absolute uncertainty on the optimized point from step 4 also reduced from 2.6 in the first grid scan to 0.21 at a this one.

6.3 Optimized working points

The complete set of working points which have been successfully optimized to reach the highest possible spin coherence time are shown in Table 6, together with their optimized optical and field parameters, lower limits on spin coherence times and the maximum tolerances in chromaticity for $\tau > 1000\ s$.

Table 6: A tabulation of all working points which were optimized using the method developed in chapter 5. Shown here are the optimized 2° optics. The model-predicted spin coherence times, their estimated lower limits, and the maximum chromaticity tolerances for $\tau \geq 1000\ s$ (measured based on the lower limits). The thick border separates the points from the two series on Q_x. The shaded row shows data on the first working point eventually optimized over the course of the grid tests (see section 5.6)

Q_x	Q_y	κ_F	κ_D	ξ_x^o	ξ_y^o	α_1^o	τ_{model}	τ_{low}	Δ^{ξ}_{1000}
1.855	0.723	0.062	-0.165	-1.845	-2.831	0.2997	1801	1173	0.010
1.855	0.823	0.068	-0.188	-1.635	-3.469	0.1365	2834	2769	0.022
1.855	0.923	0.072	-0.209	-1.480	-4.009	-0.0282	667	666	
1.855	1.023	0.075	-0.228	-1.351	-4.527	-0.0451	3470	2413	0.025
1.855	1.095	0.077	-0.242	-1.271	-4.904	-0.0756	1473	1472	0.020
1.855	1.123	0.077	-0.247	-1.253	-5.036	-0.156	877	1614	0.016
1.855	1.223	0.079	-0.264	-1.167	-5.626	-0.211	3721	3237	0.013
1.823	0.723	0.036	-0.140	-1.483	-1.353	0.0543	677	676	
1.823	0.823	0.055	-0.177	-1.465	-2.389	0.0132	6105	4154	0.016
1.823	0.923	0.062	-0.201	-1.337	-2.983	-0.0573	5647	3870	0.019
1.823	1.023	0.066	-0.223	-1.221	-3.489	-0.1584	1439	1347	0.015
1.823	1.123	0.070	-0.243	-1.124	-4.006	-0.2142	4449	4420	0.022
1.823	1.223	0.072	-0.261	-1.038	-4.508	-0.2572	2575	2571	0.019

The Table 6 shows significantly high spin coherence times at all points, with eleven out of the thirteen points showing lower limits above $1000\ s$. However, a concerning observation is the low tolerance on chromaticity errors, meaning that the sextupoles may need to be very precise and fine-tuned bring about this long spin coherence time.

6.3.1 Measurements of lower limits

While the model described in { 197 } is extremely useful for the optimization process, its uncertainty rises when needed to extrapolate for spin coherence times of the order of $\sim 10^3\ s$, with depolarisation data of $\sim 3\ s$ in equivalent beam time. This is particularly the case at the optimized point. To get a useful measurement from this point, a method was devised to obtain lower limits at these points, through the use of the model:

$$\left|\vec{P}(t)\right| = 1 - Ct^2 \qquad \{ 211 \}$$

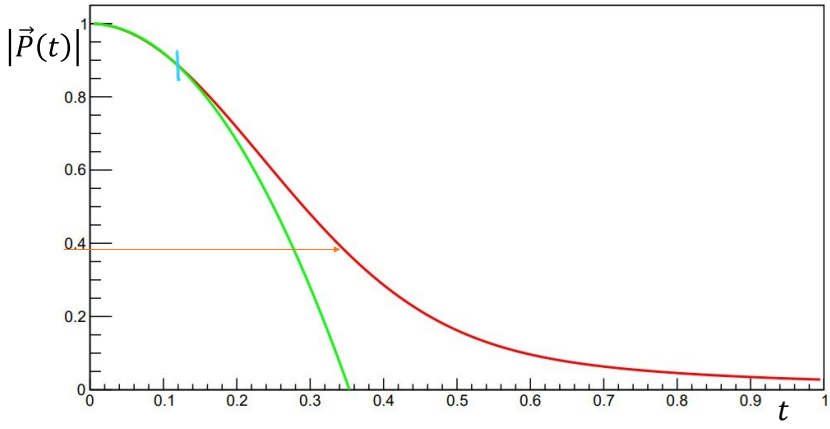

Figure 67: A graph plotting the model in { 197 } (red) and the parabolic model in { 211 } (green). The single free parameter of the parabola was tuned to fit the curve up to the blue tick. The progression shows that the estimated spin coherence time from the parabola could be regarded as a reasonable lower limit, as it possesses no new inflection points.

…where C is a parameter to be obtained from a fit. It was observed that in every case of longer ($> 10\ s$) spin coherence time, this function accurately fits the trend, but always crosses $\left|\vec{P}(t)\right| = {}^1/_e$ at a lower time than the decoherence model. A graph of the two models is shown in Figure 67.

6.3.2 Measurement of chromaticity tolerance

The term maximum tolerance Δ^{ξ}_{1000} is used to refer to the maximum uncertainty permissible in the setting of the chromaticity (in both directions) within which the spin coherence time would still be above $1000\ s$. This quantity was estimated due to the observation that despite achieving high spin coherence times, the peak is often quite sharp, which puts into question the possibility to achieve such precision in the chromaticity setting with real sextupoles on a real storage ring. This quantity helps put this concern into perspective.

The Δ^{ξ}_{1000} was measured by calculating the minor radius of the elliptical contour of $\tau = 1000\ s$ of the function { 198 }.

6.4 Discussion on lattice performance

The lattice considered in this study has a diameter of around $30\ m$, which is quite small, considering the field strength required to store particles at momenta of nearly $300\ MeV/c$. Fortunately, this is achieved with the combination of electric and magnetic bending fields. That being said, the most remarkable advantage of this lattice is the freezing of the proton spin: a key requirement in the EDM search. Focusing requirements are also important since storage rings of such small sizes are subject to higher dispersion effects, and the lattice shows reasonable optical flexibility due to the presence of three families of quadrupoles and sextupoles, allowing for a wide range of working points to be accessible.

However, the lattice also seems to have certain shortcomings. One for instance is the placement and distribution of sextupoles. The initial grid scan performed on the ξ-space (coordinates: ξ_x, ξ_y, and α_1) failed to produce viable results due to the extremely high sextupole field strengths reached at many points, which led to non-linearities in measurements (shown in Figure 57). This occurred primarily because of the QSS family of sextupoles being placed on the straight sections in close proximity to the QF family. In such situations, it often happens that the sextupole effects on particles passing through them begin to cancel out due to their strengths having opposite signs. But the aberrations caused to the particle motion due to the fields being so high may not exactly cancel out. For instance, the quadratic terms in { 81 }, which were previously ignored since x and y at the sextupole would likely be small, now begin to act significantly, deviating the sextupole from its ideal behaviour of simple chromaticity correction.

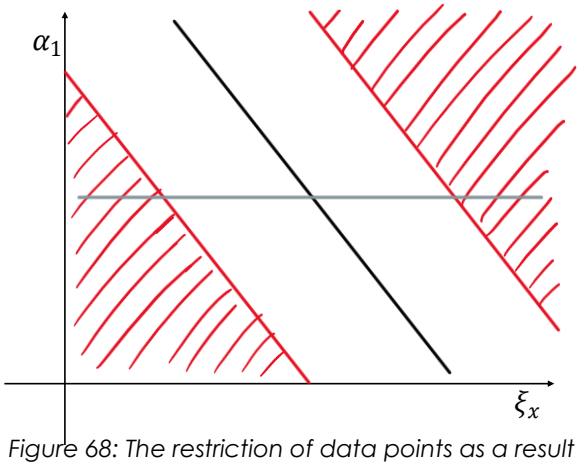

Figure 68: The restriction of data points as a result of the sextupoles SXF and SXSS being placed in close proximity at the straight sections. Points along the grey line of constant α_1, like the slices used in the first grid scan, have points within the high sextupole field zones (marked in red). When the fields were manually adjusted, point-sets such as the black line, began to be considered.

This effect can also be observed in the configuration of the $\boldsymbol{C}^{-1}$ matrix expressed in { 187 }. From the middle column, it can be deduced that ξ_y contributes relatively less to the field strengths, while the large values on the first and third columns reflect their major contributions to the fields. This can be interpreted as the ξ_x-α_1 plane being restricted to a narrow channel of viable points, as shown in Figure 68. When slices of constant α_1 are scanned, the fringes of the slice might lie in the

restricted (high field) zone, where non-linear behaviour is expected. This was the observation in Figure 57.

The final shortcoming of the lattice is the superimposed magnets. A quadrupole and a sextupole field being applied in the same position is not a practically implementable setup. Moreover, the bending magnets are implemented according to the hard-edge model, where fringe field effects, which occur in real systems, are not taken into consideration. That being said, in preliminary investigations onto unexplored paradigms such as frozen-spin dynamics, one can greatly benefit from design simplicity such as superimposed fields, not only in modelling and predictability, but also in terms of computing time requirements.

While lattice improvements are needed, the preliminary knowledge and findings from simplistic adaptations serve as a valuable guide to finding the areas that need them most.

7. Outlook: Areas yet to be Explored

The results obtained during the course of this study shows that the prototype storage ring is a promising venture in terms of taking us closer to the goal of measuring the EDM of the proton. That being said, work doesn't end here either.

The performance of this lattice, as discussed in the previous chapter reveals shortcomings which may hinder the accessibility of the second-order optical settings required to be fine-tuned to maintain spin coherence. Fortunately, with a long-term perspective in mind, this may be an addressable issue.

In this brief chapter, two possible alternatives are suggested to tackle these issues faced with the current prototype lattice.

7.1 A Racetrack Lattice

The term "racetrack" here is used to describe a lattice design with four straight sections, but with one pair of opposite straight sections longer than the other. By definition, this kind of lattice would not have a four-fold symmetry.

This is in fact the scheme on which COSY is based on (see section 3.2.1). Through the reduction of the superperiodicity of the lattice from $P = 4$ to $P = 2$, the three families of sextupoles can now be accommodated in between the bending sections where the dispersion function would have relatively large values. A scheme of this design option is shown in Figure 69.

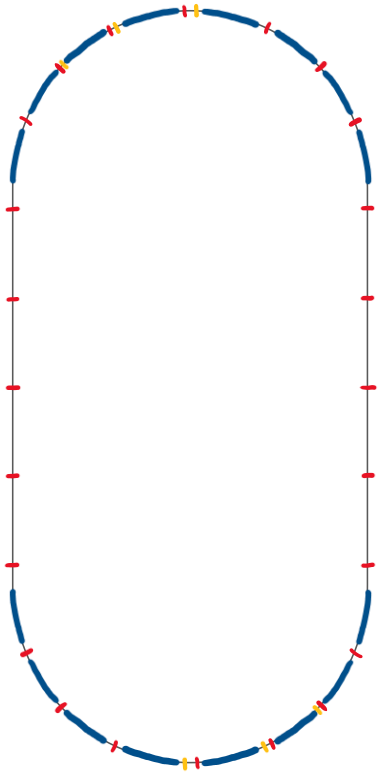

Figure 69: A scheme of the racetrack lattice for the prototype ring. The blue bands are the EM bends, the red ticks represent quadrupoles, and the yellow ticks represent sextupoles.

Each semi-circular arc has one member of each of the three sextupole families, thus providing the

required second-order optical flexibility for the optimization of spin coherence time.

The option was proposed in 2022 [77] and was also simulated for its optical properties. Shown in Figure 70 is the result of this simulation.

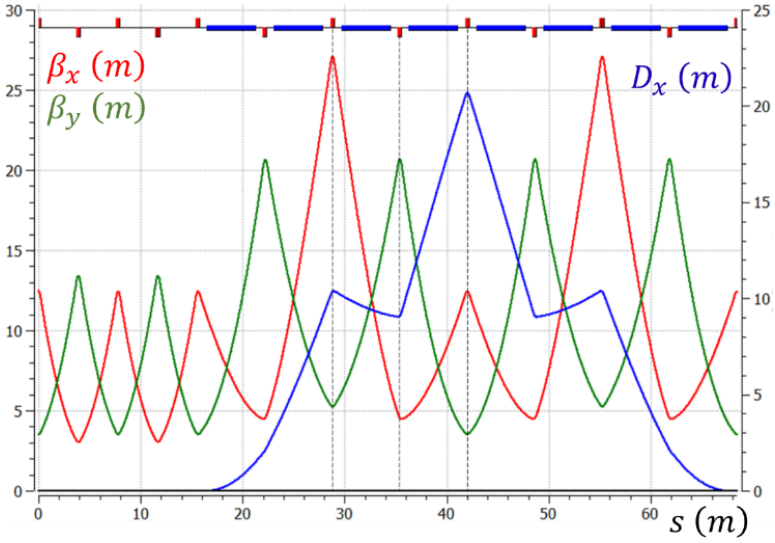

Figure 70: Simulation results of the racetrack lattice showing the variations of the transverse beta functions (left vertical axis) and the horizontal dispersion function (right vertical axis) over one superperiod of the lattice, as performed by [77]. A linearized scheme of the superperiod is expressed at the top of the graph for reference. The dotted vertical lines represent the positions of the three sextupole families.

The significant phase advance combined with the changes to the betatron and dispersion functions between the sextupoles allows for more efficient manipulation of the second-order optics via the sextupole fields as compared to the current lattice.

Furthermore, preliminary findings of simulations have also revealed that the lattice is capable of achieving spin coherence times of up to $1000\ s$, which in principle meet the demands of potential EDM measurement.

More specifics on the performance of the ring in meeting the original requirements of the prototype ring, as well as circumstances of this result are still under research by members of the JEDI collaboration.

7.2 An improved Four-fold Symmetry Lattice

A second option that can be considered is a modification of the existing lattice with a four-fold symmetry to accommodate three families of magnets within a superperiod such that there is a sizeable phase advance between them. A scheme of this idea is shown in Figure 71.

In this lattice, each bend is now $30°$ instead of $45°$, giving rise to two gaps instead of three, thus providing the room for a third family of sextupoles. Apart from the

efficiency in second-order optics manipulation, it also offers flexibility in the first order by enabling the efficient use of the third quadrupole. The main advantage of this option is that the key features of the original design, such as weak vertical focussing to minimize EDM signal detection noise and the possibility of direct scaling from the prototype ring to the final all-electric ring, are retained while still enhancing second-order optical flexibility.

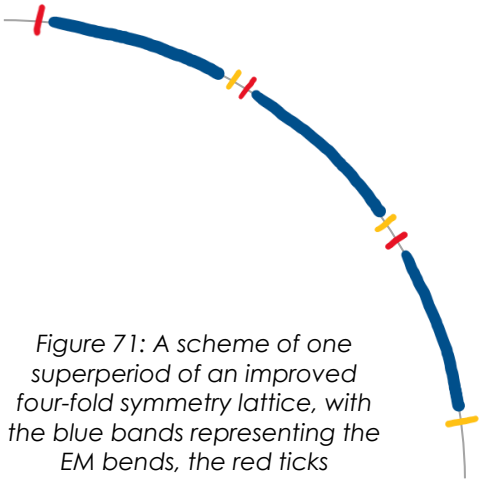

Figure 71: A scheme of one superperiod of an improved four-fold symmetry lattice, with the blue bands representing the EM bends, the red ticks representing quadrupoles while the yellow ticks represent sextupoles.

However, since this plan has not yet been implemented as a lattice in BMAD or any of the other accelerator physics simulation platforms, the viability of this option as an improvement to the prototype ring design is yet to be assessed via simulations.

8. Summary and Conclusion

The search for answers to the yet unsolved mystery of the matter-antimatter asymmetry has been the inspiration for much physics research in recent years, including that of the JEDI collaboration, which aims to address this question by designing and building a dedicated storage ring to measure the EDM of protons with never before achieved sensitivity. To gain the much-needed insights on the systematics of the rather unexplored experimental setups such as frozen spin, electrostatic particle confinement, and simultaneous counter-rotating beams, a smaller prototype storage ring was proposed as an intermediary proof-of-principle experiment. The present study performs an extensive analysis on an idealised software adaptation of this prototype storage ring, known as the prototype lattice V3, to better understand the circumstances of frozen spin.

The foremost accomplishment of this study can be considered the optimisation of spin coherence times of above 1000 seconds at several working points. This finding hits the target set by the feasibility study of EDM measurement of charged particles using storage rings, based on its required sensitivity.

This work also establishes a robust method of optimisation which has demonstrated universality of working point, and which has optimised spin coherence times of above 1000 seconds at more than 90% of working points examined. Although many of the working points sampled in this study meet the basic criteria of one which is sustainable in a real storage ring, the optimisation method established in this thesis could be useful if the need arises to find the sextupoles settings with highest spin coherence time over a new point or range of points.

In addition, a deeper look into the apparent mechanisms of decoherence undergone by particles in the simulator seem to indicate that spin tunes vary differently in storage rings with an electrostatic bending field as compared to those without. The way this difference manifests in the time evolution of the spin tune spread, and in the distributions of the spin tune error and the decoherence modes over the second order optical space has also been discussed in detail.

Furthermore, based on the initial diagnostics and the analysis of the data from the simulations, the advantages as well as the shortcomings of this lattice have been highlighted. The most crippling problem which severely restricts the second-order optical flexibility of the lattice was found to be in the placement of the sextupoles, which extends to the general configuration of the lattice. An ongoing effort by JEDI to address this issue, as well as a potential new solution in the form of modifications to the structure and configuration of the storage ring have also been proposed as the Outlook of this research.

Finally, it must be pointed out that while the implications of these results have been quite exciting, they still have "a ways to go" before being perfect. The low chromaticity tolerances of the optimized point in order to meet the sensitivity criterion are still quite narrow, which sets a high bar on sextupole precision. While it is foreseen that the lattice improvements explored earlier may relax these tolerances, it is at present unclear if this will in fact be the case. That being said, with the optimization method having shown preliminary success, more data is constantly being acquired, which can be used to further understand the intricacies of the prototype storage ring and its combined electric and magnetic bending.

In the outset of the journey through this thesis, the potential for scientific achievement of the idea of the prototype storage ring is well noticeable. As an important and inspiring bridge to a precision measurement that could change our perspective of reality, the success of this project could bring physics closer to understanding the subtle yet pervasive workings of the universe.

9. References

[1] I B Khriplovich and S K Lamoreaux, CP Violation Without Strangeness: Electric Dipole Moments of Particles, Atoms, and Molecules, Berlin: Springer, 1997.

[2] Andrei D Sakharov, "Violation of CP invariance, C asymmetry, and baryon asymmetry of the universe," *Soviet Physics Uspekhi,* vol. 34, no. 5, p. 392, 1991.

[3] W Dekens, J de Vries, J Bsaisou and et. al., "Unraveling models of CP violation through electric dipole moments of light nuclei," *Journal of High Energy Physics,* p. 69, 2014.

[4] G W Bennett, B Bousquet, H N Brown and et. al., "Improved limit on the muon electric dipole moment," *Physical Review D,* vol. 80, p. 052008, 2009.

[5] The Storage Ring EDM Collaboration, "A Proposal to Measure the Proton Electric Dipole Moment with 10-29e.cm Sensitivity," Brookhaven National Laboratory, New York, 2011.

[6] D Anastassopoulos, V Anastassopoulos, D Babusci and et. al. , "AGS Proposal: Search for a permanent electric dipole moment of the deuteron nucleus at the 10−29 e ·cm level," April 2008. [Online]. Available: https://www.bnl.gov/edm/files/pdf/deuteron_proposal_080423_final.pdf.

[7] R Maier, "Cooler synchrotron COSY- performance and perspectives," *Nuclear Instruments and Methods in Physics Research A,* vol. 390, pp. 1-8, 1997.

[8] CPEDM Collaboration, "Storage ring to search for electric dipole moments for charged particles: Feasibility study," CERN Yellow Reports: Monographs, Geneva, 2021.

[9] A Andres, "The Search for Electric Dipole Moments of Charged Particles in Storage Rings," in *20th Conference on Flavor Physics and CP Violation, Oxford, MS*, Oxford, 2022.

[10] P A R Ade, R W Aikin, D Barkats and et. al., "Detection of B-Mode Polarization at Degree Angular Scales by BICEP2," *Physical Review Letters,* vol. 112, no. 24, p. 241101, 2014.

[11] Guinevere Kauffman, "Thermal history of the universe and early growth of density fluctuations," 2019 August 11. [Online]. Available: https://wwwmpa.mpa-garching.mpg.de/~gamk/TUM_Lectures/Lecture4.pdf. [Accessed 2022 November 27].

[12] Werner Bernreuther, "Lecture Notes in Physics: CP Violation in Particle, Nuclear and Astrophysics," in *CP Violation and Baryogenesis*, Berlin, Springer Link, 2002, p. 237–293.

[13] Markus Cristinziani, "Search for antimatter with the AMS cosmic ray detector," *Nuclear Physics B - Proceedings Supplements,* vol. 114, pp. 275-279, 2003.

[14] C S Wu, E Ambler, R W Hayward and et. al., "Experimental Test of Parity Conservation in Beta Decay," *Physical Review Journals Archive,* vol. 105, p. 1413, 1957.

[15] CPLEAR Collaboration, "First direct observation of time-reversal non-invariance in the neutral-kaon system," *Physics Letters B,* vol. 444, no. 1-2, pp. 43-51, 1998.

[16] D J Griffiths, Introduction to Quantum Mechanics, London: Pearson Publishing Company, 1995.

[17] J H Christenson, J W Cronin, V L Fitch and R Turlay, "Evidence for the 2pi decay of the K20 Meson," *Physical Review Letters,* vol. 13, no. 4, p. 138, 1964.

[18] M Kobayashi and T Maskawa, "CP-Violation in the Renormalizable Theory of Weak Interaction," *Progress of Theoretical Physics,* vol. 49, no. 2, pp. 652-657, 1973.

[19] Dan-di Wu, "A Brief Introduction to the Strong CP Problem," in *Workshop in Honor of E C G Sudarshan's Contributions in Theoretical Physics*, Austin, 1991.

[20] P Huet and E Sather, "Electroweak baryogenesis and standard model CP violation," *Physical Review D,* vol. 51, pp. 379-394, 1995.

[21] Maxim Pospelov and Adam Ritz, "Electric dipole moments as probes of new physics," *Annals of Physics,* vol. 318, no. 1, pp. 119-169, 2005.

[22] Marcel Stephan Rosenthal, "Experimental Benchmarking of Spin Tracking Algorithms for Electric Dipole Moment Searches at the Cooler Synchrotron COSY," PhD Thesis, RWTH Aachen University, Aachen, 2016.

[23] J H Smith, E M Purcell and N F Ramsey, "Experimental Limit to the Electric Dipole Moment of the Neutron," *Physical Review,* vol. 108, no. 1, p. 120, 1957.

[24] C A Baker, D D Doyle, P Geltenbort and et. al., "Improved Experimental Limit on the Electric Dipole Moment of the Neutron," *Physical Review Letters,* vol. 97, p. 131801, 2006.

[25] V V Flambaum and J S M Ginges, "The Nuclear Schiff moment and time invariance violation in atoms," *Physical Review A,* vol. 65, p. 032113, 2002.

[26] V F Dmitriev and R A Sen'kov, "Schiff Moment of the Mercury Nucleus and the Proton Dipole Moment," *Physical Review Letters,* vol. 91, p. 212303, 2003.

[27] JEDI Collaboration, "JEDI Collaboration Webpage," FZ Jülich, [Online]. Available: https://collaborations.fz-juelich.de/ikp/jedi/index.shtml. [Accessed 2022 November 28].

[28] I. S. Grant and W. R. Phillips, Electromagnetism, 2nd Edition, John Wiley & Sons, 1991.

[29] Helmut Wiedemann, Particle Accelerator Physics (3rd Edition), New York: Springer, 2007.

[30] S Y Lee, Accelerator Physics (Fourth Edition), Singapore: World Scientific, 2019.

[31] Peter Hansbo, Mats G Larson and Karl Larsson, "Variational formulation of curved beams in global coordinates," *Computational Mechanics,* no. 53, pp. 611-623, 2014.

[32] S Giuducci, "Chromaticity," 1994. [Online]. Available: https://cds.cern.ch/record/398300/files/p191.pdf. [Accessed 2022].

[33] T Risselada, "Gamma Transition Jump Schemes," 1990. [Online]. Available: https://cds.cern.ch/record/213345/files/p161.pdf. [Accessed 2022].

[34] Riu Li, "Discussion of Phase Space and Emittances," in *North American Particle Accelerator Conference*, Chicago, 2016.

[35] D Prasuhn, J Dietrich, R Maier and et. al., "Electron and Stochastic Cooling at COSY," *Nuclear Instruments and Methods in Physics Research Section A: Accelerators, Spectrometers, Detectors and Associated Equipment,* vol. 441, no. 1-2, pp. 167-174, 2000.

[36] Saad Siddique, Andreas Lehrach and Jörg Pretz, "Simulations of Beam Dynamics and Beam Lifetime for a Prototype Electric Dipole Moment Ring," in *24th International Spin Symposium (SPIN2021)*, Matsue, 2022.

[37] S Karanth, E Stephenson, A Wrońska and et. al., "Influence of electron cooling on the polarization lifetime of a horizontally polarized storage ring beam," *Nuclear Inst. and Methods in Physics Research, A,* vol. 987, p. 164797, 2021.

[38] David Newton and Andy Wolski, "Design of Electron Storage and Damping Rings," in *US Particle Accelerator School*, Fort Collins, 2013.

[39] Charles P Slichter, Principles of Magnetic Resonance, Berlin: Springer, 1990.

[40] Hamad M Yehia, Rigid Body Dynamics: A Lagrangian Approach, Switzerland: Springer Nature, 2022.

[41] V. Bargmann, L. Michel and V.L. Telegdi, "Precession of the polarization of particles moving in a homogeneous electromagnetic field," *Physical Review Letters,* vol. 2, no. 10, p. 435, 1959.

[42] Takeshi Fukuyama and Alexander J. Silenko, "Derivation of Generalized Thomas-Bargmann-Michel-Telegdi Equation for a Particle with Electric Dipole Moment," *Int. J. Mod. Phys. A,* vol. 28, no. 29, 2012.

[43] Brian C Hall, Lie Groups, Lie Algebras, and Representations: An Elementary Introduction, New York: Springer, 2015.

[44] W Pauli, "Zur Quantenmechanik des magnetischen Elektrons.," *Springer,* pp. 601-622, 1927.

[45] S Y Lee, "Spin resonance strength of a localized rf magnetic field," *Physical Review Special Topics - Accelerators and Beams,* vol. 9, p. 074001, 2006.

[46] G Guidoboni, E J Stephenson, A Wrońska and et. al., "Connection between zero chromaticity and long in-plane polarization lifetime in a magnetic storage ring," *Physical review accelerators and beams,* vol. 21, p. 024201, 2018.

[47] Yoshihiko Shoji, "Dependence of average path length betatron motion in a storage ring," *Physical Review Special Topics - Accelerators and Beams,* vol. 8, p. 094001, 2005.

[48] N. Hempelmann, V. Hejny, J. Pretz and et. al., "Phase Locking the Spin Precession in a Storage Ring," *Physical Review Letters,* vol. 119, p. 014801, 2017.

[49] D. Eversmann, V. Hejny, F. Hinder and et. al., "New Method for a Continuous Determination of the Spin Tune in Storage Rings and Implications for Precision Experiments," *Physical review Letters,* vol. 115, p. 094801, 2015.

[50] Vera Poncza, Extensive Optimization of a Simulation Model for the Electric Dipole Moment Measurement at the Cooler Synchrotron COSY, Aachen: PhD Thesis, RWTH Aachen University, 2021.

[51] W Kretschmer , A Glombik and et. al., "The polarized ion-source for COSY," in *14th International Conference on Cyclotrons and their Applications*, Cape Town, 1995.

[52] Werner Bräutigam, Ronald Brings and et. al., "Status and perspectives of the cyclotron JULIC as COSY injector," in *NUKLEONIKA*, Warsaw-Krakow, 2003.

[53] V Bocharov, M Bryzgunov, A Bubley and et. al., "Budker INP Proposals for HESR and COSY Electron Cooler Systems," in *AIP Conference Proceedings*, Galena, 2006.

[54] Vsevolod Kamerdzhiev, Ulf Bechstedt, Frank Esser and et. al., "2MeV Electron Cooler for COSY and HESR – First Results," in *Proceedings, 5th International Particle Accelerator Conference*, Dresden, 2014.

[55] D Prasuhn, J Dietrich, R Maier and et. al., "Electron and stochastic cooling at COSY," *Nuclear Instruments and Methods in Physics Research Section A: Accelerators, Spectrometers, Detectors and Associated Equipment,* vol. 441, no. 1-2, pp. 167-174, 2000.

[56] Valeri Lebedev, "Accelerator Physics Limitations on an EDM ring Design," EDM collaboration meeting, Jülich, 2014.

[57] V Anastassopoulos, S Andrianov, R Baartman and et. al., "A storage ring experiment to detect a proton electric dipole moment," *Review of Scientific Instruments,* vol. 87, p. 115116, 2016.

[58] G Guidoboni, E Stephenson, S Andrianov and et. al., "How to Reach a Thousand-Second in-Plane Polarization Lifetime with 0.97-GeV/c Deuterons in a Storage Ring," *Physical Review Letters,* vol. 117, p. 054801, 2016.

[59] D Albers, F Bauer, J Bisplinghof and et. al., "A precision measurement of pp elastic scattering cross-sections at intermediate energies," *The European Physics Journal A,* vol. 22, pp. 125-148, 2004.

[60] J Bisplinghoff, R Bollman, P Cloth and et. al., "Position sensitivity by light splitting in scintillator arrays," *Nuclear Instruments and Methods in Physics Research Section A: Accelerators, Spectrometers, Detectors and Associated Equipment,* vol. 329, no. 1-2, pp. 151-162, 1993.

[61] I A Koop and M Shatunov, "The spin precession tune spread in the storage ring," in *Proceedings of the First European Particle Accelerator Conference*, Rome, 1988.

[62] M Vitz, "Spin-tracking Simulations in a COSY Model using BMAD," in *13th International Particle Accelerator Conference*, Bangkok, 2022.

[63] F Rathmann, N N Nikolaev and J Slim, "Spin dynamics investigations for the electric dipole moment experiment," *Physical Review Accelerators and Beams,* vol. 23, p. 024601, 2020.

[64] David Sagan, "The BMAD Reference Manual," 23 October 2020. [Online].

[65] A Lehrach, S Martin and R Talman, "Design of a Prototype EDM Storage Ring," in *23rd International Spin Physics Symposium*, Ferrara, 2018.

[66] David Sagan, "The Tao Manual," 11 November 2022. [Online]. Available: https://www.classe.cornell.edu/bmad/tao-manual-2022-11-11.pdf. [Accessed 13 November 2022].

[67] Maximilian Vitz, "Simulation and Optimization of the Spin Coherence Time of Protons in a Prototype EDM Ring," Master Thesis, RWTH Aachen University, Aachen, 2020.

[68] J P Shan, S G Peggs and S A Borgacz, "Analytical evaluation of the second order momentum compaction factor and comparison with MAD results," in *International Conference on Particle Accelerators*, Washington DC, 1993.

[69] Dennis Eversmann, "High Precision Spin Tune Determination at the Cooler Synchrotron in Jülich," PhD Thesis, RWTH Aachen University, Aachen, 2018.

[70] Karl Pearson, "LIII. On lines and planes of closest fit to systems of points in space," *The London, Edinburgh, and Dublin Philosophical Magazine and Journal of Science,* vol. 2, no. 11, pp. 559-572, 1901.

[71] S. Siddique, "Beam Simulation of a Prototype Proton Electric Dipole Moment Storage Ring," Master Thesis, RWTH Aachen University, Aachen, 2019.

[72] T Regge, "Introduction to complex orbital momenta," *Il Nuovo Cimento, Springer Science and Business Media LLC,* vol. 14, no. 5, p. 951–976, 1959.

[73] E Rutherford, "LXXIX. The scattering of α and β particles by matter and the structure of the atom," *The London, Edinburgh, and Dublin Philosophical Magazine and Journal of Science,* vol. 21, no. 125, pp. 669-688, 1911.

[74] C Bernardini, G F Corazza, G Di Giugno and et. al., "Lifetime and beam size in a Storage Ring," *Physical Review Letters,* vol. 10, no. 9, pp. 407-409, 1963.

[75] H Bethe and J Ashkin, Experimental Nuclear Physics, New York: J Wiley, 1953.

[76] J Keintzel, L Malina, R Tomás and et. al., "Momentum Compaction Factor Measurements in the Large Hadron Collider," in *Proceedings of the 12th International Particle Accelerator Conference*, Campinas, 2021.

[77] A Melnikov, A Aksentyev and Y Senichev, "Investigation of polarized proton spin coherence time at storage rings," in *13th International Particle Accelerator Conference*, Bangkok, 2022.

[78] Robert S. Orr and William Trischuk, "Superconducting Radio Frequency particle accelerator cavity design/testing," University of Toronto, 2012. [Online]. Available: https://hep.physics.utoronto.ca/~orr/wwwroot/Summer%20Student%20Ad/srf_summ_12.html.

[79] Antonio Riotto and Mark Trodden, "Recent Progress in Baryogenesis," *Annual Review of Nuclear and Particle Science,* vol. 49, pp. 35-75, 1999.

[80] Werner Bernreuther, "CP Violation and Baryogenesis," in *Lecture Notes in Physics: CP Violation in Particle, Nuclear and Astrophysics*, Berlin, Springer Link, 2002, p. 237–293.

[81] Andreas Lehrach, "Introduction to Accelerator Physics - Lecture Series," 30 October 2020. [Online].

[82] Forschungszentrum, Jülich, "Cooler Synchrotron (COSY)," 31 May 2022. [Online]. Available: https://www.fz-juelich.de/en/infrastructure/cooler-synchrotron-cosy.

[83] J Pretz, "Storage Rings for the Search of Charged-Particle Electric Dipole Moments," in *2nd Joint ECFA-NuPECC-ApPEC (JENAS)-Seminar*, Madrid, 2022.

10. List of Figures

Figure 1: A depiction of the history of the universe from the Big Bang until today, where the timescale is represented as labels at the bottom, and our solar system's location (not to scale) is pointed out on the right. Pair production was no longer accessible since after the lepton epoch (marked with a red arrow), somewhere between 10 and 100 s after the big bang, after which the matter-antimatter asymmetry became a permanent feature of the universe. 4

Figure 2: The effect of parity and time reversal transformations on a particle (yellow) with an electric dipole moment (magenta) being subject to an external electric field (red) via electrodes, and magnetic field (blue) via a current carrying coil. The parity transformation (inversion of the vertical coordinate) flips the electrodes while leaving the intrinsic moments and magnetic field invariant. The time reversal flips the intrinsic moments and the magnetic field but leaves the electric field invariant. Both transformed systems would behave differently than the original, thus demonstrating the violations of the transformations. 9

Figure 3: The connection of CP violating sources and the EDMs of various particles. The different momenta (EDM, magnetic quadrupole moment and Schiff moment) are shown in red; the effective couplings are shown in blue. Solid arrows represent a stronger contribution than dashed arrows. [22] 10

Figure 4: A schematic of the neutron EDM experiment using the Ramsey method, with the stages marked on top, and the neutron polarisation direction at those stages are marked in green below. The blue arrows indicate the direction of the magnetic field at each step. The red half arrows indicate that the electric field is flip-flopped to generate a variation in the EDM signal. [22] 11

Figure 5: A depiction of particle motion in a synchrotron. A particle with a positive charge ends up traversing a circular path under the influence of a magnetic field of a specific value uniformly maintained along the desired path. The direction of the acceleration is always along the radial direction. 15

Figure 6: A photograph of a RF cavity being tested by TRIUMF at the University of Toronto [78], with markings showing the cylindrically symmetric poles and cavities. 17

Figure 7: A schematic showing the cavity structure (violet) and the effective charges on the poles due to the applied RF voltage. The red curve shows the spatial variation of the voltage. The right side shows the same setup as the left, but half a time-period later. If the phase ϕ is adjusted so that the particle always feels

a negative slope, and the frequency νc is varied so the phase velocity of the voltage is always equal to the particle velocity, the particle can receive a constant field for a steady acceleration. 17

Figure 8: The arrangement of poles and the consequent field configuration of a focussing quadrupole. The diagram shows five particles at different transverse positions, all moving in the direction pointing out of the page, as well as the respective forces (black arrows) they experience due to the local magnetic field (blue arrows) they perceive. 18

Figure 9: A figure depicting a quadrupole acting as a converging lens. A paraxial particle at any transverse distance δ from the principal (beam) axis crosses over at the same point marked by the focal length f due to the linear dependence of the Lorentz acceleration with transverse offset. 20

Figure 10: Configuration of a sextupole magnet for dispersion error corrections along the horizontal (xz) plane. The forces experienced by particles at different locations on the transverse plane (yellow circles) due to the apparent fields (blue arrows) are denoted by the black arrows. 21

Figure 11: A drawing representing the right-handed Frenet-Serret coordinate system used to define the measurables of beam and spin dynamics in this thesis. The values marked in yellow are those of the location parameter s. 22

Figure 12: The Courant-Snyder ellipse drawn by a particle with emittance ϵ. The origin of the plot represents the reference particle ($\epsilon = 0$). Also marked are the maximum amplitude ($\beta\epsilon$) and velocity ($\gamma\epsilon$) attained during the betatron motion. 26

Figure 13: A visualization of the transformations to the phase space ellipse during the process of transport from $s = s1$ to $s = s2$ 28

Figure 14: An illustration of the variation of the phase space ellipse during transport. 28

Figure 15: An example of error amplification due to betatron resonance at $Qx = 5$. [81] 29

Figure 16: A diagram depicting the motion of an off-momentum particle in the absence of focussing. The motion of the offset particle (black curve) through an element $d\theta$ of the "ring angle", can be represented as a function of that of the reference particle (yellow curve). 33

Figure 17: A cylindrical pillbox cavity. The left image shows a lateral cut-section, where the direction and distribution of the electric field, as well as wall current losses can be seen. The right image shows an axial view, where the induced magnetic field due to the varying electric field is depicted. [81] 36

Figure 18: The phase space representation of "stationary" synchrotron oscillations. The contours in the graphs represent paths followed by particles at a certain

energy. The left image shows the limits of the stable oscillations, known as separatrices. Particles with phase space parameters within the limits of the separatrices follow closed paths representing stable oscillations. Particles with phase space parameters beyond the separatrix limits follow open paths, and essentially get debunched. The right image shows the same phase space with an additional dimension of particle energy, where the RF "buckets" can be visualized. The energy of the bucket centers is the energy $E0$ of the reference particle. [29] 38

Figure 19: A phase space representation of "moving" synchrotron oscillations where $\phi s > 0$. The top image shows the "spreading out" of the separatrices as the particle phase reduces. The bottom image shows the same with the energy coordinate, where it can be seen that each bunch is at a higher energy than the next as the bucket centres accelerate. It can also be noticed that as the synchronous phase increases, the phase space gets steeper, but the buckets get shallower. [29] 39

Figure 20: A diagram showing the orientation of the invariant spin axis on the transverse plane in a pure magnetic ring. The axis is tilted outward due to the EDM component of the precession. 54

Figure 21: A diagram showing a Wien filter field configuration with the electric and magnetic fields along the radial and vertical axes. The axis of precession (kicks) due to the Wien filter would be exactly along BW. 55

Figure 22: Some specifications of the staged approach currently pursued by the JEDI collaboration for proton EDM measurement. [8] 57

Figure 23: A picture describing the layout of COSY, showing the JULIC ion source and cyclotron, the stacked stripping injection path, and the "racetrack" style synchrotron. Also labelled are the various components. [50].....58

Figure 24: A photograph of the COoler SYnchrotron (COSY) accelerator and storage ring at the Forschungszentrum, Jülich, Germany. [82].....59

Figure 25: Basic layout of the prototype ring, consisting of eight dual superimposed electric and magnetic bends and two families of quadrupoles (F, focusing; D, defocusing), with an optional skew quadrupole family at the midpoints. [8].....60

Figure 26: Left: Cross-section of the capacitor (in red) inside the beam tube (outer circle). Right: One-quarter of the combined electric and magnetic prototype ring. Two $cos\ \theta$ iron-free dipoles surround the beam tube, in which the capacitor plates are accommodated. [8].....61

Figure 27: Left: Electric storage ring with simultaneously clockwise and counterclockwise circulating beams (dark and light blue arrows), each with two helicity states (green and red arrows for each beam). The grey circles represent electric field plates. Right: One quadrant of a full-scale, all-electric, frozen-spin EDM storage ring. The straight sections are marked in green whereas the bending

sections are marked in grey. The ticks on the beamline mark the electric quadrupoles whose field strengths are mentioned. The blue ticks are focussing quadrupoles while the red ones are defocussing. [8] 62

Figure 28: Measurements of the in-plane polarisation of the precessing bunch as a function of time. The scale is set so that the normalized polarization is unity at $t = 0$ s. The two panels represent two different sextupole field settings, resulting in polarization lifetimes, defined in [58] as the time for the normalized polarisation to reach 0.606, are 64.7 ± 5.4 s and 18.6 ± 2.6 s in (a) and (b), respectively. [58] 66

Figure 29: Two lines with error bands show the places where the x and y chromaticities were consistent with zero. The locations of the points of largest polarisation lifetime (spin coherence time) are shown by the circles and plusses. Circles indicate the results with a beam with high horizontal emittance, while the plus signs indicate those by a beam with a large longitudinal width. [46] 67

Figure 30: Relevant parameters for the deuteron EDM experiment at COSY. [9] .68

Figure 31: The angle α of the polarisation vector with the horizontal (ring) plane, as a function of time. At $t = 100\,s$, the vertically polarised beam is rotated onto the horizontal plane. At $t = 155\,s$, the RF Wien filter and the Siberian Snake are turned on and the vertical polarisation begins to linearly build up. In this measurement, the settings were $\phi WF = 0.945\,mrad$, $\xi sol = 0\,rad$, $\phi rel = 0.79\,rad$. [9].....69

Figure 32: A plot showing the dependence of the rate of the vertical polarisation build-up calculated from the linear fit of Figure 31 with the relative phase ϕrel of the RF Wien filter. The points were fitted with a sinusoidal model $12\pi d\alpha dn = Asin\phi rel + Bcos\phi rel$. The amplitude of the function $\epsilon = A2 + B2$ is the resonance strength. [9].....69

Figure 33: Resonance strength ϵ , plotted against the Wien filter rotation angle ϕWF and the angular displacement of the spin due to the Siberian snake ξsol. The points are fitted with the function { 172 }, and the minima of the surface gives the orientation of the invariant spin axis. [9] 70

Figure 34: A floor plan of the V3 prototype lattice, generated by Tao [66]. The devices marked EM are the electromagnetic bends, QF, QD, and QSS are the quadrupoles of the three different families, and RF is the RF cavity. The red arrow points to the spot on the beamline that is considered the origin of the laboratory coordinate system used in the plot ($X = 0$, $Z = 0$). This point corresponds to $s = 0$ in the Frenet frame. 72

Figure 35: A snippet from the BMAD file description of the V3 lattice. The length of the EM bends and the particle momentum are set in lines 9 and 26 respectively. Line 35 sets the "default" magnetic field required to close the path. The actual magnetic field is set in line 37, and the electric field required for satisfying the frozen spin condition (see { 161 }) is calculated in line 36. The quadrupole field strengths

are set in lines 18, 19 and 20, while the sextupole field strengths are set in lines 21, 22 and 23. 73

Figure 36: Bending radius (green curves) and particle momentum (blue lines) contours plotted as a function of electric and magnetic fields. The red star plots the configuration of the prototype ring (currently investigated in this thesis) and the red circle plots that of the all-electric ring (described in section 3.2.3) [83] ...74

Figure 37: Twiss parameters measured at quadrupole settings given by $\kappa F = 0.077$ and $\kappa D = -0.242$. The straight-section quadrupole is currently turned off. The red, green, and blue curves represent the horizontal beta function, vertical beta function and the horizontal dispersion function respectively as functions of the distance s along the ring. The points marked by stars are the locations of quadrupoles (also the superimposed sextupoles). All units are in metres. 75

Figure 38: A scan of all possible working points. The area covered by the colours are the regions with real values of betatron tunes. The colour-bar on the left plot shows the horizontal betatron tune, and the one on the right shows the vertical betatron tune. 76

Figure 39: A scan of the phase slip factor over all working points on the lattice. The red curve represents the gamma-transition line where $\eta 0 = 0$. Points to its right fulfil the stability condition of $\eta 0 < 0$ 76

Figure 40: Vector-field plots of the gradients of the second-order parameters in the sextupole field space at a working point with $\kappa F = 0.062$ and $\kappa D = -0.165$. The length and direction of each arrow in the three plots represents the magnitude and direction of the gradient of the quantities ξx (left), ξy (centre) and $\alpha 1$ (right). The arrows within a plot having a common magnitude and direction is indicative of a constant gradient across space. 79

Figure 41: The organization of the parameter space explored in this study. The space formed by the betatron tunes Qx, Qy and the phase slip factor $\eta 0$ is the first-order (1°) space, and the one formed by the chromaticities ξx, ξy and the second-order momentum compaction factor $\alpha 1$ is the second-order (2°) space. A point in the first-order space is termed a working point, and one in the second-order space is termed a data point. 79

Figure 42: Natural chromaticities measured over all available working points where chromaticity measurement was possible. 81

Figure 43: Contour curves for $\xi x = 0$ (red) and $\xi y = 0$ (blue) based on interpolations from the graphs in Figure 42. The intersection point gives the field settings of the working point with zero natural chromaticity. 81

Figure 44: A snippet from the beam distribution user input file. The type of distribution is defined for each of the spatial directions in lines 5, 6 and 7. The x and y emittances are set in lines 8 and 9, and the standard deviations of the longitudinal position and momentum offsets are set in lines 10 and 11. 83

Figure 45: Parallelization scheme for simulation of 1024 particles in a computing cluster with 256 cores.....84

Figure 46: A plot showing the development of the magnitude of the polarisation vector of 1000 particles in a Gaussian bunch as a function of number of turns simulated. The decoherence phenomenon is observed as the steady decline in value after several turns. 85

Figure 47: A comparison of the motion paths of particles with different initial phase space coordinates lying on the same Gaussian σ-contour. The projections of the function are drawn in green on the outset. Initially off-momentum particles (red) fluctuate symmetrically on their respective phase space ellipse, returning to their mean position every half turn. Initially off-position particles on the other hand (blue staring from $+z$ and light-blue starting from $-z$), return to their mean position only once every turn. However, since they follow a much smaller phase-space ellipse, they contribute less to the fluctuations. 86

Figure 48: A plot showing the spin tune spread of the polarisation vector measured simultaneously with the experiment in Figure 46. 87

Figure 49: A depiction of the phase space ellipses followed by particles in a typically even Gaussian distribution. Here the horizontal direction represents position offset, and the vertical represents momentum offset. Since the phase space ellipse is highly eccentric, most particles end up being initially located close to the minor axis of their respective phase space ellipses. 86

Figure 50: Examples of positive (left), zero (centre) and negative (right) fluctuation amplitudes occurring at different 2° optical settings of the same working point. 88

Figure 51: A figurative depiction of the nine distinct modes of decoherence of the polarisation vector observed on the prototype storage ring operating on frozen spin. The yellow arrows represent the initial position of the polarisation vector, the blue ones represent the final positions. The grey curves trace out the trajectory of the top of the vectors as they move from the initial to the final position. 90

Figure 52: Plots showing the variation of spin tune error with chromaticity. The left plot shows 1D scans varying ξy at different fixed values of ξx. The right plot shows a 2D scan of a mesh of points that were accurately fit with a plane, whose equation is expressed on top.....90

Figure 53: Graphs plotting the Eversmann model shown in { 188 }. The plot on the left shows the development of the model at different values of the damping parameter. The plot in the centre is an example of the model used as a fitting function for the decoherence of the polarisation vector. The plot on the right shows the agreement of the model up to and beyond the $Pt = 1e$ line.....91

Figure 54: Linear scans measuring the reciprocal of spin coherence time with chromaticity with $\chi SS = 0$. The left plot fixes ξy and varies ξx. The right plot varies both simultaneously to scan a line on the ξx-ξy plane.....92

Figure 55: A scan of reciprocals of spin coherence times at a mesh of data points on the ξx-ξy plane. The coloured curves are interpolated contour lines whose colours represent the value of 1τ on those contours. 93

Figure 56: Variation of the spin tune errors with chromaticity at three different values of $\alpha 1$. The nonlinearities are observed when the values (white dots) are more and more misaligned with the plane fit of the data as $\alpha 1$ increases. 93

Figure 57: A vector field plot of the gradient of the spin tune error, which demonstrates the linearity of the spin tune error in all directions. 95

Figure 58: 3D plots of the grid points used in the scan. The left plot colours the points according to the fluctuation amplitude coefficient mv. The right plot colours the points according to the spin tune error Δvs. 95

Figure 59: Measurements of spin coherence time (bottom) and its inverse square (top) at the chosen working point with $\chi SS = -5$ (left) and $\chi SS = 5$ (right). The data on the top graphs were fit using the expression in { 189 } and that of the bottom ones were fit with its inverse square root. 97

Figure 60: A plot of the vertex points (listed in Table 5) obtained from the paraboloid fits at each slice on the grid scan, plotted on the ξx-ξy plane with error bars. The straight line represents a linear fit of the data. 99

Figure 61: A depiction (left) of the optimization strategy of finding the optimum point via the intersection of the 3D line that best fits the vertices obtained from slice fits, and the plane of zero spin tune error. The graph (right) shows a simulation of two million turns (equivalent to about 2.8 s of beam time) at the optimized point which shows virtually no decoherence. The fitting curve (red) measures a spin coherence time of 100

Figure 62: A scan of betatron tunes at all quadrupole settings that fulfil the stability criteria. This is similar to the scan shown in Figure 38, but done by [67] with a higher resolution. The sparse white "curves" are gaps in the data due to beam instability at betatron resonance conditions. 101

Figure 63: A tune diagram generated for the prototype ring in frozen spin mode, showing the various resonance configurations across the betatron tune spectrum. The black lines represent betatron resonances up to second order and the coloured lines represent spin resonances up to third order. The highlighted lines are settings where both resonances coincide. 102

Figure 64: A temporal "map" describing the sequence of actions that form the investigation of the lattice 105

Figure 65: A plot of the local maxima (paraboloid vertices) detected in the slices of constant χSS at the working point $Qx = 1.855$, $Qy = 0.823$. The plot highlights the reduced uncertainty and the stricter collinearity of the vertices as compared to Figure 60, as a result of increasing the number of turns simulated per point. 107

Figure 66: A graph plotting the model in { 188 } (red) and the parabolic model in { 202 } (green). The single free parameter of the parabola was tuned to fit the curve up to the blue tick. The progression shows that the estimated spin coherence time from the parabola could be regarded as a reasonable lower limit, as it possesses no new inflection points. 109

Figure 67: The restriction of data points as a result of the sextupoles SXF and SXSS being placed in close proximity at the straight sections. Points along the grey line of constant $\alpha 1$, like the slices used in the first grid scan, have points within the high sextupole field zones (marked in red). When the fields were manually adjusted, point-sets such as the black line, began to be considered. 110

Figure 68: A scheme of the racetrack lattice for the prototype ring. The blue bands are the EM bends, the red ticks represent quadrupoles, and the yellow ticks represent sextupoles. 113

Figure 69: Simulation results of the racetrack lattice showing the variations of the transverse beta functions (left vertical axis) and the horizontal dispersion function (right vertical axis) over one superperiod of the lattice, as performed by [77]. A linearized scheme of the superperiod is expressed at the top of the graph for reference. The dotted vertical lines represent the positions of the three sextupole families. 114

Figure 70: A scheme of one superperiod of an improved four-fold symmetry lattice, with the blue bands representing the EM bends, the red ticks representing quadrupoles while the yellow ticks represent sextupoles. 115

11. List of Tables

Table 1: The current upper limits on the EDM searches in nucleons and leptons, mentioned along with confidence levels. The measurement of the proton and the electron are from indirect measurements whereas the neutron, the muon and mercury were measured directly. [22] 12

Table 2: A table listing the Basic beam parameters for the prototype ring. [8] 60

Table 3: The list of parameters mentioned in { 167 } which are relevant for the statistical error in the proton experiment. [8] 63

Table 4: Field settings and optical properties of the zero-chromaticity working point. 80

Table 5: Locations of the optimum points as estimated by the fitting function, along with (not very precise) estimates of the spin coherence time at these points. 97

Table 6: A tabulation of all working points which were optimized using the method developed in chapter 5. Shown here are the optimized 2° optics. The model-predicted spin coherence times, their estimated lower limits, and the maximum chromaticity tolerances for $\tau \geq 1000\, s$ (measured based on the lower limits). The thick border separates the points from the two series on Qx. The shaded row shows data on the first working point eventually optimized over the course of the grid tests (see section 5.6) 108

12. List of Equations

{ 1 } 4
{ 2 } 5
{ 3 } 6
{ 4 } 6
{ 5 } 6
{ 6 } 7
{ 7 } 7
{ 8 } 8
{ 9 } 8
{ 10 } 8
{ 11 } 9
{ 12 } 9
{ 13 } 11
{ 14 } 12
{ 15 } 12
{ 16 } 12
{ 17 } 16
{ 18 } 16
{ 19 } 16
{ 20 } 16
{ 21 } 17
{ 22 } 19
{ 23 } 19
{ 24 } 19
{ 25 } 19
{ 26 } 20

{ 27 } 20
{ 28 } 20
{ 29 } 21
{ 30 } 22
{ 31 } 23
{ 32 } 23
{ 33 } 23
{ 34 } 24
{ 35 } 24
{ 36 } 24
{ 37 } 24
{ 38 } 24
{ 39 } 25
{ 40 } 25
{ 41 } 25
{ 42 } 25
{ 43 } 25
{ 44 } 25
{ 45 } 26
{ 46 } 26
{ 47 } 26
{ 48 } 27
{ 49 } 27
{ 50 } 27
{ 51 } 27
{ 52 } 27
{ 53 } 27
{ 54 } 27
{ 55 } 28
{ 56 } 28
{ 57 } 28

{ 58 } 28
{ 59 } 28
{ 60 } 28
{ 61 } 29
{ 62 } 29
{ 63 } 29
{ 64 } 29
{ 65 } 29
{ 66 } 30
{ 67 } 30
{ 68 } 30
{ 69 } 30
{ 70 } 30
{ 71 } 30
{ 72 } 31
{ 73 } 31
{ 74 } 31
{ 75 } 31
{ 76 } 31
{ 77 } 31
{ 78 } 32
{ 79 } 32
{ 80 } 32
{ 81 } 32
{ 82 } 32
{ 83 } 33
{ 84 } 33
{ 85 } 33
{ 86 } 34
{ 87 } 34
{ 88 } 34

{ 89 } 34
{ 90 } 34
{ 91 } 34
{ 92 } 35
{ 93 } 35
{ 94 } 35
{ 95 } 35
{ 96 } 35
{ 97 } 36
{ 98 } 36
{ 99 } 36
{ 100 } 37
{ 101 } 37
{ 102 } 37
{ 103 } 37
{ 104 } 37
{ 105 } 37
{ 106 } 38
{ 107 } 39
{ 108 } 39
{ 109 } 39
{ 110 } 40
{ 111 } 41
{ 112 } 41
{ 113 } 41
{ 114 } 42
{ 115 } 43
{ 116 } 43
{ 117 } 43
{ 118 } 43
{ 119 } 44

{ 120 } 44
{ 121 } 44
{ 122 } 44
{ 123 } 45
{ 124 } 45
{ 125 } 45
{ 126 } 45
{ 127 } 45
{ 128 } 45
{ 129 } 45
{ 130 } 46
{ 131 } 46
{ 132 } 46
{ 133 } 46
{ 134 } 46
{ 135 } 46
{ 136 } 46
{ 137 } 47
{ 138 } 47
{ 139 } 47
{ 140 } 47
{ 141 } 47
{ 142 } 48
{ 143 } 48
{ 144 } 48
{ 145 } 49
{ 146 } 49
{ 147 } 49
{ 148 } 49
{ 149 } 49
{ 150 } 49

{ 151 } 50
{ 152 } 51
{ 153 } 51
{ 154 } 51
{ 155 } 52
{ 156 } 52
{ 157 } 53
{ 158 } 54
{ 159 } 54
{ 160 } 54
{ 161 } 54
{ 162 } 55
{ 163 } 55
{ 164 } 56
{ 165 } 56
{ 166 } 56
{ 167 } 57
{ 168 } 57
{ 169 } 57
{ 170 } 63
{ 171 } 63
{ 172 } 68
{ 173 } 68
{ 174 } 68
{ 175 } 69
{ 176 } 70
{ 177 } 74
{ 178 } 77
{ 179 } 77
{ 180 } 78
{ 181 } 78

{ 182 } 78
{ 183 } 78
{ 184 } 78
{ 185 } 79
{ 186 } 81
{ 187 } 81
{ 188 } 82
{ 189 } 82
{ 190 } 82
{ 191 } 85
{ 192 } 86
{ 193 } 87
{ 194 } 91
{ 195 } 91
{ 196 } 92
{ 197 } 94
{ 198 } 94
{ 199 } 94
{ 200 } 95
{ 201 } 98
{ 202 } 99
{ 203 } 99
{ 204 } 100
{ 205 } 103
{ 206 } 103
{ 207 } 103
{ 208 } 104
{ 209 } 109